TECHNISCHE UNIVERSITÄT WIEN

Diese Dissertation haben begutachtet:

_____   _____

Prof. Dr. Kai-Thomas Brinkmann   Prof. Dr. Klaus Reygers

DISSERTATION

Dielectron production in proton–lead collisions at $\sqrt{s_{\mathrm{NN}}} = 5.02$ TeV with ALICE at the LHC

Ausgeführt zum Zwecke der Erlangung des akademischen Grades eines Doktors der
Naturwissenschaften unter Leitung von

Prof. Dr. Eberhard Widmann
and Dr. Michael Weber
Stefan-Meyer Institut für subatomare Physik
der Österreichischen Akademie der Wissenschaften

eingereicht an der Technischen Universität Wien Fakultät für Physik

von

Aaron Capon
Matr.-Nr. 01276598

_____   _____

Ort, Datum   Unterschrift

Zusammenfassung

Die am Large Hadron Collider (LHC) durchgeführten ultrarelativistischen Schwerionenkollisionen können so hohe Temperaturen erreichen, dass ein neuer Materiezustand beobachtet werden kann - das Quark-Gluon Plasma (QGP). Dieser stark wechselwirkende Zustand herrschte im frühen Universums für einige (wenige) Mikrosekunden nach dem Urknall vor. In diesem Zusammenhang spielt das Verständnis der Eigenschaften des QGPs eine Schlüsselrolle in der Vertiefung unseres Wissens über dessen spätere Entwicklung. Um die Eigenschaften des QGP oder heißer Kernmaterie generell zu erforschen, sind jedoch Referenzmessungen in kleinen Kollisionssystemen erforderlich, um die Teilchenproduktion und deren Eigenschaften im Vakuum oder in Gegenwart kalter Kernmaterie zu bestimmen. Am LHC werden hierzu üblicherweise Proton-Proton- (pp) oder Proton-Blei- (p–Pb) Kollisionen herangezogen. In den letzten Jahren wurden jedoch bestimmte Merkmale in diesen Kollisionen beobachtet, die ursprünglich dem QGP zugeschrieben wurden und unser Verständnis von Schwerionenkollisionen zum Teil in Frage stellen. Vertiefende Studien sind daher erforderlich, um die Datenlage zu klären.

Dielektronen (e^+e^-), d.h. korrelierte Elektron-Positron-Paare, stellen in dieser Hinsicht ein ausgezeichnetes Werkzeug dar, da sie keine Farbladung besitzen und nicht mit dem QGP wechselwirken. Weil Dielektronen den Kollisionsbereich deshalb im Wesentlichen unverändert verlassen, stellt die Messung ihrer Produktionsrate eine Methode dar, um die Eigenschaften des gesamten Systems unmittelbar zu untersuchen. Darüber hinaus enthält das invariante Massenspektrum der Dielektronen viele verschiedene Quellen von e^+e^--Paaren, die zu unterschiedlichen Zeiten im Kollisionsprozess erzeugt werden. Eine Messung dieser diversen Quellen erlaubt daher die Messung des zeitlichen Verlaufs des Kollisionssystems.

Diese Arbeit präsentiert die erste Analyse von Dielektronen bei niedriger invarianter Masse in p–Pb Kollisionen bei einer Schwerpunktsenergie $\sqrt{s_{NN}} = 5.02$ TeV gemessen mit dem ALICE Detektor. Elektronen und Positronen werden in Pseudorapidität $|\eta| < 0.8$ und Transversalimpuls $0.2 \leq p_T \leq 10$ GeV/c selektiert und die Ergebnisse werden für die invariante Masse $0 < m_{ee} < 3.5$ GeV/c^2 und den Paartransversalimpuls $0 < p_{T,ee} <$

$8\,\text{GeV}/c$ gezeigt. Das gemessene e^+e^--Spektrum wird mit einem sogenannten Cocktail aller bekannten hadronischen e^+e^--Quellen verglichen. Dieser Cocktail wird aus gemessenen Wirkungsquerschnitten der Teilchen in anderen Zerfallskanälen konstruiert, wobei die Beiträge semileptonischer Zerfälle von Hadronen mit schweren Quarks (Charm und Beauty) anhand der Ereignisgeneratoren POWHEG und PYTHIA 6.4 berechnet werden. Die simulierte Produktionsrate dieser semileptonischen Zerfälle wird auf den im Dielektronenkanal gemessenen Wirkungsquerschnitt in pp Kollisionen bei gleicher Schwerpunktenergie sowie auf die Atommassenzahl (A) des Bleikerns (A = 208) skaliert. Die Daten stimmen mit dem hadronischen Cocktail innerhalb der Unsicherheiten dieses Modells überein. Die Daten werden ebenfalls mit zwei zusätzlichen Modellen verglichen. Ersteres enthält thermisch erzeugte Dielektronen, die das Vorhandensein eines heißen Mediums anzeigen. In zweiterem wird die Charm-Produktionsrate aufgrund der Gegenwart des Bleikerns unterdrückt (einer der Effekte von kalter Kernmaterie). Keines der beiden Modelle kann angesichts der aktuell zu großen Ungenauigkeiten ausgeschlossen werden. Da e^+e^--Messungen bei derselben Schwerpunktsenergie verfügbar sind, wird der nukleare Modifikationsfaktor (R_{pPb}) als Funktion von m_{ee} und $p_{\text{T,ee}}$ analysiert. Im gesamten untersuchten Bereich stimmen die Daten innerhalb der Modellunsicherheiten mit dem hadronischen Cocktail sowie mit den beiden zusätzlichen Modellen überein.

ii

Abstract

Ultrarelativistic heavy-ion collisions performed at the Large Hadron Collider (LHC) are thought to reach such high temperatures that a new state of matter known as a quark–gluon plasma (QGP) is created. This state of strongly interacting matter is predicted to have dominated the early Universe a few microseconds after the Big Bang and understanding its properties is crucial for understanding its subsequent evolution. However, in order to understand heavy-ion collisions reference measurements in so-called small systems, at the LHC typically proton-proton (pp) and proton-lead (p–Pb) collisions, are required. Measurements in pp collisions represent the so-called baseline or vacuum measurements where the particle production rates in a vacuum can be determined. Whereas measurements in p–Pb collisions act as an intermediary which are used to determine any modifications to the particle production rates that arise from cold nuclear matter (CNM) effects, in contrast to hot matter effects originating from the QGP. In recent years, signatures that were originally attributed to the QGP have been observed in small system collisions, further complicating the current picture of heavy-ion collisions. Deeper studies into these small systems are now required to clear up the situation.

An excellent probe for this task are pairs of particles produced in these collisions called dielectrons (e^+e^-) which constitute a correlated electron/positron pair. As electrons and positrons are leptons, they lack any colour charge and therefore do not interact with the QGP. As they are able to leave the collision area essentially unaffected, measuring their production rates can provide a direct method to measure the properties of the system itself. Furthermore, as the dielectron invariant mass spectrum contains many differing sources of e^+e^- pairs which are produced at differing times of the collision process, measuring the different sources provides us with an overview of the evolution of the system from the initial collision to the final stage where the produced particles freely fly away from the collision point.

This thesis presents the first analysis of low-mass dielectrons in p–Pb collisions at a centre-of-mass energy $\sqrt{s_{\mathrm{NN}}} = 5.02$ TeV measured with the ALICE detector. The analysis is performed over the ranges $0 < m_{\mathrm{ee}} < 3.5\,\mathrm{GeV}/c^2$ and $0 < p_{\mathrm{T,ee}} < 8\,\mathrm{GeV}/c$

with the fiducial selection criteria $|\eta| < 0.8$ and $0.2 \leq p_T \leq 10\,\text{GeV}/c$. The measured e^+e^- spectrum is compared to a hadronic cocktail of known e^+e^- sources. The cocktail is constructed from measured cross sections of the constituent decays in other channels with the contributions from open-heavy flavour semi-leptonic decays calculated with two event generators: POWHEG and PYTHIA 6.4. The simulated heavy-flavour templates are scaled to the cross sections measured in the dielectron channel in pp collisions at the same centre-of-mass energy and scaled by the atomic mass number (A) of the Pb ion (A = 208). The data are in good agreement with the hadronic cocktail within uncertainties. The data are also compared to two additional models which incorporate thermally produced dielectrons which would indicate the presence of a hot medium, or a potential suppression of the charm production rate due to the presence of the Pb ion (a potential CNM effect). Neither model can be ruled out given the current precision. As e^+e^- measurements were available at the same centre-of-mass energy, the nuclear modification factor (R_{pPb}) was also analysed as a function of m_{ee} and $p_{T,ee}$. Over the entire investigated range the data are in agreement with the hadronic cocktail within the uncertainties, as well as with the two additional models.

Acknowledgements

First, I would like to thank my supervisor Eberhard Widmann for all his support during my time at the Stefan Meyer Institute. His help and guidance from the day I joined SMI for my master's project has made my time there both productive and very enjoyable. I would also like to thank Michael Weber, who provided day-to-day support and eagerly helped me with any problems I came across. Your passion for physics was truly motivating during this time, and this thesis would not have been possible without your help.

A big thank you to all my colleagues at SMI with whom I spent many hours discussing work, or playing N64 (both of which were very necessary!). Also many thanks to my colleagues from the ALICE low-mass dielectron working group, whose input during our weekly remote meetings greatly helped and improved my analysis, as well as ensuring any conferences abroad, where we could meet in person, were events to really look forward to. I must also thank the FWF doctoral college "Particles and Interactions" for their fascinating retreats and summer schools, as well as their funding support, which enabled me to travel extensively to both conferences and workshops, which in turn contributed to the writing of this thesis.

Lastly, I would to thank my family. To my parents, your continued support of my scientific pursuits made all of this possible. I can't thank you enough. To Franz and Nandita, you welcomed me into your family and made the transition to life in Austria an easy and incredibly enjoyable one. And finally, my biggest thanks and appreciation to my partner Sonali. Without your constant encouragement throughout these many years, none of this would have come to fruition.

"'In the beginning there was nothing, which exploded."'

(Terry Pratchett)

vi

Contents

List of Figures

List of Tables

1 Introduction

The cosmological model known as the Big Bang describes the evolution of our Universe [1]. The model predicts that at around 13.8 billion years ago our Universe was contained in a single point which then began to rapidly expand. After a few microseconds, the temperature remained too high for the quarks and gluons, the elementary particles that make up all visible matter, to form hadrons as we see them confined in today, rather they existed in an unbound state known as the quark–gluon plasma (QGP). To accurately model the evolution of our Universe, this phase of matter must be understood. Additionally, while the recently experimentally confirmed Higg's field is often touted as being responsible for the mass of the Universe, it only generates around 2% of the mass of the visible Universe, with the rest being dynamically generated by the strong force [2]. However, due to a phenomenon known as confinement, which stipulates that quarks and gluons are confined to hadrons at everyday temperatures and pressures, studying the strong force at large distances is very challenging. Examples like these, along with many more from cosmology, astrophysics and nuclear physics, motivate the research field of high energy collider physics, in particular the use of heavy-ion collisions.

Currently, the highest energy particle collisions are performed at the large hadron collider (LHC) at CERN (Conseil européen pour la recherche nucléaire) near Geneva, Switzerland. Of the four large detectors in operation at the LHC, the ALICE (A Large Ion Collider Experiment) detector [3, 4] was specifically designed to measure heavy-ion collisions. The energies and densities reached in these collisions are high enough that confinement is no longer observed by the strong force and a QGP is created which can be studied in a laboratory setting. An incredibly promising probe of these collisions are *dielectrons* (e^+e^-) which consist of a correlated electron-positron pair created during the collision. Since electrons[1] do not interact strongly, they are able to leave any QGP created during the collisions with minor interactions. And, as e^+e^- pairs are produced throughout the entirety of the collision, measuring their production rates over the course

---

[1]The term electron is used interchangeably with positron throughout this thesis unless otherwise specified.

of the collision can help us map aspects (e.g., temperature) of the evolution of the system itself.

This thesis presents the first e^+e^- analysis of p–Pb collisions at $\sqrt{s_{\mathrm{NN}}} = 5.02$ TeV which were recorded in 2016 with the ALICE detector. Dielectron production is analysed as a function of invariant mass (m_{ee}) and pair-transverse momentum ($p_{\mathrm{T,ee}}$) at midrapidity ($|\eta| < 0.8$) with a minimum transverse momentum restriction of $p_{\mathrm{T}} > 0.2\,\mathrm{GeV}/c$ over the range $m_{\mathrm{ee}} < 3.5\,\mathrm{GeV}/c^2$ and $p_{\mathrm{T,ee}} < 8\,\mathrm{GeV}/c$.

The thesis is organised as follows. This chapter contains an overview of the Standard Model (SM), Quantum Chromodynamics (QCD) and the basics of heavy-ion collisions (HICs). Chapter 2 covers the different sources of dielectrons. In Chapter 3 the ALICE detector is outlined. The analysis of e^+e^- production is presented in Chapter 4, with Section 4.6 detailing the method to generate the so-called hadronic cocktail (a simulation of all expected hadronic sources). In Chapter 5 the results of this analysis are presented. Lastly, the summary and outlook is given in Chapter 6.

1.1 The Standard Model

The SM of particle physics is a quantum field theory with a local $\mathrm{SU}(3) \times \mathrm{SU}(2) \times \mathrm{U}(1)$ gauge symmetry which describes how three of the four known fundamental forces interact with the known elementary particles [5]. The elementary particles described by the SM can be sorted into two groups. The matter particles, of which a subset make up the visible universe, come in three generations of quarks and leptons, coloured purple and green in Fig. 1.1, respectively, and are collectively labelled fermions which have half-integer spin values and therefore obey the Pauli exclusion principle [6]. The forces described by the SM are mediated by the force-carriers labelled bosons, coloured red in Fig. 1.1, and have integer spin values and are therefore not constrained by the Pauli-exclusion principle. The bosons and corresponding forces are as follows: the photon (γ) is the mediator of the electromagnetic (EM) force which governs interactions between electrically charged particles, the gluon (g) mediates the strong force which is responsible for binding quarks into hadrons and hadrons into into atomic nuclei, and finally the Z and $W^\pm$ bosons are responsible for the weak force which facilitates β-decay as well as interactions involving neutrinos. The strong force has a range of $\sim 10^{15}$ m and at this range is ~ 137 times stronger than electromagnetism, and 10^6 times stronger than the weak interaction. The SM also includes the Higgs boson (H), which in contrast to the other gauge bosons is a scalar particle, and contributes to the SM by partially facilitating the generation of the

masses of the elementary particles [7–9].

Standard Model of Elementary Particles
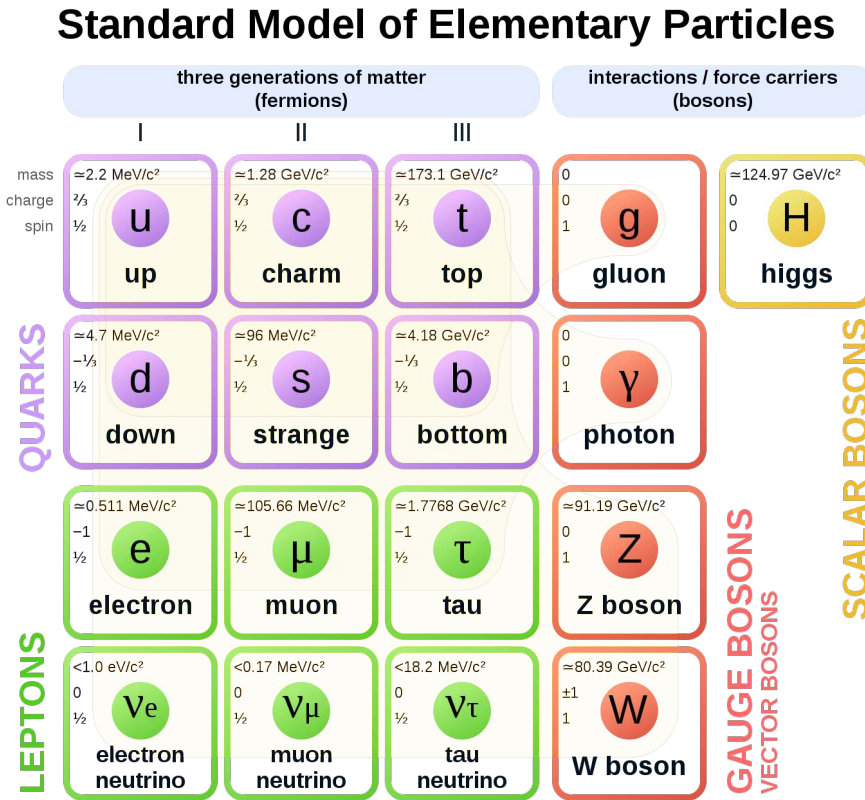
Figure 1.1: *Overview of the standard model of particles physics, consisting of 12 fermions and five bosons [10]. The loops indicate which bosons (red) interact with which quarks (purple) and/or leptons (green).*

1.2 Quantum Chromodynamics

The underlying dynamics of the strong interaction can be described by a quantum field theory known as Quantum Chromodynamics (QCD). QCD is a non-abelian gauge theory, due to gluon self-interactions, and is the SU(3) component of the SU(3) × SU(2) × U(1) symmetry group governing the SM. QCD describes the interactions between coloured quarks and gluons, where colour is the QCD analog to electric charge in Quantum Electrodynamics (QED), with the possible charges labelled green, red and blue. The gauge invariant QCD Lagrangian ($\mathcal{L}_{\mathrm{QCD}}$), expressed using Einstein notation, is written as [5]

$$\mathcal{L}_{\text{QCD}} = \sum_q \bar{\psi}_{q,a} \left(i\gamma^\mu \partial_\mu \delta_{ab} - g_s \gamma^\mu t_{ab}^C \mathcal{A}_\mu^C - m_q \delta_{ab} \right) \psi_{q,b} - \frac{1}{4} G_{\mu\nu}^A G^{A\mu\nu}. \qquad (1.1)$$

The $\psi_{q,a}$ represents the quark-field spinors for a given quark of flavour q and mass m_q, where the colour-index goes from a $= 1$ to $N_c = 3$, and the γ^μ represents the Dirac γ-matrices. The $\mathcal{A}_\mu^C$ corresponds to the gluon fields where C ranges from 1 to $N_c^2 - 1 = 8$. The eight generators of the SU(3) group are represented by t_{ab}^C, and the QCD coupling is represented by g_s. Lastly, the gauge invariant gluon field tensor represented by $G_a^{\mu\nu}$, which is the QCD analogue of the QED field strength tensor $F_{\mu\nu}$, is defined as

$$G_{\mu\nu}^a = \partial_\mu \mathcal{A}_\nu^a - \partial_\nu \mathcal{A}_\mu^a + g_s f_{ABC} \mathcal{A}_\mu^B \mathcal{A}_\nu^C, \qquad (1.2)$$

where f_{ABC} are the structure constants of SU(3). The last term in the equation indicates the self interacting nature of gluons and thus the non-abelian nature of QCD.

Unlike fermions and the electroweak gauge bosons, quarks and gluons are not observed as free particles. Rather, quarks are found in colour-singlet (colourless) bound states known as hadrons, typically as baryons (three quarks) or mesons (quark-antiquark). This experimentally observed phenomenon, known as *colour confinement* [11], can be thought of as if the gluon field between quarks form a thin flux tube which due to the non-abelian nature of QCD causes the strong force to remain constant per unit distance between the quarks regardless of their total separation (in contrast to QED). This means if two quarks are separated far enough from each other, it will at some point become energetically favourable to produce a new quark-antiquark pair than to further increase the distance between the original quarks.

Another defining feature of QCD is the so-called *asymptotic freedom* [12] which is another property that contrasts QED and QCD. In QED at low energies the electromagnetic coupling (α_{EM}) is finite ($\alpha_{\text{EM}} \approx 1/137$), however as the energy increases α_{EM} becomes strongly coupled and eventually runs off to infinity at the Landau pole. In QCD, however, asymptotic freedom results in the interactions between particles becoming weaker the higher the energy scale, or the closer the distance between the particles. As a result, the QCD coupling ($\alpha_{\text{s}}(Q^2)$) can be written as

$$\alpha_{\text{s}}(Q^2) = \frac{g_s^2(Q^2)}{4\pi} \approx \frac{1}{\beta_0 \ln(\frac{Q^2}{\Lambda_{\text{QCD}}^2})}, \qquad (1.3)$$

where Q is the momentum transfer of the interaction, β_0 a constant, and Λ_{QCD} the QCD scale parameter [5]. This effect can be thought of as an anti-screening of the colour

charge by the surrounding gluons, which at higher energies or closer distances means the colour charge will decrease. In Fig. 1.2, a collection of measurements of the $\alpha_s(Q^2)$ are plotted as a function of Q along with the corresponding order of the perturbation calculation used. As $Q \to 0$ the $\alpha_s(Q^2)$ rapidly approaches 1 and enters a regime where perturbative expansions are no longer valid. In this non-pertubative regime, different methods are required. A popular and promising approach to this problem is known as lattice QCD (LQCD) [13, 14]. LQCD is a discrete gauge theory devised on a lattice of space points which represent the quark fields with spacing a away from each other and the connections between the points representing the gluon fields. Calculations are done at finite lattice spacing and then extrapolated to $a = 0$ where the QCD continuum is recovered.
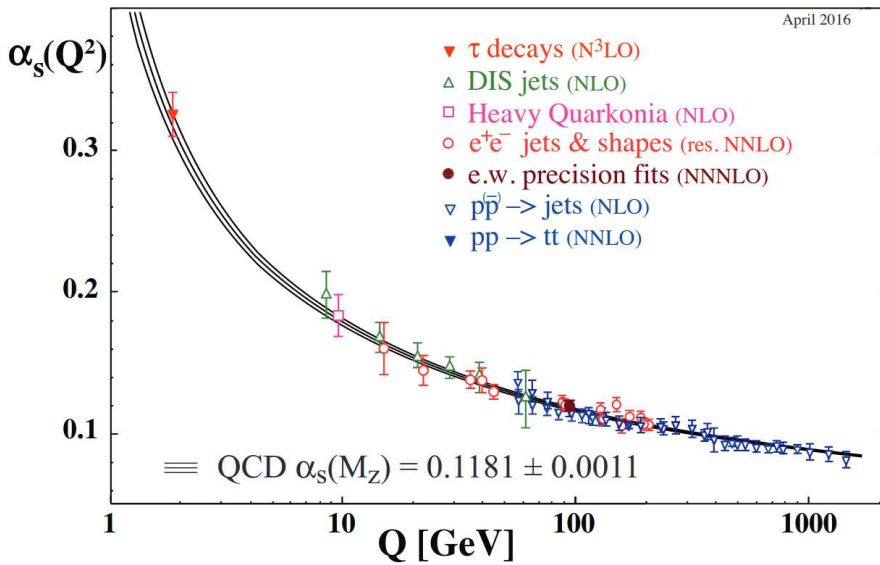
Figure 1.2: *Summary of $\alpha_s(Q^2)$ measurements as a function of the energy scale Q [5]. The order of QCD perturbation theory used to extract the $\alpha_s(Q^2)$ is indicated in brackets.*

QCD Phase Diagram

As a result of asymptotic freedom, at high enough temperatures or densities a system of quarks and gluons is predicted to exist as a quark–gluon plasma (QGP) where the quarks and gluons are no longer confined by the strong force and become the relevant degrees of freedom for the system [15, 16]. When entering this phase the partons[2] are said to undergo *deconfinement*. Analogously to the phase diagram for H_2O, a phase

---

[2]A parton is any of the constituent particles in a hadron, such as a quark or a gluon

diagram for strongly interacting matter can also be constructed. In Fig. 1.3, a qualitative representation of the QCD phase diagram is presented as a function of net baryon density[3] (μ_B) and temperature (T).
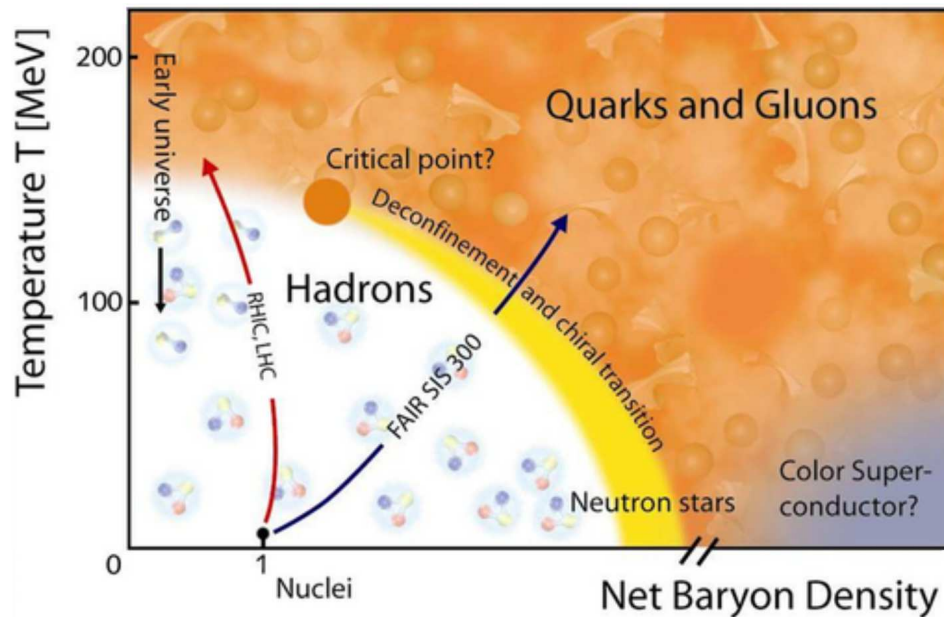
Figure 1.3: *Schematic of the QCD phase diagram represented as a function of temperature and net baryon density normalised to nuclear matter density [17].*

The lower left quadrant shown in white represents the region where confinement still applies and hadronic (bound) matter exists. Along the x-axis the label "Nuclei" corresponds to $T \approx 0$ K and $\mu_B \approx 940$ MeV which represents normal nuclear densities.

Outside of the hadronic region, deconfinement of the quarks and gluons can occur by increasing the temperature and/or the net baryon density. At low temperatures and high baryon density, the matter will begin to form a degenerate neutron gas, as is predicted in neutron stars. As the net baryon density further increases it begins to overcome the repulsive force between the degenerate neutrons, with the distance between the neutrons becoming so small that a degenerate gas of free quarks is formed. At even higher densities a colour superconducting phase is predicted [18]. Conversely, at $\mu_B \approx 0$ and high temperatures, as predicted in the early moments of the universe, the quarks and gluons become so energetic that they no longer interact (as predicted by *asymptotic freedom*). As this occurs, the quarks and gluons become the relevant

---

[3]Net baryon density (μ_B) quantifies the number of protons and neutrons minus the number antiprotons and antineutrons. Commonly in thermodynamics the μ_B will be represented by the baryochemical potential, which increases with μ_B.

degrees of freedom for the system and a QGP is created. According to LQCD, the pseudocritical temperature for deconfinement (T_c) given $\mu_B \approx 0$ is predicted to be T_c ≈ 151 MeV with the crossover between the phases a smooth transition [19]. As the net baryon density increases, the transition between the phases is expected to become a first-order transition, which implies the existence of a critical point. Both the order of the phase transition, as well as the existence of a critical point are still experimentally unknown. As a result, one of the primary goals of high energy nuclear physics is the investigation of the QCD phase diagram and its structure.

Chiral Symmetry

The fermion fields described in QCD can undergo two global transformations known as *vector* (Λ_V) and *axial vector* (Λ_A) transformations which are defined as

$$\Lambda_V : \psi \to e^{-i\frac{\vec{\tau}}{2}\vec{\Theta}}\psi \ \text{ and } \ \Lambda_A : \psi \to e^{-i\gamma_5\frac{\vec{\tau}}{2}\vec{\Theta}}\psi, \tag{1.4}$$

where ψ is now expressed in isospin notation ($\psi = (u, d)$), $\vec{\tau}$ is a vector of Pauli isospin-matrices, Θ corresponds to the angle of rotation, and γ_5 is the fifth Dirac matrix [20]. As the γ_5 matrix rotates the chirality[4] of the particle, the axial-vector transformation is often known as a chiral transformation. Under the condition that the quark masses are zero, the Lagrangian would be invariant under either transformation, and both the vector current and axial vector current would be conserved quantities with the system being said to be chirally symmetric. However, as the quarks have non-zero masses, the axial-vector term is no longer invariant and the chiral symmetry of the system is explicitly broken. In the light fermion sector (u, d and s quarks) this symmetry is said to be approximately conserved due to the quarks very light masses relative to the QCD energy scale ($\Lambda_{QCD} \approx 300$ MeV), whereas for the heavy quarks (c, b and t) their masses are too large to be able to assume the dynamics can be treated as small perturbations from the symmetric case [21].

The vector mesons have associated chiral partners which are defined by the axial-vector transformation. For example, the ρ^0 and a_1 vector mesons

$$\vec{\rho_\mu} = \bar{\psi}\vec{\tau}\gamma_\mu\psi, \ \vec{a_{1\mu}} = \bar{\psi}\vec{\tau}\gamma_\mu\gamma_5\psi, \tag{1.5}$$

---

[4]Chirality defines objects which are the mirror image of each other and cannot be superimposed onto one another. Closely related is helicity which is defined as the projection of the spin onto the momentum vector. In the case of massless particles, the helicity and chirality are the same.

are chiral partners which can be rotated into each other via the axial-vector transformation

$$\Lambda_A \vec{\rho_\mu} = \vec{\rho_\mu} + \vec{\Theta} \times \vec{a_{1\mu}}. \tag{1.6}$$

Naively, one expects such a connection to imply that the chiral partners have the same eigenvalues, that is the same mass. However, when the masses of chiral partners are measured, for example $m_{\rho^0} = 770 \text{ MeV}/c^2$ and $m_{a_1} = 1260 \text{ MeV}/c^2$ [5], the difference in masses is far larger than expected from the small non-zero quark masses and cannot be explained with explicit chiral symmetry breaking alone [21]. The observed difference can be explained via a so-called spontaneous breaking of the chiral symmetry. Spontaneous symmetry breaking occurs when the ground or vacuum state is not invariant under a symmetry group of transformations, but the Lagrangian is. The chiral condensate $(|\langle\overline{\psi}\psi\rangle|)$ acts like an order parameter for the spontaneous breaking of chiral symmetry and has a non-zero vacuum expectation value. At high enough temperatures and/or net baryon densities the $|\langle\overline{\psi}\psi\rangle|$ is expected to melt away $(|\langle\overline{\psi}\psi\rangle| \rightarrow 0)$ and the system's chiral symmetry is no longer spontaneously broken. This can be imagined analogously to the magnetisation of a ferromagnet where below the Curie temperature the material is spontaneously magnetised in a random direction due to an ordering of the magnetic moments, however once the Curie temperature is reached the material undergoes a phase transition where the atoms are no longer ordered and the magnetisation disappears. The $|\langle\overline{\psi}\psi\rangle|$, calculated within the SU(3) Nambu and Jona-Lasinio model [22], is shown in Fig. 1.4 as a function of temperature and nuclear density along with the different regions that are probed by some common experiments [23]. In the chirally restored phase, chiral partners like the ρ^0 and a_1 mesons would become degenerate [24]. This is explicitly shown in Fig. 1.5 where the vector and axial-vector spectral functions, with contributions from the ground states (ρ^0 and a_1 peaks), the first excited states (ρ' and a_1') and a chirally invariant (i.e., identical) continuum, are presented at a range of temperatures [25]. In the vacuum the peaks of the spectral functions (i.e., the masses of the ground state chiral partners) are not aligned due to the broken chiral symmetry. As the temperature is increased, the vector spectral function peak begins to broaden at the same time as the peak slightly drops. The axial-vector spectral function peak drops significantly as the temperature increases until the chiral restoration temperature $T_{\text{chiral}} \approx 159 \text{ MeV}$ [26] is reached, at which point both peaks are aligned indicating a degeneracy in the chiral partner's masses due to the restoration of chiral symmetry.
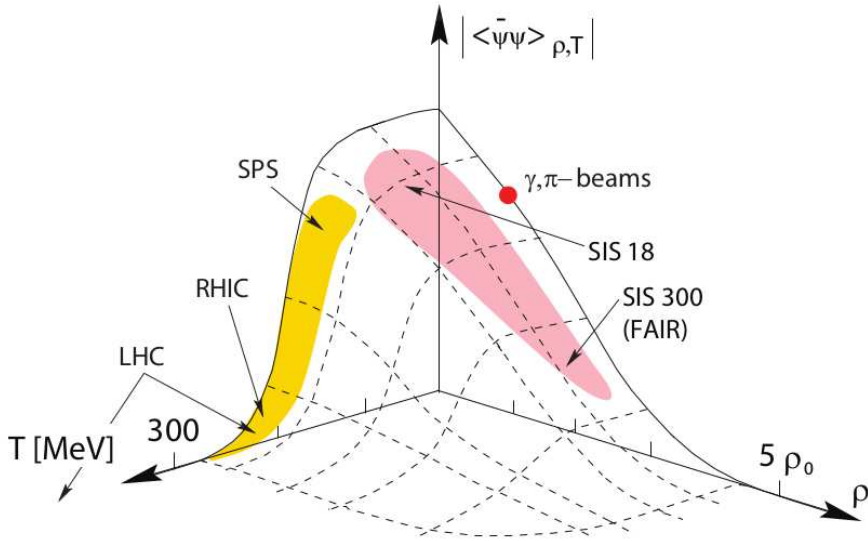
Figure 1.4: *The expected value of the quark condensate ($|\langle\overline{\psi}\psi\rangle|$) plotted as a function of temperature and nuclear density [23] calculated using the Nambu and Jona-Lasinio model [22], along with the different regions that are probed by a selection of experiments.*
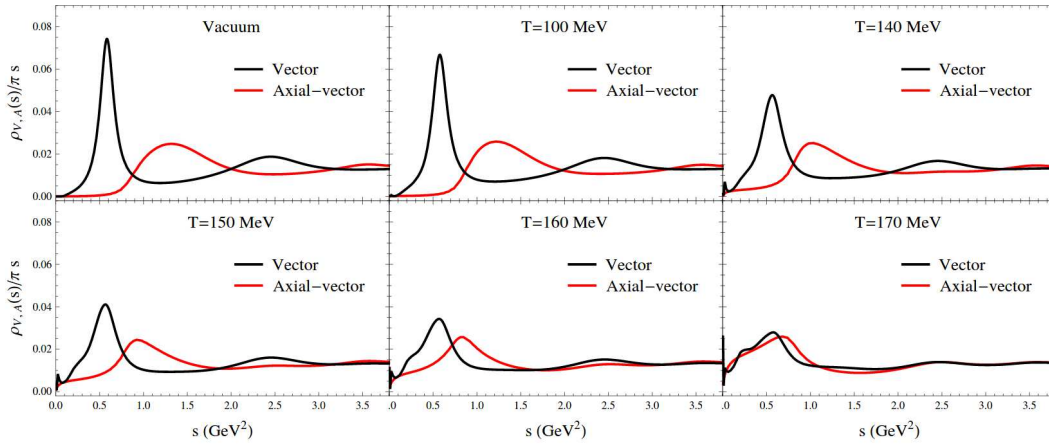
Figure 1.5: *Finite-temperature vector (black) and axial-vector (red) spectral functions presented for a range of increasing temperatures [25]. The spectral functions contain contributions from the ground states (ρ^0 and a_1 peaks), the first excited states (ρ' and a_1') and a chirally invariant (i.e., identical) continuum. The x-axis ($s(\mathrm{GeV}^2)$) represents the mass.*

1.3 Heavy-Ion Collisions

Heavy-ion collisions at ultra-relativistic energies[5] allow us to study the effect of extreme temperatures and densities on nuclear matter in a laboratory setting. The current understanding of the stages of a HIC is represented in Fig. 1.6 where the left and right sides of the plot depict a HIC with and without the creation of a QGP. The evolution of a HIC which reaches T_c will now be outlined.
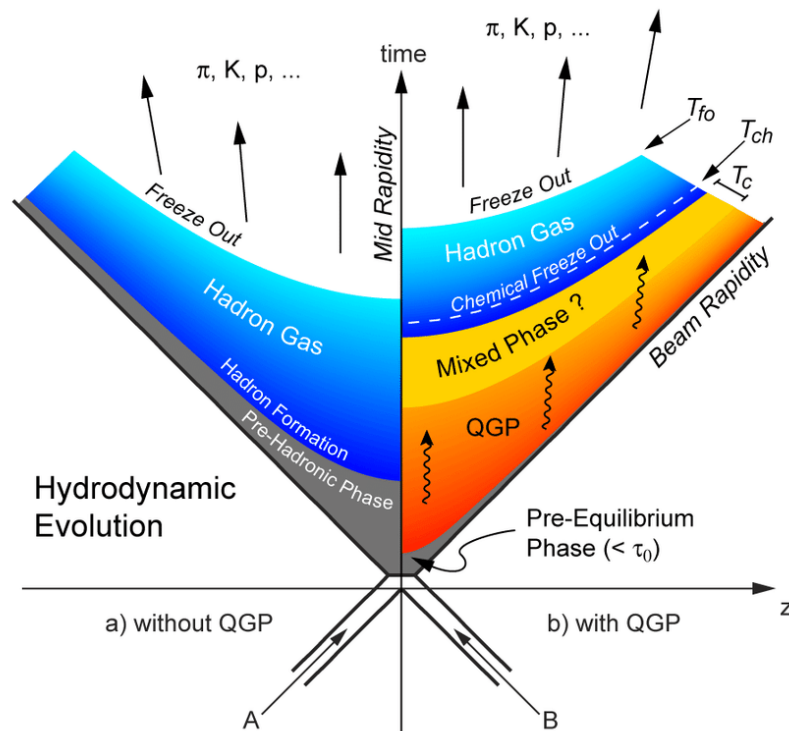
Figure 1.6: *Space-time diagram depicting a relativistic heavy-ion collision with (right) and without (left) the creation of a QGP.*

To begin, the ions (typically Pb–Pb at the LHC) are accelerated to velocities nearing the speed of light and, due to the Lorentz contraction, are compressed along the direction of travel appearing as pancake-like objects. During the initial collision the partons undergo hard scattering processes while the ions cross paths. Immediately after the collision a *pre-equilibrium* phase is predicted where the produced particles interact with each other and the system begins to thermalise until a local equilibrium is potentially reached, and if T_c was reached a QGP is formed. The hot and dense system then rapidly

---

[5]The energy of a particle is calculated with $E^2 = m^2c^2 + p^2c^2$. A particle is said to be ultrarelativistic when $pc \gg mc^2$ at which point the energy can be reasonably approximated with $E = pc$.

expands into the vacuum due to the significant pressure gradient, which at this point can be described with relativistic hydrodynamics, and as a result begins to cool down. Once the system has cooled down to T_c, *hadronisation* occurs where the quarks and gluons become confined into hadrons and mesons. The system continues to expand until the *chemical freeze-out* temperature (T_{ch}) is reached where inelastic collisions between the hadrons stop, and the relative abundances of the particle species no longer change outside of the expected hadronic decays. Following this, the gas of interacting hadrons continues to expand until the *kinematic freeze-out* temperature (T_{fo}) is reached where the mean free path length between the hadrons is larger than the size of the system. At this point the hadrons are free to leave the system without further alterations to their kinematics.
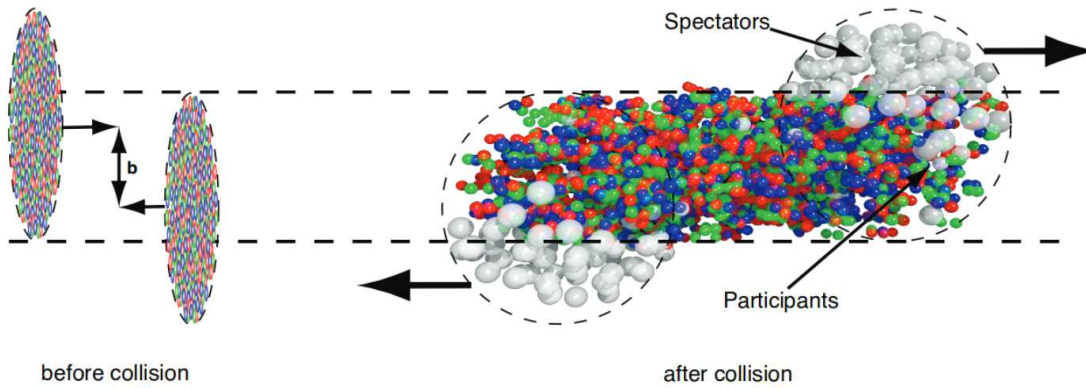
Figure 1.7: *Representation of two colliding nuclei in a relativistic heavy-ion collision [27]. The incoming nuclei are offset by the impact parameter (b) which defines the level of overlap. The partons in the overlap zone take part in the collision are labelled participants (N_{part}) and those that are outside this region are labelled spectators.*

A central property of a HIC is the geometry of the system and how to characterise it. A pictorial representation of a HIC is shown in Fig. 1.7. The impact parameter (b) defines the overlap region between the two incoming nuclei. As the overlap between the two increases, the number of participating nucleons (N_{part}) and the number of inelastic nucleon-nucleon collisions, often called binary collisions (N_{coll}), increases. However, as these quantities are not directly observable, it is necessary to characterise the resulting events via their centrality (measured in percentiles) which can be inferred from the collisions charged particle multiplicity (N_{ch}) under the assumption that the multiplicity increases monotonically with b. Techniques that try to model this are referred to as

"Glauber Models" with MC Glauber modelling [28] now the most common approach. To relate the Glauber model to experimental data, measured distributions, for example the number of events as a function of charged-particle multiplicity (dN_{evt}/dN_{ch}), are mapped to the corresponding calculated distributions which start from Glauber calculations to determine N_{part} and N_{coll} and then the particle production from each collision is determined by sampling from a negative binomial distribution which is determined via a fit to data [29, 30]. Average values within each centrality class for the data and simulated distributions are then compared and the Glauber model can be related to a physical observable. This is shown in Fig. 1.8 where the measured cross section as a function of N_{ch} ($d\sigma/dN_{ch}$) is decomposed into centrality classes which are then mapped to the initial overlap of the colliding nuclei. For example, collisions with a large b (small overlap) are labelled peripheral events, whereas collisions with a low b (large overlap), and thus high multiplicity, are labelled central events.
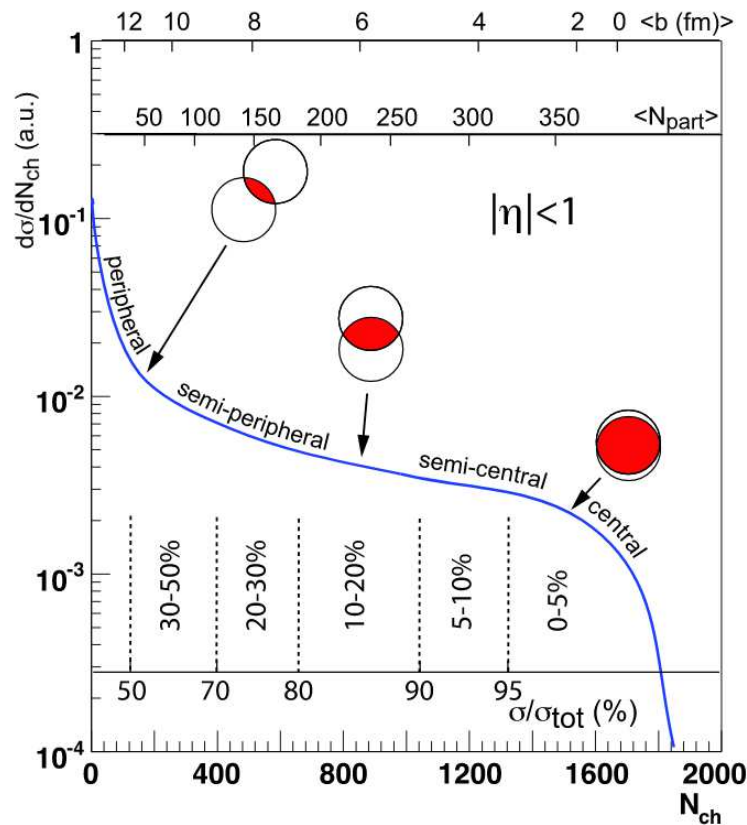
Figure 1.8: *Pictorial representing the correlation of the final state observable (N_{ch}) with the Glauber calculated quantities: impact parameter (b) and the number of participating nucleons (N_{part}) [28].*

As the presence of a QGP in HICs alters the overall evolution of the system, many of the observables are expected to be modified with respect to their measurements performed in a vacuum (e.g., pp collisions). This provides us with a potential mechanism for determining the presence and properties of the QGP. Many experimental measurements of potential QGP signatures in HICs have been reported [31] and have led to a general consensus that a QGP is created in HICs. A brief overview of some of the key QGP signatures are now presented.

- **Strangeness enhancement:** One of the earliest predictions of a QGP signature was the enhanced production of strange quarks. Strange quarks are not present in the colliding nuclei, so they must be created during the collision process. As the mass of a strange quark pair is just above T_c, a sharp increase in strangeness production as function of collision energy was predicted to indicate the presence of a QGP as it could thermally produce additional strange quark pairs. This has been observed at many different experiments which have studied enhanced strange baryon production [32–34].

- **In-medium Parton Energy Loss:** A key signature for the creation of a hot and dense medium is the observation of parton energy loss. This occurs as the parton traverses the medium and interacts with it. The process depends on the type of parton as well as the volume and density of the medium, and can therefore be used to infer the properties of the system, for example, the size, temperature colour density, etc, of the QGP. The most common way to investigate this effect is to compare the nuclear modification factor (see Eq. 1.9) between differing systems. A particularly interesting aspect of parton energy loss is the measurement of highly energetic back-to-back collimated beams of particles (so-called *jets*) which are the product of initial hard parton scattering. The total energy of the measured jets can vary due to their differing path lengths through the medium which enables the properties of the medium to be inferred. Parton energy loss is now well-established and has been observed by many different high energy experiments [35–38].

- **Collective flow:** The observation of so-called collective flow between particles and the resulting success describing this phenomenon with hydrodynamics is considered a key QGP signature. These flow effects can be quantitatively studied by measuring the azimuthal distributions between particles with respect to the

collision symmetry planes (Ψ_n) and can be written as

$$\frac{\mathrm{d}N}{\mathrm{d}\varphi} = \frac{1}{2\pi}(1 + 2\sum^{n} \nu_n \cos(n(\varphi - \Psi_n))), \tag{1.7}$$

where φ is the azimuthal angle and ν_n represent the harmonics of the distribution (n) with each harmonic associated with a specific type of collective motion [39, 40]. For example, the first flow coefficient ν_0 is associated with the purely radial component of the expansion. This increases the p_T of the particles produced in collisions, but due to the different particle masses the effect is not uniform and a mass dependent hardening of the low p_T portion of the spectrum in heavy-ion collisions is observed. The second flow coefficient, known as elliptic flow (ν_2), mainly quantifies the elliptical deformation of the initial fireball which stems from the overlap region between the colliding nuclei. By measuring this coefficient, the viscosity of the medium can be inferred.

- **Quarkonium production:** Due to the heavy quarks' large masses, the production of quarkonia, a flavourless meson containing a heavy quark and its own antiquark, is the result of hard scattering processes during the initial stages of the collision. In the presence of a QGP a suppression of the quarkonium production rate was predicted to occur. This suppression is due to the free colour charges in the medium which effectively screen the potential between heavy quarks, allowing them in essence to melt in the medium. This effect was initially observed by many different experiments [41–43]. However, at higher energies a competing effect was observed where the suppression factor was decreasing as the collision energy increased and was coined *regeneration*. Somewhat analogously to strangeness enhancement, although no heavy quarks are thermally generated, as the collision energy increases, the chance that a heavy quark is produced in the initial scattering processes also increases thereby increasing the probability that two separately produced heavy quarks can later hadronise and form a bound state [44, 45]. This can be schematically seen in Fig. 1.9 where heavy-flavour meson production is shown for low energies (top row) and high energies (bottom row).

To ensure the observations in HICs were in fact due to the presence of a QGP, studies in smaller systems (typically pp and pA) were to be used as control groups, so that any non-QGP effects could be disentangled from the measurements performed with heavy-ions. To this end, pp collisions were used as the baseline measurement to characterise
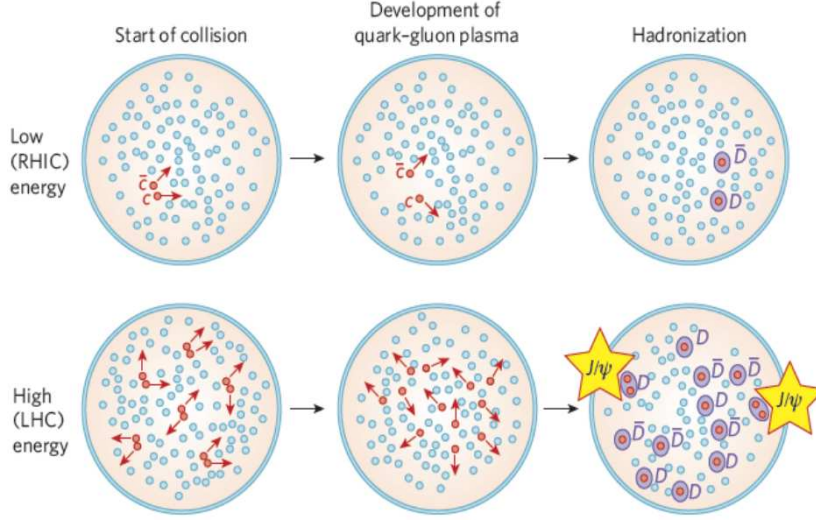
Figure 1.9: *Schematic overview of the open heavy-flavour and quarkonium production compared between low (top) and high (bottom) energies. At higher energies (LHC) the larger abundance of heavy quarks increases the chance of two separately created heavy quarks recombining in the QGP phase or at the phase boundary, resulting in the regeneration effect seen at high energies.*

medium-free (vacuum) collisions, while pA collisions were used to disentangle the cold nuclear matter (CNM) effects from the final state collective effects due to the QGP.

A straight-forward approach to measure the differences between the collision systems is to calculate the so-called nuclear modification factor which is the ratio of the same quantity measured in two different systems. For example, comparing measurements in pp and p–Pb collisions the corresponding nuclear modification factor (R_{pPb}) can be expressed as

$$R_{\mathrm{pPb}}(m_{\mathrm{ee}},\ p_{\mathrm{T,ee}}) = \frac{1}{\langle N_{\mathrm{coll}} \rangle} \frac{\mathrm{d}^2 N^{\mathrm{pPb}}/\mathrm{d}m_{\mathrm{ee}}\mathrm{d}p_{\mathrm{T,ee}}}{\mathrm{d}^2 N^{\mathrm{pp}}/\mathrm{d}m_{\mathrm{ee}}\mathrm{d}p_{\mathrm{T,ee}}}, \tag{1.8}$$

where $\mathrm{d}^2 N^{\mathrm{pp}}/\mathrm{d}m_{\mathrm{ee}}\mathrm{d}p_{\mathrm{T,ee}}$ and $\mathrm{d}^2 N^{\mathrm{pPb}}/\mathrm{d}m_{\mathrm{ee}}\mathrm{d}p_{\mathrm{T,ee}}$ are the differential yields measured in pp and p–Pb collisions, respectively, and $\langle N_{\mathrm{coll}} \rangle$ is the average number of inelastic nucleon-nucleon collisions (introduced in Section 1.3). An equal representation can be written for cross section measurements with the same scaling assumption as

$$R_{\mathrm{pPb}}(m_{\mathrm{ee}},\ p_{\mathrm{T,ee}}) = \frac{1}{A} \frac{\mathrm{d}^2 \sigma^{\mathrm{pPb}}/\mathrm{d}m_{\mathrm{ee}}\mathrm{d}p_{\mathrm{T,ee}}}{\mathrm{d}^2 \sigma^{\mathrm{pp}}/\mathrm{d}m_{\mathrm{ee}}\mathrm{d}p_{\mathrm{T,ee}}}, \tag{1.9}$$

where $\mathrm{d}^2 \sigma^{\mathrm{pp}}/\mathrm{d}m_{\mathrm{ee}}\mathrm{d}p_{\mathrm{T,ee}}$ and $\mathrm{d}^2 \sigma^{\mathrm{pPb}}/\mathrm{d}m_{\mathrm{ee}}\mathrm{d}p_{\mathrm{T,ee}}$ are the measured differential cross sections in pp and p–Pb collisions, respectively, and A the atomic mass number of the

ion (A = 208 for a Pb ion). In both cases the scaling assumes that the measurements in p–Pb are simple superpositions of the same quantity measured in pp collisions scaled by the number of nucleon-nucleon collisions, often labelled N_{coll} scaling or A-scaling. This is a commonly used scaling assumption when investigating processes which depend on the initial hard scattering process, for example, heavy-flavour quark production which will be covered in Section 2.2, and would be correct if the resulting R_{pPb} is equal to unity. If, however, the R_{pPb} is smaller than one, the production rate is said to be suppressed with respect to pp collisions, and, conversely, if the R_{pPb} is above unity the production rate would be enhanced. The same logic can be used to construct the nuclear modification factor for Pb–Pb collisions (R_{PbPb}). For example, in Fig. 1.10 the nuclear modification factor for charged particle measurements by ALICE in p–Pb collisions at $\sqrt{s_{NN}} = 5.02$ TeV and Pb–Pb collisions at $\sqrt{s_{NN}} = 2.76$ TeV are compared [46]. Here the R_{pPb} is consistent with unity for $p_T > 2\,\mathrm{GeV}/c$, which in this case indicates that the strong suppression observed in both central and peripheral Pb–Pb collisions is not simply due to the presence of cold nuclear matter but rather the result of jet quenching, which describes the energy loss of high energy particles and jets in AA collisions with respect to reference measurements.
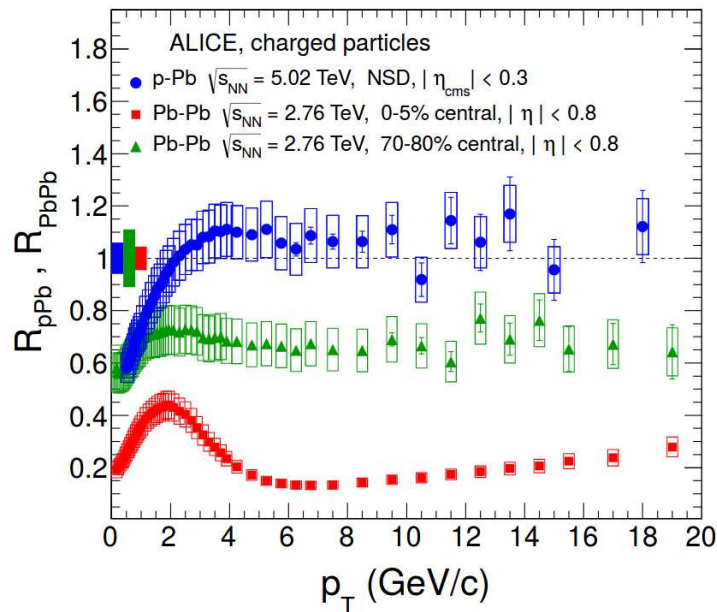
Figure 1.10: *The nuclear modification factor (R_{pPb} and R_{PbPb}) of charged particles as a function of p_T measured by ALICE in p–Pb collisions at $\sqrt{s_{NN}} = 5.02$ TeV as well as in central and peripheral Pb–Pb collisions at $\sqrt{s_{NN}} = 2.76$ TeV [46].*

However, a spate of measurements performed over the last decades in small systems have themselves exhibited collective behaviour that was previously attributed to the presence of a QGP and has prompted a revision of the idea that such a simple separation of the physics between the collision systems is possible [47,48]. One of the prime examples is the discovery of near-side and away-side long-range particle correlations in pp [49] and p–Pb [50–52] events which resemble those seen in Pb–Pb [53]. However, the picture is further muddied by the lack of jet quenching observed in the small system measurements (as discussed in Fig. 1.10), which is a key QGP signature. Another example of a QGP signature now in doubt is the previously discussed strangeness enhancement, which has now been observed in high multiplicity pp [54] and p–Pb [55] collisions. Contradictory results like these indicate that a much deeper understanding of the physics occurring in small systems is required.

One clear indication of hot and dense medium is the emission of thermally produced photons. Radiated photons can undergo pair production into a lepton pair ($\ell^-\ell^+$) and as leptons do not interact strongly, they can freely leave the hot medium and reach the detector. For this reason, dileptons are an excellent probe when investigatng high energy particle collisions. The following section will focus solely on electron-positron pairs, so-called dielectrons (e^+e^-), which are analysed in this thesis.

2 Dielectron Production

Dielectrons are produced throughout the whole course of a HIC [56], and, due to their lack of colour charge, are able to leave the collision area with minimal interactions, making them very interesting probes. This section outlines those different sources beginning with decays of light-flavour hadrons in Section 2.1, semi-leptonic open heavy-flavour decays in Section 2.2, J/ψ production in Section 2.3, Drell-Yan production in Section 2.4, and lastly thermal dielectron production in Section 2.5.
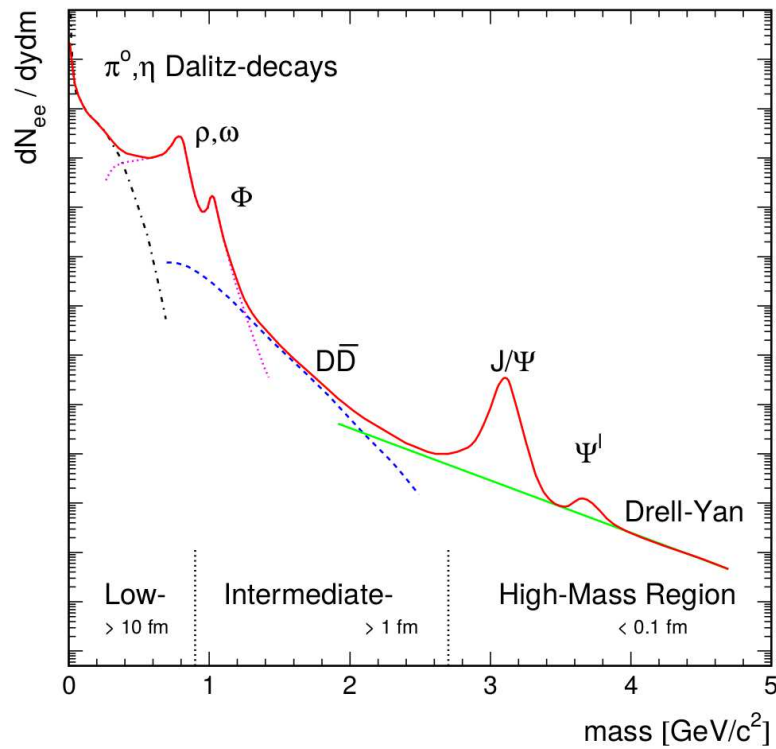
Figure 2.1: *Schematic drawing of the dielectron invariant mass spectrum [57]. The vertical dashed lines roughly define the main regions with which the spectrum can decomposed into.*

2.1 Light-flavour Hadron Decays

Below $m_{ee} \lesssim 1.1\,\mathrm{GeV}/c^2$, light-flavour meson Dalitz ($h \to X \mathrm{e}^+\mathrm{e}^-$) and resonance ($h \to \mathrm{e}^+\mathrm{e}^-$) decays are the main contributors to the vacuum dielectron spectrum. These mesons consist of three pseudoscalar mesons ($\mathrm{J}^P = 0^-$) π^0, η and η', as well as three vector mesons ($\mathrm{J}^P = 1^-$) ρ^0, ω and ϕ. While both resonant and Dalitz decays for all the previously listed mesons are allowed, the branching ratios for many of the decay channels are incredibly small, in particular the resonant $\mathrm{e}^+\mathrm{e}^-$ decays for the pseudoscalar mesons. For example, the branching ratio for the Dalitz decay $\pi^0 \to \gamma \mathrm{e}^+\mathrm{e}^-$ is 0.0117, whereas the resonant decay $\pi^0 \to \mathrm{e}^+\mathrm{e}^-$ is 6.46×10^{-8}. As the pseudoscalar mesons appear to only contribute to dielectron production via Dalitz decays, the spectrum in the very low-mass region ($m_{ee} \lesssim 0.4\,\mathrm{GeV}/c^2$) is a smooth continuum of sources dominated by these decays. The vector mesons, however, all contribute with resonance decays, providing resonance structures for $0.5 < m_{ee} < 1.1\,\mathrm{GeV}/c^2$, with the ω and ϕ also contributing to the continuum via Dalitz decays.

Dielectron production from the vector mesons in the hadron gas stage is due to the enhancement of the $\pi\pi$ cross section. Since the quantum numbers of these vector mesons and the photon are the same, their coupling to dileptons can be described by the Vector Dominance Model where the photon is said to be a superposition of the exclusively electromagnetic photon and a vector meson [58]. A Feynman diagram in Fig. 2.2 illustrates the process using the ρ^0 meson as the mediator coupling to the photon: $\pi^+\pi^- \to \rho^0 \to \gamma^* \to \ell^+\ell^-$.
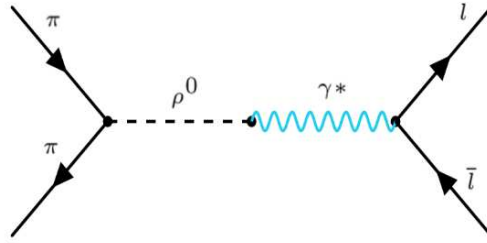
Figure 2.2: *Feynman diagram of vector dominance model for dilepton production [59].*

In this stage of the collision, the peak structure of the vector mesons are of particular interest, as near the phase boundary from the partonic to hadronic stage the spectral shapes are predicted to be modified by the hot medium [60–63]. An example of the broadening of the ρ^0 meson spectral function was presented in Fig. 1.5. The broadening

is attributed due to many-body interactions in the presence of hot hadronic matter as well as a partial restoration of chiral symmetry, and would be accompanied by the masses of the chiral partners ρ^0 and a_1 becoming degenerate. While these in-medium modifications are possible for all three vector mesons, the ρ^0 meson's short lifetime ($\tau_{\rho^0} \approx 1.3$ fm/c) means it is of particular interest as it is ensured to decay in the medium.

2.2 Open Heavy-flavour Decays

Another important contribution to the dielectron spectrum are semi-leptonic open heavy-flavour decays. Open heavy-favour hadrons contain one c or b quark (or antiquark) with the other antiquark (or quark) coming from the light sector ($\bar{u}$, $\bar{d}$ or $\bar{s}$). For example, the lightest D and B mesons are $D^+ = c\bar{d}$ and $B^+ = u\bar{b}$. At LHC energies, the contributions from open heavy-flavour meson decays to dielectron production are very significant over nearly the entire investigated mass range, and become essentially the sole source of measured e$^+$e$^-$ pairs in the intermediate mass range ($1.1 < m_{ee} < 2.7$ GeV/c^2). These correlated e$^+$e$^-$ pairs are the result of initial inelastic hard-scattering processes between the incoming nucleons which produce a pair of heavy quarks ($Q\bar{Q} = $ c$\bar{c}$ or b$\bar{b}$). At leading order the heavy quark pairs can be produced via quark-quark interactions ($q\bar{q} \to g^* \to Q\bar{Q}$) and, since QCD is non-abelian, also via gluon-gluon fusion ($gg \to g^* \to Q\bar{Q}$), as shown in Fig. 2.3.
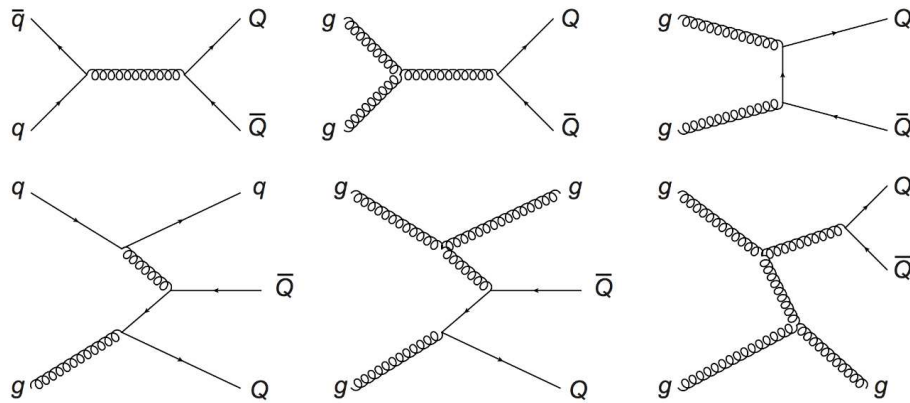
Figure 2.3: *Feynman diagrams of heavy quark production at leading order [57].*

The resulting $Q\bar{Q}$ pair undergoes fragmentation forming a meson-antimeson pair by binding to a light quark. These mesons can decay semi-leptonically which results in a correlated e$^+$e$^-$ pair. An example of such a semi-leptonic decay from a c$\bar{c}$ pair is shown

in Fig. 2.4. The total branching ratio for D^0 decaying into an electron is approximately 10% [5].
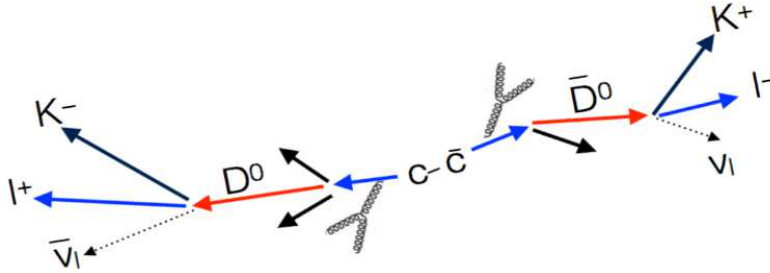
Figure 2.4: *Diagram illustrating the semi-leptonic decay channel by which open heavy- flavour mesons contribute to the dielectron spectrum by producing correlated dielectron pairs.*

Since these heavy-flavour quark pairs are created in the initial collision, they are particularly interesting for probing the presence of matter as they experience the entire evolution of the system [64]. In particular, heavy-flavour decays measured in small systems can provide crucial information about any initial or final state interactions due to the presence of cold nuclear matter. As interactions with the nucleus can effect heavy-flavour production rates, consequently the measured dielectron production rate will also be modified.

To measure and quantify this phenomenon parton distribution functions (PDFs) are introduced. The PDF is a probability density function for finding a parton within a free proton with a given momentum fraction (x) at a given resolution or energy scale (Q). PDFs are defined within the framework of collinear factorisation [65]. This states that when $Q^2 >> \Lambda_{\text{QCD}}$, the cross section and the PDF can be factorised with the non-perturbative physics contained in the PDF. Thanks to the universal nature of the PDFs (they are process independent and follow the DGLAP equations [66]), they can be constrained by looking at a wide range of experimental results, with the primary two being Deep Inelastic Scattering (DIS) and Drell-Yan (DY) processes (outlined in Section 2.4), however more recent iterations now include neutrino experiments as well as W, Z and dijet measurements from LHC experiments [67]. The nuclear parton distribution function (nPDF) is analogous to the PDF but for bound nuclear states (e.g., Pb). For two hadrons A and B that produce a final state k (and additional products), the cross section ($\sigma^{AB \to k+X}$) can be factorised in terms of a sum over all involved partons i, j as

$$d\sigma^{AB \to k+X} = \sum_{i,j,X'} f_i^A(x, Q^2) \otimes d\hat{\sigma}^{ij \to k+X'}(Q^2) \otimes f_j^B(x, Q^2) + \mathcal{O}(1/Q^2), \qquad (2.1)$$

up to power corrections ($\mathcal{O}(1/Q^2)$). Due to asymptotic freedom (discussed in Section 1.2), the cross section $d\hat{\sigma}^{i,j \to k+X'}$ is perturbatively calculable, and the nPDF terms (f_i^A and f_j^B) now encode the long-range non-perturbative physics. From this another nuclear modification factor can be defined for each parton i as

$$R_i^A(x, Q^2) = \frac{f_i^A(x, Q^2)}{f_i^P(x, Q^2)}, \qquad (2.2)$$

where f_i^A is the nPDF and f_i^P the PDF. A schematic drawing of a global fit for R_i^A is shown in Fig. 2.5 with the fit parameters (x_a, x_e, y_a, y_e) plotted along the axes which enclose the commonly defined x-regions: shadowing, antishadowing, the EMC effect[1] and Fermi motion. By using R_i^A one can apply expected nuclear modifications to simulated collisions for comparison with data, or, conversely, by measuring the nuclear modification factors introduced in Eq. 1.9, for example heavy-flavour production rates, one can use these results to further constrain the underlying nPDFs themselves.
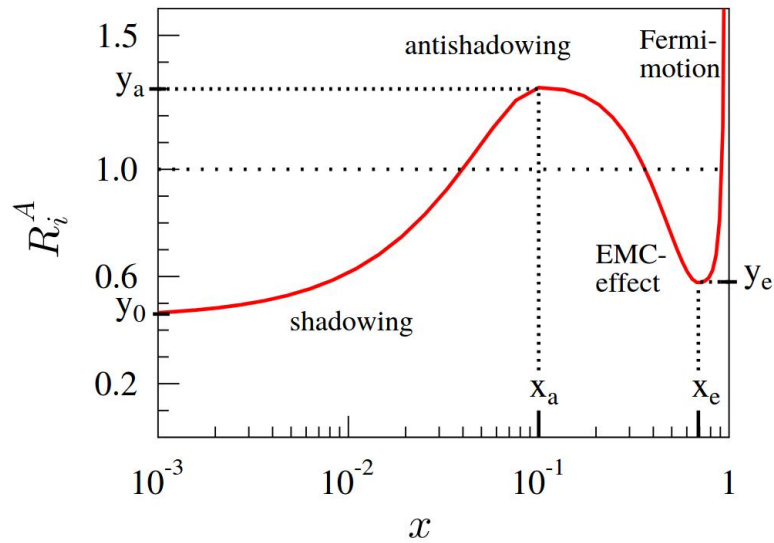
Figure 2.5: *An example of the fit function for $R_i^A(x)$ along with the fit parameters which define the regions labelled on the plot [69].*

---

[1]The EMC effect describes the high-x shadowing region which was first discovered by the European Muon Collaboration [68].

2.3 J/ψ

The J/ψ meson is the lowest energy bound state of charmonium which is a flavour-neutral meson consisting of a charm and anticharm quark ($c\bar{c}$). As with the open heavy-flavour mesons just outlined, charmonium bound states are produced when heavy quarks produced in the initial hard scattering processes hadronise. Charmonium states can decay directly into a e$^+$e$^-$ pair mediated by a photon (see Fig. 2.6) with a branching ratio for J/ψ →e$^+$e$^-$ of $5.96 \pm 0.06\%$ [5].
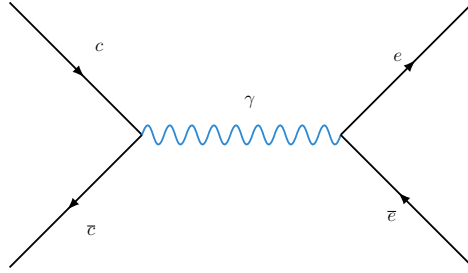
Figure 2.6: *Charmonium decaying into* e$^+$e$^-$ *pair via a photon.*

2.4 Drell-Yan Production

A Drell-Yan process involves a quark and antiquark annihilation which produces a lepton-antilepton pair and is facilitated by a γ^* or Z boson [70]. The interaction is presented Fig. 2.7 via the exchange of a virtual photon (γ^*). While these interactions occur at the very beginning of the collision process and can provide useful information about the PDFs, the relative fraction of e$^+$e$^-$ pairs produced at LHC energies in the range this analysis is performed ($m_{\mathrm{ee}} < 3.5\,\mathrm{GeV}/c^2$) is negligible, and therefore these contributions are not considered during the analysis.

2.5 Thermal Dielectron Production

While the presence of a hot dense medium can modify the vector spectral functions in part due to a partial restoration of chiral symmetry, a hot medium can also emit thermal photons which can decay into a e$^+$e$^-$ pair. The electromagnetic spectral function to calculate the dielectron thermal emission rate per unit phase space in heavy-ion collisions can be written as
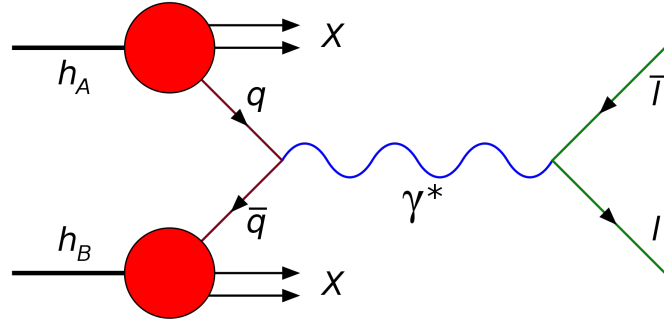
Figure 2.7: *A Feynman diagram of a Drell-Yan process [71]. A quark and antiquark from different hadrons annihilate and produce a lepton pair via the exchange of, in this case, a γ^*. The same process can be facilitated by a Z boson.*

$$\frac{\mathrm{d}N_{\mathrm{e^+e^-}}}{\mathrm{d}^4x\mathrm{d}^4p} = -\frac{\alpha_{\mathrm{EM}}L(m)}{\pi^3 m^2}f^B(E;T)\mathrm{Im}\Pi_{EM}(m,p;\mu_B,T), \qquad (2.3)$$

where α_{EM} is the electromagnetic coupling, $L(m)$ is a lepton phase-space factor (which goes to 1 for vanishing lepton masses), f^B denotes the thermal Bose distribution, $E = \sqrt{m^2 + p^2}$ is the energy of the lepton pair (or virtual photon) calculated with its invariant mass and 3-momentum, and $\mathrm{Im}\Pi_{EM}$ the partonic or hadronic in-medium spectral function [63]. To calculate the final contribution to the $\mathrm{e^+e^-}$ spectrum, both the partonic and hadronic in-medium spectral functions must be accounted for by integrating their contributions over a realistic space-time evolution of the collision using

$$\frac{\mathrm{d}N_{\mathrm{e^+e^-}}}{\mathrm{d}m_{\mathrm{ee}}} = \int d^4x \frac{m_{\mathrm{ee}}d^3p}{p_0}\frac{dN_{\mathrm{e^+e^-}}}{d^4xd^4p}. \qquad (2.4)$$

The in-medium spectral function from the partonic phase is based on QGP calculations from LQCD, whereas the hadronic phase spectral function is calculated using a hadronic many-body approach. A thermal fireball model is used to provide a system temperature which dictates the cross over from the partonic to the hadronic phase, along with an equation of state for both phases. In Fig. 2.8 the thermal contributions to dielectron production in Pb–Pb collisions at the LHC are shown [72]. For this calculation an ideal gas equation of state (EoS) for the partonic phase and resonance gas EoS for the hadronic phase was used. The vacuum spectral shape for the ρ^0, ω and ϕ mesons (free HG) is plotted alongside the hadronic in-medium modified spectral function (in-med HG), as well the spectral function from the partonic phase (QGP). In the low mass

region ($m_{ee} < 1.1\,\text{GeV}/c^2$) the thermal dielectrons from the hadronic gas phase are the dominant source, while in the intermediate mass range ($1.1 < m_{ee} < 2.7\,\text{GeV}/c^2$) the QGP contribution becomes dominant. The plot also indicates the expected dielectron yield from $c\bar{c}$ decays (DD) which are the dominant source in Pb–Pb collisions for $m_{ee} \gtrsim 0.4\,\text{GeV}/c^2$ and highlights why thermal dielectron measurements at LHC energies are very complex and need precise modelling of the heavy-flavour contributions so that they can be accurately subtracted. Thermal calculations for p–Pb collisions at $\sqrt{s_{\text{NN}}} = 5.02$ TeV are discussed and presented in Section 4.6.5, and are compared to the data in Chapter 5.
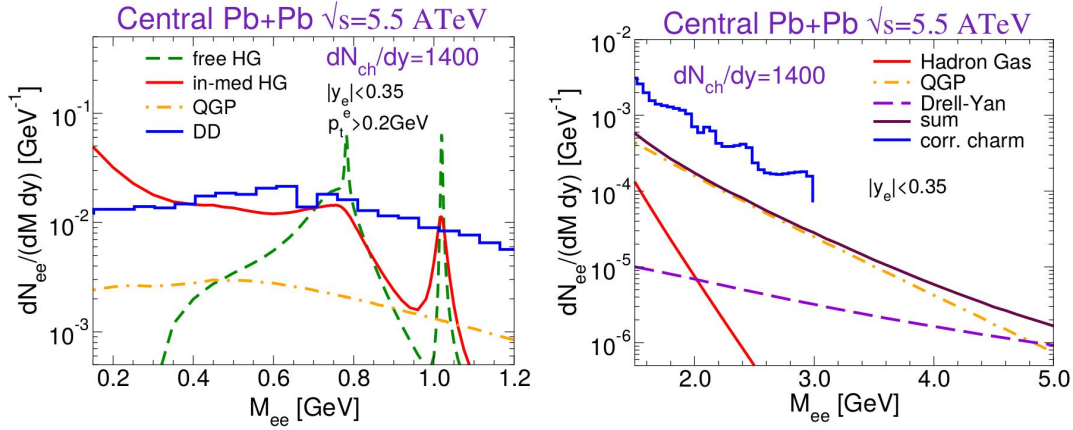
Figure 2.8: *Predicted thermal dielectron yield in Pb–Pb collisions at the LHC compared to the expected in-vacuum yield (green) [72]. Dielectron thermal contributions from both interactions in a hadron gas (red) and from the QGP (dotted yellow) are plotted separately. The expected dielectron yield from open heavy-flavour $c\bar{c}$ decays (blue) and Drell-Yan processes (purple) are also plotted.*

2.6 Previous Results

This section presents a selection of previous results with a focus on those that are particularly relevant to this thesis and is in no way comprehensive. With respect to the previously discussed QCD phase diagram (Fig. 1.3), the results shown here are extracted from collisions at small net baryon density with increasing temperatures, represented as a red line in Fig. 1.3.

Some of the first dielectron production measurements in both p–A and nucleus-nucleus collisions were performed in 1992 at the Super Proton Synchrotron at CERN by the CERES collaboration [73] in low energy collisions at $E_{\text{lab}} = 450$ GeV and $E_{\text{lab}} = 200$

AGeV, respectively. Invariant mass spectra were extracted from p–Au, p–Be and S–Au collisions and compared to the hadronic cocktail which contains the expected contributions from all known hadronic decays. The cocktail for the studies performed in this thesis are covered in detail in Section 4.6. As visible on the left in Fig. 2.9, no excess was observed in p–Au collisions with the data and expectation found to be in good agreement, as was also the case in p–Be collisions. On the right, however, a clear excess was observed in S–Au collisions, in particular in the lower mass region $0.2 < m_{ee} < 0.6 \, \text{GeV}/c^2$. Due to the onset of the excess at $m_{ee} \approx 2m_\pi$ and the dominant excess occurring in the ρ^0 mass region, it was explained as being the result of two-pion annihilation ($\pi\pi \rightarrow \rho^0 \rightarrow e^+e^-$). Two models were included to explain the observation; a dropping [74] or a broadening [60] of the ρ^0 mass, however the precision of the results prevented any definitive conclusions at the time.

(a) p–Be

(b) S–Au
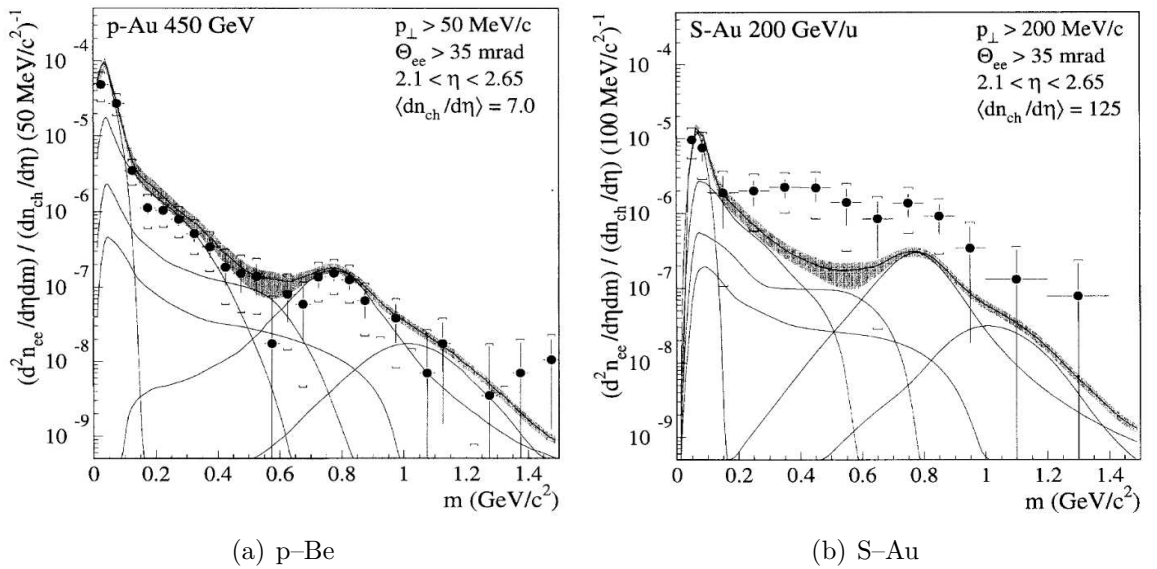
Figure 2.9: *Inclusive* e^+e^- *mass spectra in p–Be collisions (left) and S–Au collisions (right) recorded by the CERES collaboration at the CERN SPS, showing the data (full circles) and the various contributions from hadron decays (solid lines) [73]. The shaded region indicates the systematic error on the summed contributions. No pair acceptance corrections are applied.*

Nearly a decade later, the CERES [75] and NA60 [76] collaborations were both able to measure the ρ^0 spectral shape in nucleon-nucleon collisions at $E_{\text{lab}} = 158$ AGeV with much higher precision. The e^+e^- yield, after the subtraction of the expected hadronic contributions, measured by the upgraded CERES experiment in Pb–Au collisions is shown on the left in Fig. 2.10, and on the right the remaining dimuon mass spectrum

after hadronic subtraction measured in In–In collisions by the NA60 collaboration is shown alongside the vacuum ρ^0 expectation (solid black). In both measurements the broadening of the ρ^0 spectral function was found to be consistent with the theoretical predictions, accompanied by an excess due to thermal production of ρ^0 mesons, and the mass dropping scenario was essentially ruled out. This was followed up by another NA60 measurement which investigated the intermediate mass range ($m_{ee} > 1.1\,\text{GeV}/c^2$) and was able to show evidence for partonic thermal radiation [77].

(a) m_{ee} (b) $m_{\mu\mu}$
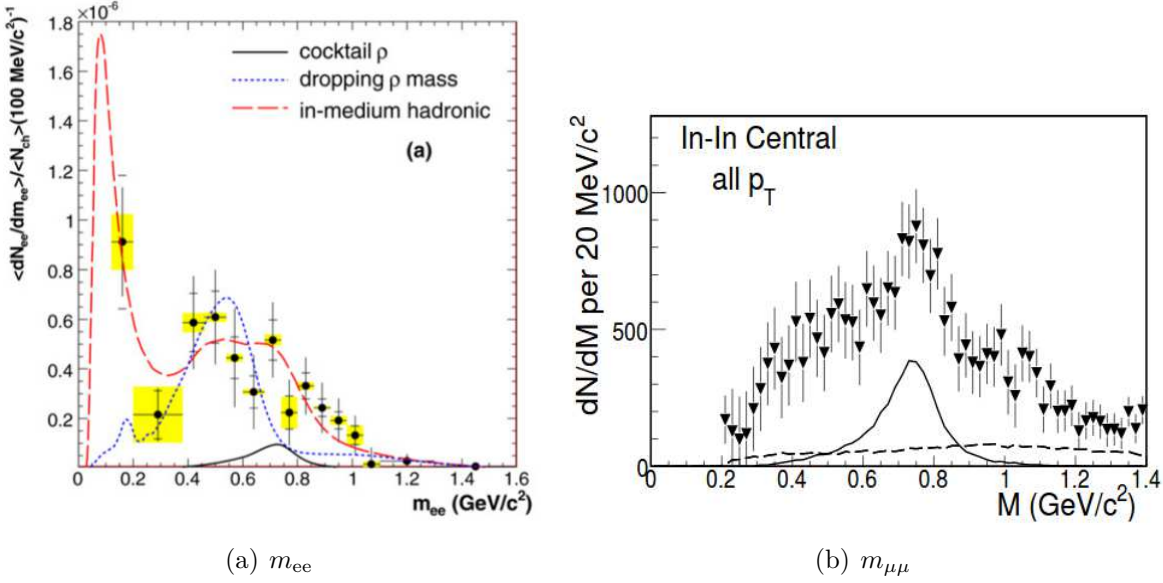
Figure 2.10: *Measured dilepton spectra after the subtraction of the known hadronic sources (excluding the ρ^0 meson) by CERES (left) in Pb–Au collisions [75] and by the NA60 collaboration (right) in In–In collisions [76] both at $E_{\text{lab}} = 158\ AGeV$.*

More recently, the PHENIX and STAR collaborations, which operate at the relativistic heavy-ion collider (RHIC) located at the Brookhaven National Laboratory, both performed dielectron measurements in pp, d–Au and Au–Au collisions at $\sqrt{s_{\text{NN}}} = 200$ GeV [78, 78–82]. The e^+e^- spectrum measured in pp collisions was consistent with calculations only including known hadronic sources. By measuring d–Au at the same energy, it was also possible to calculate the nuclear modification factor for $c\bar{c}$ and $b\bar{b}$ production, as shown in Fig. 2.11, where no observable deviation from unity was found within the large uncertainties. In Fig. 2.12 the measured m_{ee} spectrum in Au–Au collisions are shown for PHENIX (left) and STAR (right). Both collaborations reported an excess in the low mass region around the peak of the ρ^0 meson that could not be explained with a pure vacuum ρ^0. On the right in Fig. 2.12, two additional thermal models

were compared to the data. In red is the thermal model outlined in Section 2.5, and in dotted blue is a model not covered in this thesis but it is known as Parton-Hadron-String Dynamics (PHSD) which uses a microscopic off-shell transport approach to describe the full evolution of a HIC. Both collaborations also reported hints of a possible thermal excess in the intermediate mass region ($1.1 < m_{ee} < 2.7\,\mathrm{GeV}/c^2$), however large contributions from correlated heavy-flavour decays coupled with the significant uncertainties of the expected yield calculations meant no concrete conclusions could be drawn.

(a) m_{ee} (b) $p_{\mathrm{T},ee}$
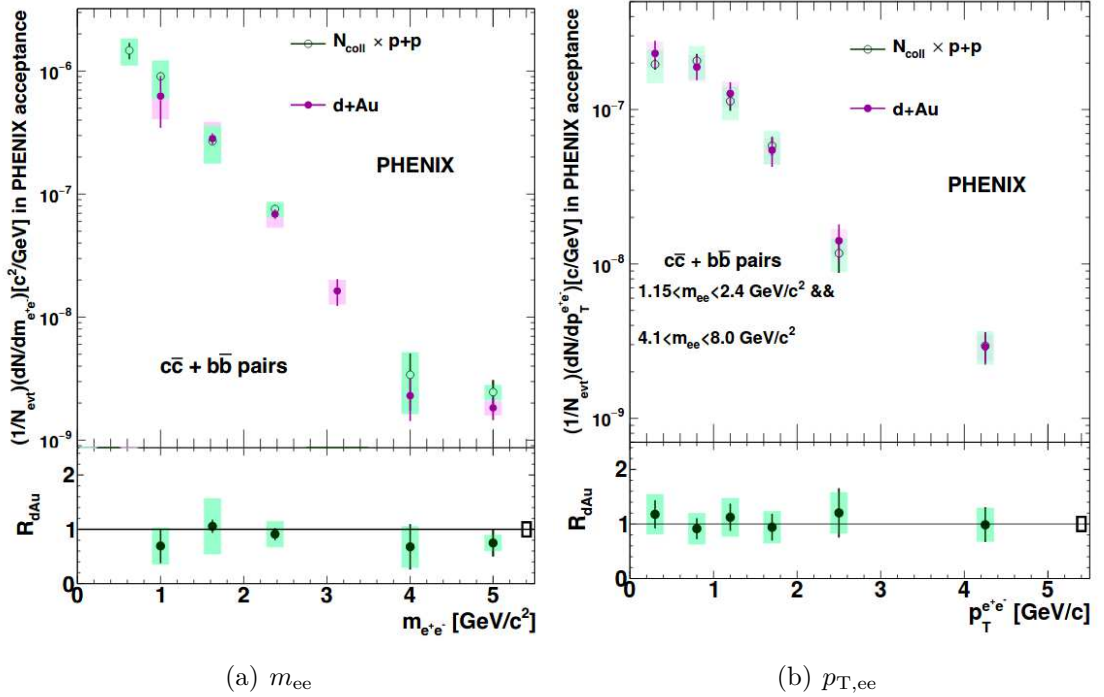
Figure 2.11: *Nuclear modification factors measured in d+Au collisions at $\sqrt{s_{\mathrm{NN}}} = 200$ GeV by PHENIX [80] as a function of m_{ee} (left) and $p_{\mathrm{T},ee}$ (right).*

Moving to the high energy regime, $\mathrm{e^+e^-}$ measurements have recently been performed at the LHC by ALICE in both pp collisions at $\sqrt{s} = 5.02$, 7 and 13 TeV [83–85], as well as in Pb–Pb collisions at $\sqrt{s_{\mathrm{NN}}} = 2.76$ TeV [86]. The dielectron spectra measured in pp collisions at $\sqrt{s} = 7$ and 13 TeV are shown in Fig. 2.13 and were found to be in agreement with the vacuum expectation of dielectrons from hadron decays. While the Pb–Pb measurement, shown in Fig. 2.14, has a hint of an excess in the low mass region where the data is compatible with both model calculations (the same two models previously discussed alongside the STAR Pb–Pb results), the measurement was limited by the small data set.

Measurements of open-charm hadron production [87, 88] including their decay elec-

(a) PHENIX

(b) STAR
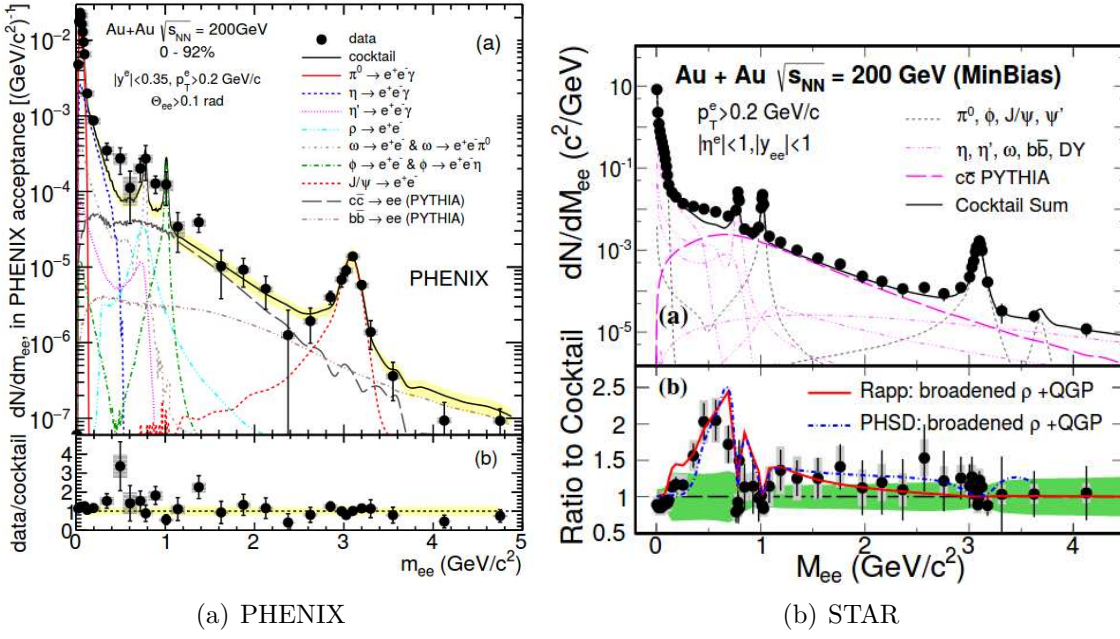
Figure 2.12: *Dielectron yields measured by PHENIX (left) and STAR (right) in Au–Au collisions at $\sqrt{s_{\mathrm{NN}}} = 200$ GeV [81, 82].*

(a) $\sqrt{s} = 7$ TeV

(b) $\sqrt{s} = 13$ TeV
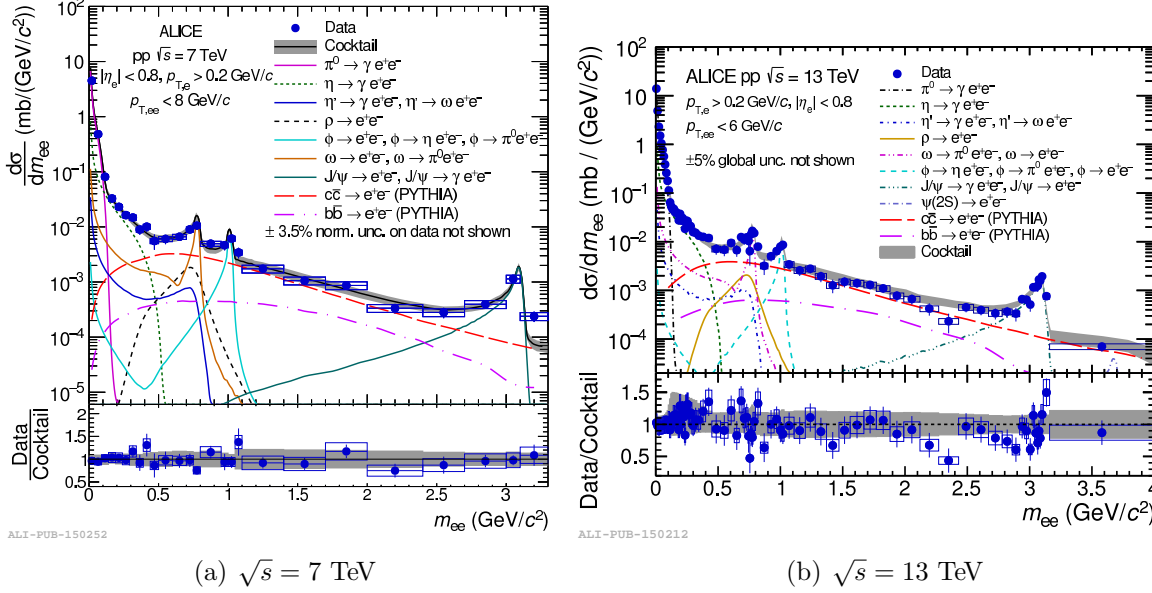
Figure 2.13: *Dielectron yield measured by ALICE in pp collisions at $\sqrt{s} = 7$ and 13 TeV [84, 85].*
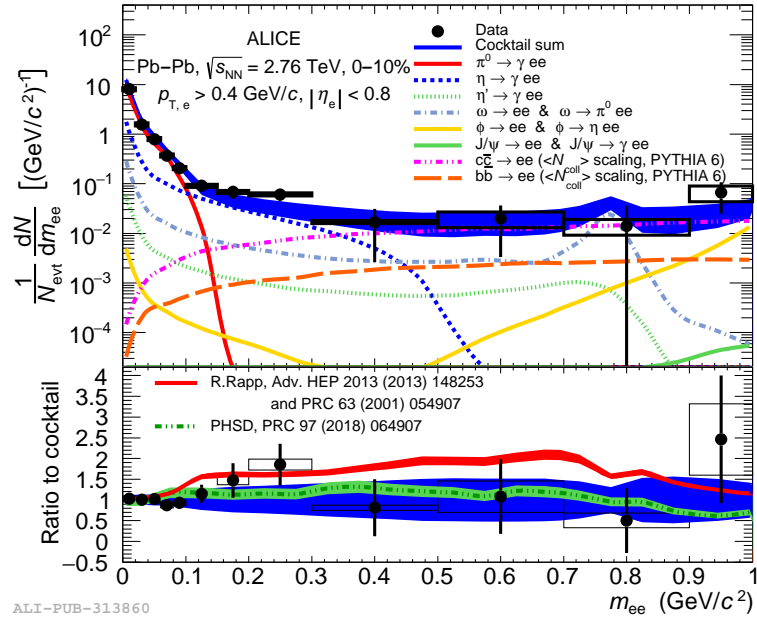
Figure 2.14: *Dielectron yields measured by ALICE in Pb–Pb collisions at $\sqrt{s_{NN}} = 2.76$ TeV compared to two models which include thermal contributions [86].*

trons [89, 90], along with measurements of the azimuthal correlations of D mesons and charged particles [91], are all compatible with measurements performed in pp collisions scaled by A (A = 208). The R_{pPb} from the single-leg electron measurements is shown on the left hand side of Fig. 2.15 and is compatible with unity within the large systematic uncertainties, as well as the additional models that were drawn (including one using EPS09 which is presented in detail in Section 4.6.5). However, measurements of prompt J/ψ production and J/ψ production from B hadron decays in p–Pb collisions at $\sqrt{s_{NN}} = 5.02$ TeV indicate a suppression at very low p_T [92], as shown on the right in Fig. 2.15, and agree with A scaling for larger p_T. Such measurements point towards any potential CNM effects affecting heavy-flavour production at midrapidity being quite small.. This is contrast to similar measurements at forward and backward rapidities which seem to confirm the presence of shadowing [93–95].

Measured e$^+$e$^-$ production in pp collisions at $\sqrt{s} = 5.02$ TeV

Most relevant to this thesis are the recently published dielectron production measurements in pp collisions at midrapidity at $\sqrt{s} = 5.02$ TeV [83]. This is the first time at LHC energies that dielectron measurements in both pp and p–Pb collisions at the same energy are available, enabling a direct comparison between the systems without having
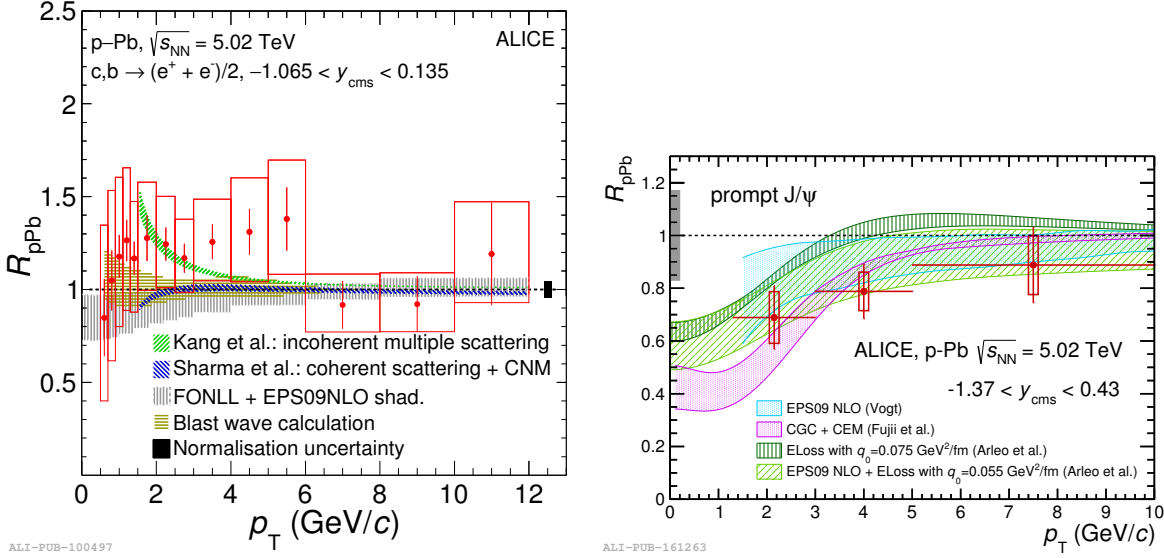
Figure 2.15: *Left: Nuclear modification factor (R_{pPb}) of electrons from heavy-flavour hadron decays as a function of p_T measured in p–Pb collisions at $\sqrt{s_{NN}} = 5.02$ TeV [89]. Right: prompt J/ψ R_{pPb} as a function of p_T measured by ALICE in collisions at $\sqrt{s_{NN}} = 5.02$ TeV [92].*

to resort to scaling which naturally introduces uncertainties (for example, previous di-electron comparisons by ALICE have used Fixed Order + Next-to-Leading Logarithms (FONLL) [96, 97] calculations to obtain the scaling factor).

For the pp analysis, two event generators were used to simulate the shape of the heavy-flavour contributions, POWHEG and PYTHIA 6.4[2], and were fit to the data via a double differential fit in m_{ee} and $p_{T,ee}$ in the intermediate mass region ($1.1 < m_{ee} < 2.7$ GeV/c^2). In Fig. 2.16 the fits using both generators are presented along side the data. While both generators are able to fit the data very well, the goodness of fit, evaluated with the χ^2/n.d.f, showed slightly better agreement when using POWHEG ($\chi^2 = 110.9/123$) than for PYTHIA 6.4 ($\chi^2 = 113.4/123$). The cross sections for c$\bar{c}$ and b$\bar{b}$ at midrapidity ($d\sigma_{c\bar{c}}/dy|_{y=0}$ and $d\sigma_{b\bar{b}}/dy|_{y=0}$) were also extracted and are presented in Table 2.1. The statistical and systematic uncertainties are from the data itself, with the additional uncertainty arising from the semi-leptonic decay branching ratios of the open heavy-flavour hadrons and fragmentation functions. This amounts to an uncertainty of 22% and 6% for the charm and beauty cross sections, respectively. While the differences in the fits to the dielectron spectrum between the generators were somewhat small, the measured cross sections show non-negligible differences between the two. This highlights the potential

---

[2]In both cases the hadronisation was performed with PYTHIA 6.4. See Section 4.6.2 for a description of these generators.

sensitivity of dielectron analyses to the heavy-flavour production mechanisms and is an exciting prospect for the future.
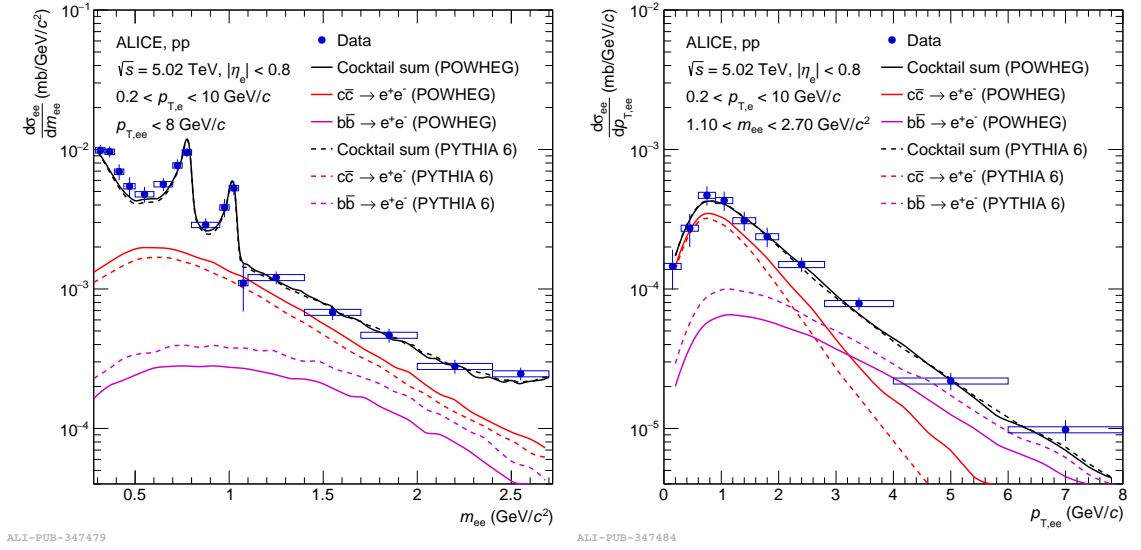
Figure 2.16: *Measured dielectron production at midrapidity in pp collisions at $\sqrt{s} = 5.02$ TeV as a function of m_{ee} (left) and $p_{T,ee}$ (right) [83]. The heavy-flavour contributions were generated using PYTHIA 6.4 (dashed lines) and POWHEG (solid lines) and are shown after a double-differential fit in m_{ee} and $p_{T,ee}$ performed in the intermediate mass region ($1.1 < m_{ee} < 2.7$ GeV/c^2).*

	PYTHIA	POWHEG
$\mathrm{d}\sigma_{c\bar{c}}/\mathrm{d}y\big|_{y=0}$	$524 \pm 61 \pm 26 \pm 115\,(\mathrm{BR})\,\mu\mathrm{b}$	$756 \pm 80 \pm 38 \pm 166\,(\mathrm{BR})\,\mu\mathrm{b}$
$\mathrm{d}\sigma_{b\bar{b}}/\mathrm{d}y\big|_{y=0}$	$34 \pm 4 \pm 2 \pm 2\,(\mathrm{BR})\,\mu\mathrm{b}$	$28 \pm 5 \pm 1 \pm 2\,(\mathrm{BR})\,\mu\mathrm{b}$

Table 2.1: *Heavy-flavour cross sections extracted via double differential fits in m_{ee} and $p_{T,ee}$ to the measured dielectron production in pp collisions at $\sqrt{s} = 5.02$ TeV at midrapidity using PYTHIA 6.4 and POWHEG [83]. The statistical and systematic uncertainties of the data are quoted along with the 22% (charm) and 6% (beauty) uncertainty of the branching ratio (BR) of the decays.*

These recent cross section measurements at $\sqrt{s} = 5.02$ TeV are put into context in Fig. 2.17 where they are compared to other heavy-flavour cross sections measured in dielectron analyses at $\sqrt{s} = 7$ and 13 TeV. Also plotted are the FONLL predictions, as well as cross sections from a measurement of prompt D^0 mesons for $c\bar{c}$ and a measurement of single heavy-flavour hadron measurements for $b\bar{b}$. FONLL calculations reproduce the slope of the dielectron measurements quite well, and are in agreement due to the large

uncertainties from FONLL. The dielectron c$\bar{\text{c}}$ cross section measurements are systematically above the FONLL central value for both generators and at $\sqrt{s} = 7$ TeV the D^0 measurement is in agreement with both generators. Similar differences between the generators are present for the b$\bar{\text{b}}$ cross section measurements, however in this case the PYTHIA 6.4 results are slightly above the central FONLL calculation and POWHEG slightly below.
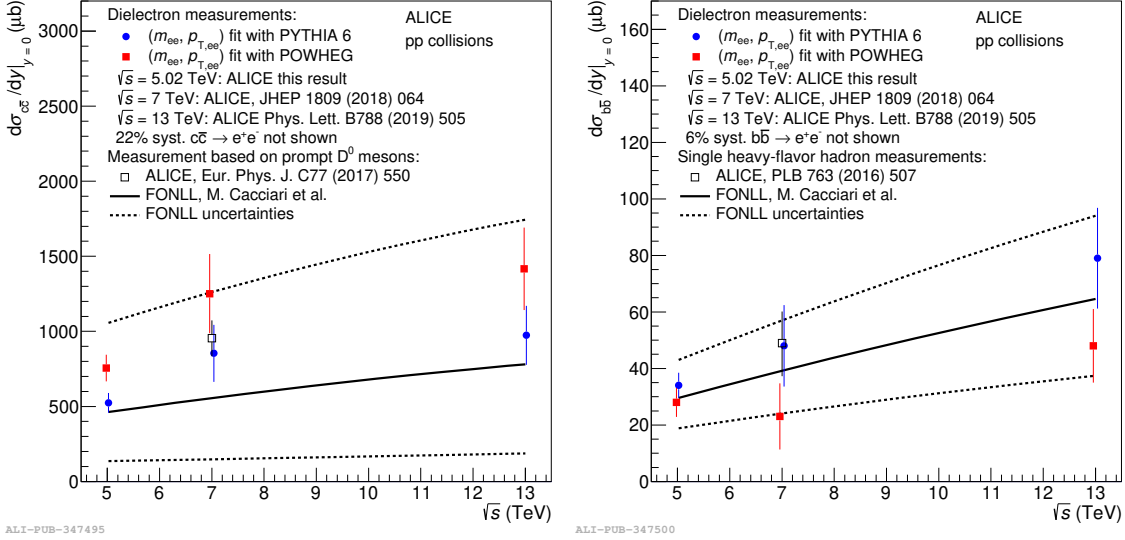
Figure 2.17: *Mid-rapidity cross sections for* c$\bar{\text{c}}$ *(left) and* b$\bar{\text{b}}$ *(right) measured in pp collisions at $\sqrt{s} = 5.02$ TeV [83]. The red and blue markers indicate fits to dielectron measurements using POWHEG and PYTHIA 6.4 for the simulations, respectively. The black line represents FONLL calculations, along with the associated uncertainties shown as black dashed lines. The open markers represent single heavy-flavour hadron measurements.*

Also found in [83] are the final dielectron production measurements as a function of m_{ee}, as well as a function of $p_{\text{T,ee}}$ in two mass ranges ($0.5 < m_{\text{ee}} < 1.1\,\text{GeV}/c^2$ and $1.1 < m_{\text{ee}} < 2.7\,\text{GeV}/c^2$). The measurements were compared to the expected dielectron production using the better fitting POWHEG to generate the heavy-flavour contributions with all the light-flavour contributions grouped together under "Light-flavor" (see Table 4.7 for a complete list). The uncertainty of the calculations, shown in grey, is zero by construction for $1.1 < m_{\text{ee}} < 2.7\,\text{GeV}/c^2$ as this is the range where the calculations were fit to the data. The dielectron production measurement as a function of m_{ee} is shown in Fig. 2.18 and as a function of $p_{\text{T,ee}}$ in Fig. 2.19. A good agreement between the data and calculations is evident in all cases. These dielectron measurements are used in the final chapter of this thesis, Section 5.3, to produce the

nuclear modification factors discussed earlier.

In summary, dielectron measurements have significantly contributed to the understanding of HICs and QCD in general. With many facets of HICs still not understood, in particular with respect to the physics occurring in small systems, dielectrons are again an ideal probe to try answer these questions. Two currently open questions are the magnitude of the CNM effects in small systems, in particular at higher (LHC) energies, which have until now suffered from large uncertainties in the measurements; as well as determining the presence of any thermal radiation in small systems. These are the primary investigations undertaken in this thesis which measures dielectron production in p–Pb collisions at $\sqrt{s_{\mathrm{NN}}} = 5.02$ TeV measured with the ALICE detector.
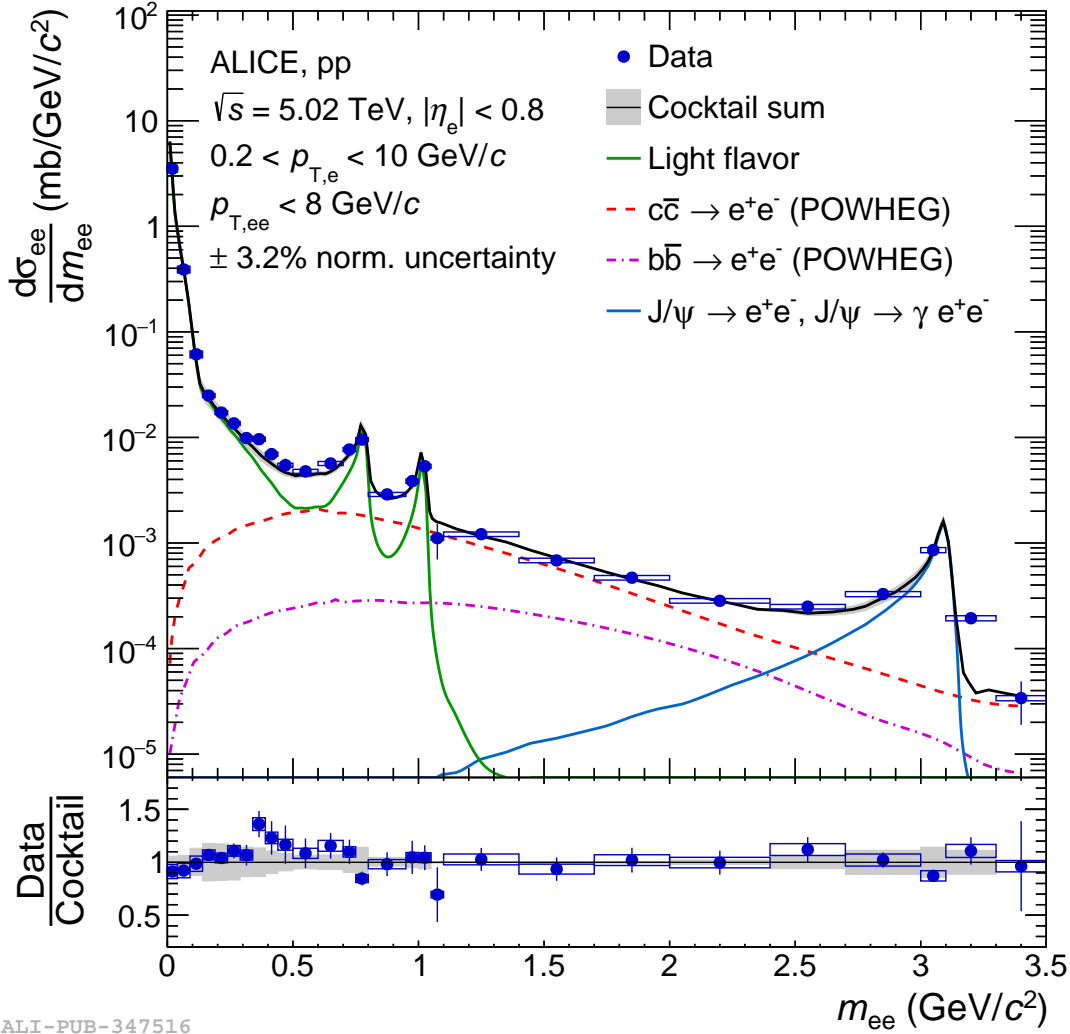
Figure 2.18: *The dielectron cross section measured in pp collisions at $\sqrt{s_{NN}} = 5.02$ TeV as function of m_{ee} integrated over the range $0 < p_{T,ee} < 8$ GeV/c [83]. The data are compared to a hadronic cocktail with the heavy-flavour contributions produced with POWHEG and fit to the data in the intermediate mass range $(1.1 < m_{ee} < 2.7$ GeV/c^2). The grey band represents the systematic uncertainty of the hadronic cocktail. The lower panel shows the ratio of the data over the hadronic cocktail.*

(a) $0.50 < m_{ee} < 1.10\,\mathrm{GeV}/c^2$

(b) $1.10 < m_{ee} < 2.70\,\mathrm{GeV}/c^2$
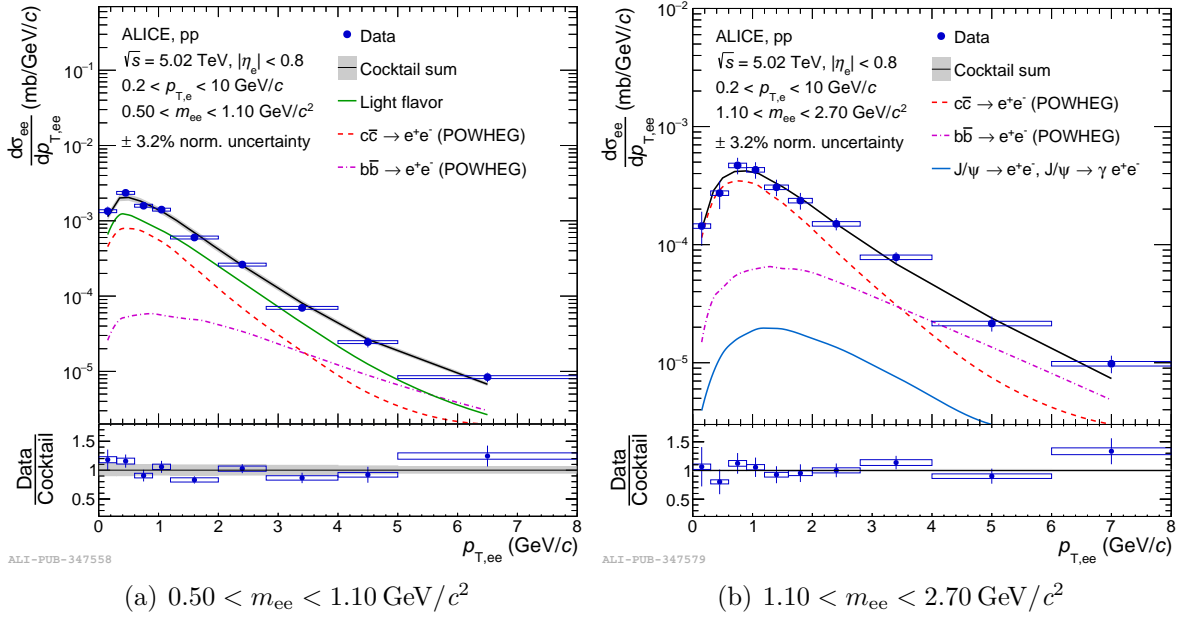
Figure 2.19: *The dielectron cross section measured in pp collisions at $\sqrt{s_{\mathrm{NN}}} = 5.02$ TeV as function of $p_{\mathrm{T,ee}}$ in two mass intervals [83]. The data are compared to a hadronic cocktail with the heavy-flavour contributions produced with POWHEG and fit to the data in the intermediate mass range ($1.1 < m_{ee} < 2.7\,\mathrm{GeV}/c^2$). The grey band represents the systematic uncertainty of the hadronic cocktail. The lower panel shows the ratio of the data over the hadronic cocktail.*

3 ALICE Detector

THE ALICE DETECTOR

a. ITS SPD (Pixel)
b. ITS SDD (Drift)
c. ITS SSD (Strip)
d. V0 and T0
e. FMD

1. ITS
2. FMD, T0, V0
3. TPC
4. TRD
5. TOF
6. HMPID
7. EMCal
8. DCal
9. PHOS, CPV
10. L3 Magnet
11. Absorber
12. Muon Tracker
13. Muon Wall
14. Muon Trigger
15. Dipole Magnet
16. PMD
17. AD
18. ZDC
19. ACORDE
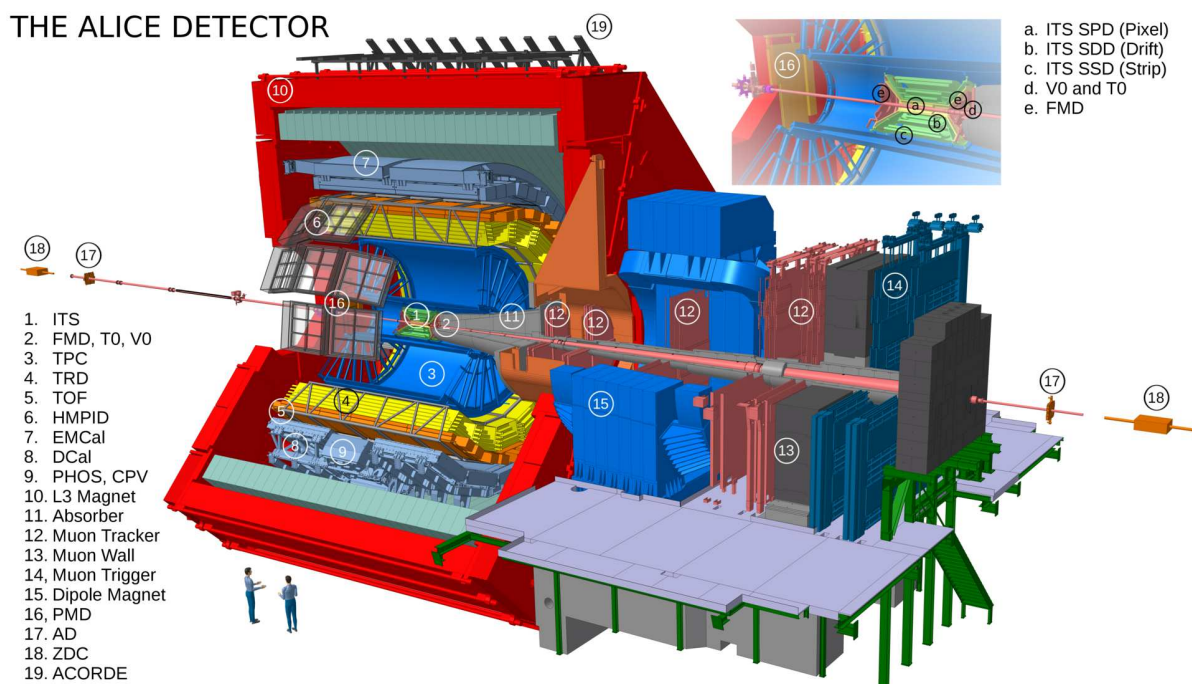
Figure 3.1: *A schematic overview of the ALICE detector during the LHC Run 2 data taking period [3]. The plot in the upper right corner is a closer view of the Inner Tracking System and the surrounding forward detectors (see plot legend).*

3.1 Overview

The ALICE (A Large Ion Collider Experiment) collaboration [4] operates one of the big four detectors operating at the LHC (Large Hadron Collider), which is located at CERN on the outskirts of Geneva, Switzerland. The ALICE detector was primarily designed to study strongly interacting matter produced in heavy-ion collisions, typically Pb–Pb, where the high energy and densities reached in the collisions are thought to create a QGP. However, the detector also records data from pp and p–Pb collisions, which are in fact necessary to establish a baseline reference for the Pb–Pb results. The general

37

performance of the ALICE detector is covered in detail in [98]. The ALICE detector is comprised of 19 primary components and can be seen in Fig. 3.1 where a schematic of the ALICE detector as operated during LHC Run 2 (2015-2018) is shown. These detector components can be grouped into two separate sections. The first is the central barrel of the detector that houses the commonly referred to *central barrel detectors*, which are used in this thesis and will be covered in the following text in more detail. The second detector section is the *forward muon arm*, whose acceptance covers the pseudorapidity range $2.5 < \eta < 4$, and is mainly used to study heavy quarkonia spectra via their dimuon decay channels.

The central barrel detectors, covering the pseudorapidity range $|\eta| < 0.9$, are surrounded by a large solenoid, which generates a uniform magnetic field up to 0.5 Tesla along the beam axis direction. These detectors provide vertex reconstruction, tracking and Particle IDentification (PID) capabilities, in addition to event timing and multiplicity estimations. The core detectors for this analysis are the Inner Tracking System (ITS), covered in Section 3.2, the Time Projection Chamber (TPC), covered in Section 3.3, the Time-Of-Flight (TOF) detector, covered in Section 3.4, and the V0 detectors, covered in Section 3.5.

To reconstruct the tracks of the charged particles passing through the detector, the ITS and TPC track points are used by a Kalman-filter based algorithm [99, 100]. Following the initial fit, these tracks can be paired to other central barrel detectors, for example, the Transition Radiation Detector (TRD), in order to further improve the tracking quality. The track's transverse momentum (p_T) can be calculated with

$$p_T = \left(0.3\frac{GeV}{Tm}\right) \cdot qrB,$$

(3.1)

where B is the magnetic field strength, r the radius of the track, and q the charge of the track. Additional detectors are located close to the beam pipe and are used to measure the collision time, event multiplicity, as well as being used for triggering. To determine the event collision time in low multiplicity events, the T0 detector [101], located up and downstream from the nominal interaction point, is used. For higher multiplicity events, the TOF detector, or a combination of the TOF and T0 inputs, are used [102]. The T0 detectors are comprised of 12 Cherenkov counters in an array, and can obtain a precision of < 25 ps. The V0 detector [103], outlined in Section 3.5, is used both for the minimum-bias (MB) trigger, defined by coincident signal in both V0 detectors, and for rejection of potential background events, which are discussed in Section 4.1.

3.2 Inner Tracking System

The primary goals of the ITS are precise primary vertex reconstruction, with a resolution down to 100 μm, the ability to reconstruct secondary vertices from long lived particles, e.g., D and B mesons, as well the ability to track and identify low-p_T ($p_\mathrm{T} < 0.2\,\mathrm{GeV}/c$) particles [4, 104]. The ITS encases the central beam pipe with the first and last layers at a radius of 4 cm and 43.6 cm, respectively. In total, the ITS has six layers which are comprised of three different types of silicon detectors.
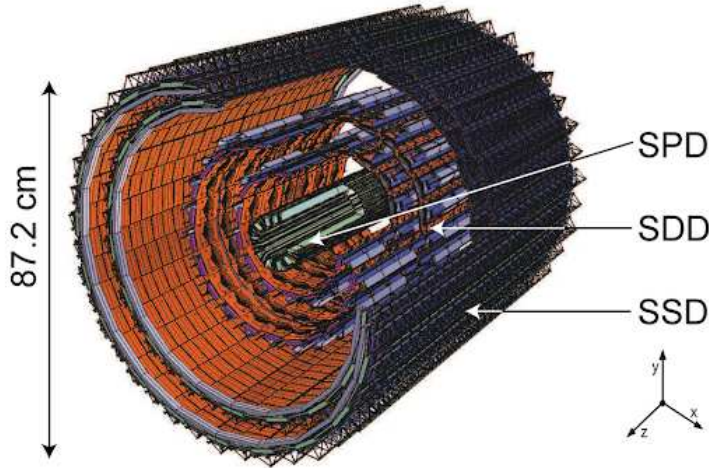
Figure 3.2: *A diagram of the ALICE Inner Tracking System showing the three different silicon detector types used [105]. The inner two layers are silicon pixel detectors (SPD), the third and fourth layers are silicon drift detectors (SDD), and the outer two layers are silicon strip detectors (SSD).*

As shown in Fig. 3.2, the inner two layers are Silicon Pixel Detectors (SPD), the third and fourth layers are Silicon Drift Detectors (SDD), and the outer two layers are Silicon Strip Detectors (SSD). The outer four layers operate with an analogue readout enabling their use not only for tracking but also for low-p_T PID via the specific energy loss ($\mathrm{d}E/\mathrm{d}x$) of the traversing track (see Section 3.3 for an overview). However, due to the high interaction rates during the 2016 p–Pb data taking period and the slow readout time of the SDD ($\sim$6.4 μs), approximately half of the events were recorded without information from the SDD layers. Since at least three out of the four analogue ITS layers must record a valid signal in order for a reliable $\mathrm{d}E/\mathrm{d}x$ calculation, half the data set does not contain a reliable $\mathrm{d}E/\mathrm{d}x$ measurement from the ITS, as well as having two less track points used during track fitting. The ramifications of this on the analysis are discussed in more detail in Section 4.2.1.

For low-p_T tracks, the tracking resolution is dominated by multiple scattering interactions of the track with the detector material, which stipulated that the material budget of the ITS was kept to a minimum. Conversely, to keep the signal-to-noise ratio to a minimum, the silicon detectors in the SSD and SDD layers were required to have a minimum thickness of 300 μm. In total, the detectors effective thickness only amounts to 8% of the radiation length (X_0), which is particularly important for dielectron analyses as this reduces the probability that real photons would interact with the detector and convert into an e^+e^- pair. Due to the imperfect tracking resolution, e^+e^- pairs from photon conversions can appear to have a non-zero m_{ee} ($m_{ee} \lesssim 0.14\,\mathrm{GeV}/c^2$). These conversion pairs can be relatively easily removed from the final signal, however they can dramatically increase the combinatorics of the pairing procedure which greatly reduces the significance of the final measurement. The significance of the measurement and the methods employed to suppress tracks originating from photon conversions are covered in Section 4.3.

3.3 Time Projection Chamber

The TPC is the core detector of ALICE, which provides not only charged-particle tracking, but also excellent PID and vertex reconstruction [4, 106]. The TPC, with a length of 510 cm, surrounds the ITS and extends out to a radius of 250 cm. A diagram of the TPC can be seen in Fig. 3.3. A uniform electrostatic field is produced by the field cage, which contains a central high-voltage electrode and two opposite axial potential dividers. Contained within the field cage is a gaseous mixture, which in 2016, when the data used in this thesis was taken, was a 88/12 mixture of Ar/CO_2. A high electric field of 400 V/cm is maintained, causing a drift velocity of $\sim$2.7 cm/μs, which results in a maximum drift time of $\sim$92 μs. The end caps contain a radially-segmented multiwire proportional readout system which provides up to 159 space-time points for the traversing tracks.

To identify a particle species in the TPC, both the p_T and the dE/dx of the track are measured. In the region $0.1 \lesssim \beta\gamma \lesssim 1000^1$, the Bethe-Bloch formula can describe the mean dE/dx of a relativistic charged particle to within a few percent [5], and can be written as:

---

[1] The Lorentz factor is defined as $\gamma = \frac{1}{\sqrt{1-\beta^2}}$, and $\beta = \frac{v}{c}$ where v is the relative velocity.
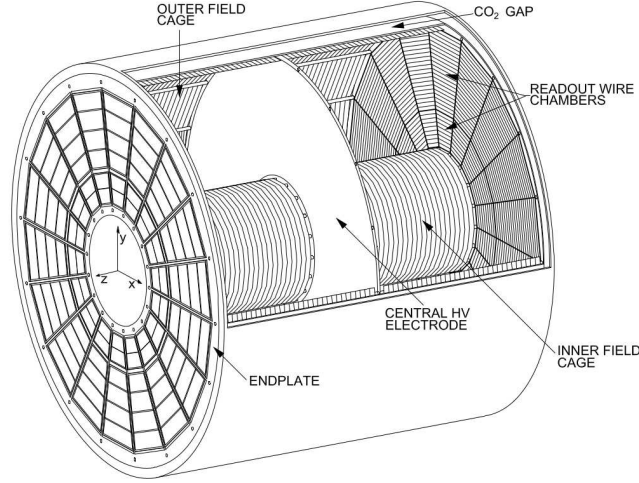
Figure 3.3: *A diagram of the ALICE Time Projection Chamber [107].*

$$\left\langle -\frac{\mathrm{d}E}{\mathrm{d}x} \right\rangle = K z^2 \frac{Z}{A} \frac{1}{\beta^2} \left[ln\left(\frac{2 m_e c^2 \beta^2 \gamma^2}{I} \right) - \beta^2 \right] \tag{3.2}$$

where K is a constant, Z the atomic number, A the mass number, I the mean excitation energy, and z the electric charge of the traversing particle. In Fig. 3.4, the $\mathrm{d}E/\mathrm{d}x$ for a μ^+ in Cu is shown for $0.1 \ \mathrm{MeV}/c < p_\mathrm{T} < 100 \ \mathrm{TeV}/c$, with the valid range for the Bethe-Bloch formula depicted between the second and third vertical grey bands. The PID capabilities of the TPC are crucial for dielectron analyses, and are covered in detail in Section 4.2.2.

3.4 Time of Flight Detector

The TOF detector is a Multi-gap Resistive-Plate Chamber detector designed as a cylindrical shell with an inner radius of 370 cm and outer radius of 399 cm [4, 109]. The frame of the detector and a single module are shown in Fig. 3.5. The total thickness of the detector ultimately corresponds to 30% of a radiation length. It is built in a modular fashion ,with 18 sectors in the φ direction, and five segments in the z direction, resulting in a polar acceptance of $|\theta - 90| < 45°$ and pseudo-rapidity range of $|\eta| < 0.9$. A highly uniform electric field is maintained over each module so that a traversing track will ionise the gas and immediately start an avalanche process, which is recorded at the electrodes. In contrast to other gaseous detectors, the high electric field and small width of the chambers ensures that there is no drift time associated to each track, rather the

41
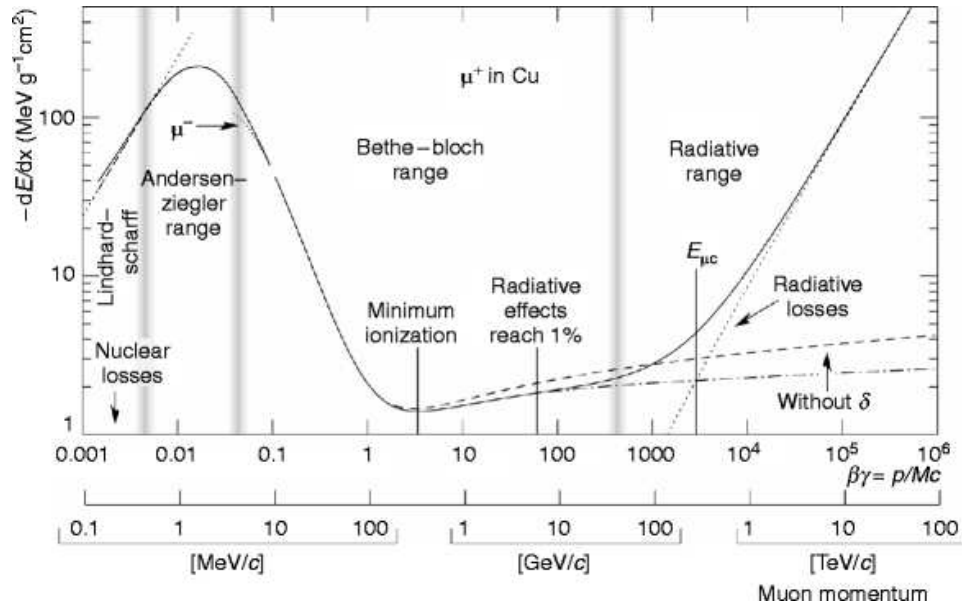
Figure 3.4: *The specific energy loss (dE/dx) for a positive muon (μ^+) in copper (Cu) as a function of the particles momentum. Between the second and third grey vertical bars is the region where the Bethe-Bloch parametrisation of dE/dx is applicable [108].*

time jitter of the detector is a result of the growth of the initial avalanche. During the Run 2 period in 2016, when the data for this thesis was taken, the TOF reached a timing resolution of 56 ps [110].

Analogously to the dE/dx measurements in the ITS and TPC, the TOF detector can provide PID information by measuring the time-of-flight of the track, and has strong separating power between electrons and identified hadrons in the intermediate-p_T range, which complements the capabilities of the ITS and TPC. This is covered in more detail in Section 4.2.2.

3.5 V0 Scintillators

The V0 detector consists of two arrays of scintillators, with the V0A detector situated 340 cm from the interaction point, and the V0C detector located on the front face of the hadronic absorber at only 90 cm from the interaction point. The detectors cover the ranges $2.8 < \eta < 5.1$ for the V0A, and $-3.7 < \eta < -1.7$ for the V0C. One of the primary purposes of the V0 detector is to provide a minimum-bias trigger for the central barrel detectors, where the particles providing the trigger can be generated in the initial collision, as well as from secondary interactions. Additionally, since the relationship
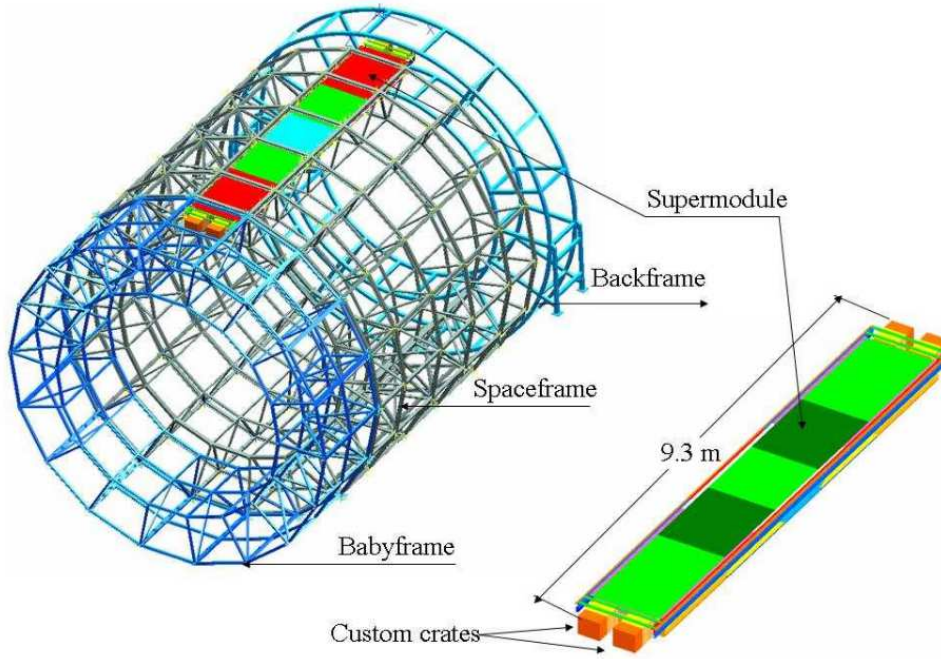
Figure 3.5: *A schematic drawing of the Time-Of-Flight detectors frame used by ALICE as well one of the supermodels [4].*

between the number of primary particles and the number of tracks registered in the V0 is monotone, the V0 signals can be used to estimate the multiplicity of event, which in Pb–Pb collisions can be used to estimate the centrality. The standard MB trigger, used in this analysis, requires a coincident signal between both V0 modules. Finally, the V0 detector is also used to calculate the beam luminosity.
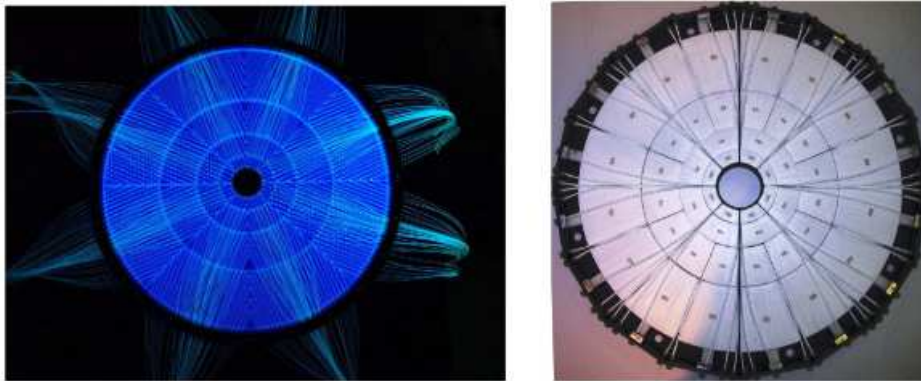
Figure 3.6: *The V0A (left) and V0C (right) detectors shown from the front [4].*

43

4 Analysis

This section details the treatment and analysis of the data and corresponding Monte Carlo (MC) simulations. It begins with the event selection, covered in Section 4.1, followed by the track selection and electron identification criteria, covered in Section 4.2.2. The signal extraction method, from the electron-positron pairing procedure to the photon conversion rejection techniques, is detailed in Section 4.3. The reconstruction efficiency correction is presented in Section 4.4, followed by the systematic uncertainties of the final results in Section 4.5. In Section 4.6, the procedure to simulate the expected dielectron production in p–Pb collisions at $\sqrt{s_{\mathrm{NN}}} = 5.02$ TeV is detailed.

4.1 Data Set and Event Selection

The data set used in this thesis was recorded by the ALICE collaboration in p–Pb collisions at $\sqrt{s_{\mathrm{NN}}} = 5.02$ TeV performed during Run 2 in 2016. As a result of the asymmetric beam energies in p–Pb collisions in the centre-of-mass system, with 4 TeV for the proton beam and 1.59 TeV per nucleon for the Pb beam, the rapidity (y) distribution is slightly shifted by $\Delta y = 0.465$ with respect to the laboratory frame in the direction of the proton beam. The MB trigger (defined in Section 3.1) was used to select events, in combination with the LHC's central beam crossing clock. The number of triggered events (N_{MB}) along with the integrated luminosity $(\mathcal{L}_{int})$ is listed in Table 4.1, with $\mathcal{L}_{int}$ calculated as

$$\mathcal{L}_{int} = N_{\mathrm{MB}}/\sigma_{\mathrm{MB}}, \tag{4.1}$$

where σ_{MB} is the MB cross section (2.09 b $\pm$ 3.7%) measured with a van der Meer scan [111]. To be considered for the analysis, the triggered events must also satisfy the following conditions:

- The triggered event must contain at least one primary track (defined in Section 4.2.1) which can be used to reconstruct the collision vertex.

- The tracks used for the vertex reconstruction must have at least one hit in the SPD layers of the ITS.

- The reconstructed collision vertex must be within ± 10 cm of the nominal interaction point along the beam axis, so as to avoid any edge effects of the central barrel detectors.

Further conditions are placed on the event selection to ensure that no events containing the products from more than one collision are included in the analysis. These *pileup* events come in two primary categories. The *same-bunch-crossing pileup* covers when two or more collisions take place within one bunch[1] crossing. This type of pileup is observed by all detectors. The second type is *out-of-bunch pileup* and includes pileup originating from collisions between bunches that were not responsible for triggering the event, as well collisions between the beam and residual gas in the beam pipe. This type of pileup primarily affects detectors with longer than average read out times, and differs from the first type of pileup as the reconstructed points in the drift detectors, e.g., SDD and TPC, will be spatially shifted in the drift direction of the detector. There are two separate approaches to deal with event pileup. The first covers both types of pileup, and is applied at the event selection level by rejecting any events that are reconstructed with a certain number of vertices by the SPD, with the number of allowable vertices depending on the multiplicity of the event. Approximately 0.3% of the accepted events were rejected with this criterion. The second approach deals only with the second type of pileup and is applied at the track level by requiring the track properties to be of a high quality, for example, requiring matching tracks from the ITS and TPC, restrictions on the distance of closest approach of the track to the reconstructed vertex etc. The specific tracking requirements used in this analysis are covered in Section 4.2.1. The final number of events (N_{ev}) used in this thesis, after event selection and pileup rejection, is listed in Table 4.1.

N_{MB}	$\mathcal{L}_{\mathrm{int}}$	N_{ev}
626×10^6	$299 \pm 11 \ \mu\mathrm{b}^{-1}$	535×10^6

Table 4.1: *The number of MB triggered events (N_{MB}), the integrated luminosity ($\mathcal{L}_{\mathrm{int}}$), and the number of events (N_{ev}) accepted for the analysis after event selection, including pileup rejection.*

---

[1] A bunch is defined as a collection of particles circulating together in the LHC. Typically many, up to 2556 during pp collisions, bunches will be circulating simultaneously in each direction.

The recorded data set is composed of 31 subsets of the data, which correspond to so-called *runs*, where the state of the detector and beams were kept relatively constant for a period of time. Each of these runs is subject to quality assurance (QA) tests performed centrally by the ALICE Data Preparation Group, where fundamental quantities of the detector performance, track matching and calibration are examined. The individual runs are listed in the central Run Condition Table and given a flag based on their perceived quality, along with additional flags corresponding to each detector's performance. All 31 runs were assessed as 'good' and had positive flags for the crucial detectors for this analysis. To ensure that these runs are uniform and can be treated identically, the accepted runs are then further analysed locally focusing on event, track and pair level properties that are important to this analysis. A full list of the track properties used in this analysis can be found in Table 4.2. The local QA calculates the mean and standard deviation of each track property over all runs, and any runs falling outside $\pm 3\sigma$ of the mean would be rejected. An example of this QA check is shown in Fig. 4.1 which plots the average p_T ($\langle p_T \rangle$) of the electron and positron candidates as a function of run number, with all runs being within $\pm 3\sigma$ of the mean. Ultimately, no additional runs were rejected due to these checks.
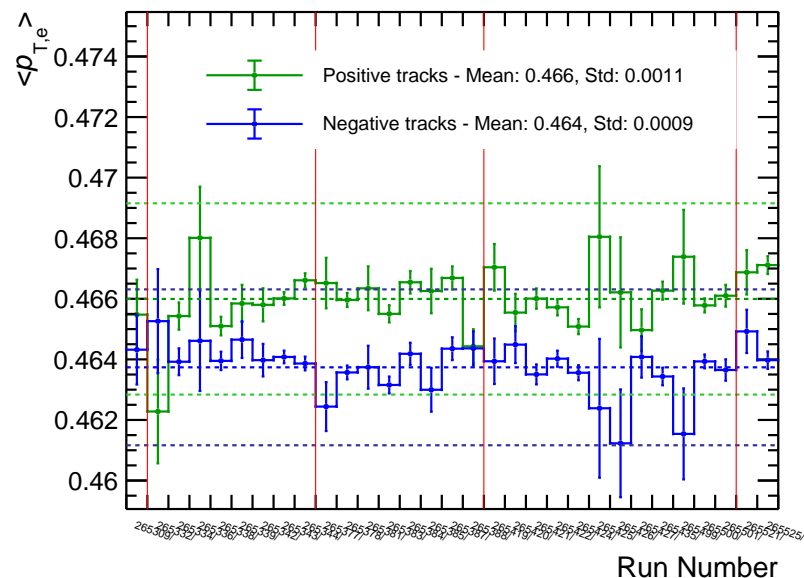
Figure 4.1: *The mean $p_{T,e}$ ($\langle p_{T,e} \rangle$) of the electron (blue) and positron (green) candidates as a function of run number. The dotted horizontal lines represent the mean of the individual runs, and the 3-sigma upper and lower bounds which are used to determine uniformity between the runs. The vertical red lines indicate a new fill of beams from the LHC.*

46

4.2 Track Selection and Electron Identification

4.2.1 Track Selection

The next step after event selection is to ensure that only primary tracks of good quality are accepted. Primary tracks are those originating from the primary collision vertex, whereas secondary tracks can originate from either interactions with the detector material, for example, dielectrons from photon conversions, or from secondary physics processes such as weak decays, which are not relevant for this analysis. The track quality requirements listed in Table 4.2 are applied to achieve this, and only tracks that satisfy each individual requirement are accepted for the analysis.

Feature	Requirement
p_{T}	$0.2 \leq p_{\mathrm{T}} \leq 10\,\mathrm{GeV}/c$
$\lvert\eta\rvert$	≤ 0.8
TPC refit	true
$n^{TPC}_{crossedrows}$	≥ 100
$n^{TPC}_{findableclusters}$	≥ 80
$n^{TPC}_{crossedrows}/n^{TPC}_{findableclusters}$	≥ 0.8
ITS refit	true
SPDfirst	true
$n^{ITS}_{clusters}$	> 2
$n^{ITS}_{sharedclsuters}$	0
$\chi^2/n^{ITS}_{clusters}$	≤ 5.5
Reject kink daughters	true
DCA_{z}	3 cm
DCA_{xy}	1 cm

Table 4.2: *Single track selection criteria applied for this analysis*

The kinematic requirements $0.2 \leq p_{\mathrm{T}} \leq 10\,\mathrm{GeV}/c$ and $\lvert\eta\rvert < 0.8$ are dictated by the detector geometry, the strength of the magnetic field and the momentum resolution. The requirement $\lvert\eta\rvert < 0.8$ defines a region of acceptance covered by both the ITS and TPC that will not result in any edge-type effects, that is, the restriction is slightly smaller than the typically quoted acceptance. The lower bound on the track's p_{T} removes tracks that would suffer from poor reconstruction in the TPC due to the significant bending

of the track by the strong magnetic field. The upper p_T restriction is in place as at higher momenta the track resolution begins to degrade and the PID capabilities become significantly reduced as it becomes no longer possible to separate each particle species from each other. Both the ITS and TPC must have successful refits meaning that during the final refit of the track, the ITS and TPC standalone tracks must be in agreement with the final globally reconstructed track. Specific requirements on the TPC are implemented such as a requiring a minimum number of crossed rows (maximum 159 rows per readout sector), a minimum number of findable TPC clusters (number of crossed rows used for track reconstruction accounting for dead zones), as well as a reasonable ratio between the two. Similar requirements are imposed on the ITS quantities. Each track is required to have a hit in the first layer of the ITS (SPDfirst), which aims to suppress conversions from photons and is covered in detail in Section 4.3.1. Tracks must also not share any ITS clusters with any other tracks (shared ITS hits). As half of the events lacked the information from the SDD (outlined in Section 3.2), and uniformity across the whole data set is desirable, all events were ultimately reconstructed without using the SDD regardless of its availability. For this reason, each track is only required to have minimum number of two ITS hits used during the track fitting process (ITS clusters), as well as a reasonable fit the final track (χ^2 per ITS cluster).
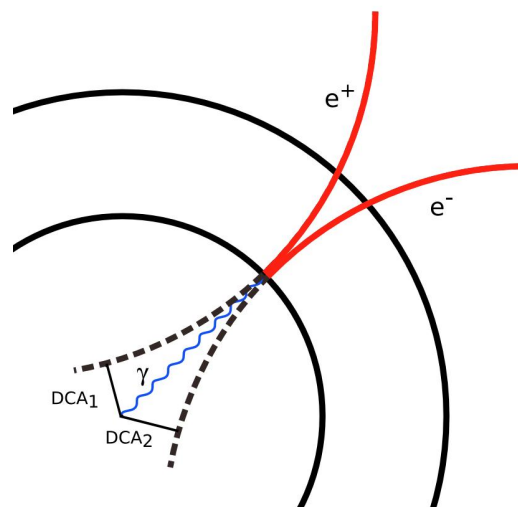
Figure 4.2: *A diagram of the distance-of-closest approach (DCA). Depicted is a photon (blue) converting in the first layer of the detector into a* e^+e^- *pair (red) [112]. The dotted black lines represent the back propagation of the track finding algorithm and highlight how DCA can be useful for separating prompt and non-prompt sources.*

Furthermore, a set of requirements that aim to suppress tracks originating from sec-

ondary decays are applied. Certain weak decays of charged particles, for example, the weak decay $K^{\pm} \rightarrow \mu^{\pm} + \nu$, can leave tracks with very sharp bends in their trajectories with the non-ionizing neutral decay product not being tracked by the detector. Due to the very sharp 'kink' in the curvature, a kink-finder algorithm is used to reject these secondary tracks (Reject kink daughters). Finally, the distance-of-closest approach (DCA) to the primary reconstructed vertex, illustrated in Fig. 4.2, both in the transverse plane (DCA_{xy}) and the longitudinal direction (DCA_z), is restricted. Typically, the DCA requirements for other analyses would be quite strict, however, due to the decay lengths of the c$\bar{\text{c}}$ and b$\bar{\text{b}}$ semi-leptonic decays, $c\tau \sim 150~\mu$m and $c\tau \sim 470~\mu$m, respectively, the restriction on the DCA is relaxed so as to not exclude these dielectron pairs.

4.2.2 Electron Identification

The standard approach to PID within ALICE is to first produce the so-called PID variables ($n(\sigma_i^{\text{Det}})$). These values express the PID response of a given detector (Det) to a track through the number of standard deviations (n) a track is away from the most probable energy deposition for a chosen mass assumption (i) at the particle's momentum (p). Assuming the track is an electron or positron, the TPC PID variable ($n(\sigma_e^{\text{TPC}})$) is calculated with

$$n(\sigma_e^{\text{TPC,raw}}) = \frac{(dE/dx)_{\text{measured}}^{\text{TPC}} - \langle dE/dx \rangle_{\text{e,expected}}^{\text{TPC}}}{\sigma^{\text{TPC}}}, \tag{4.2}$$

where $(dE/dx)_{\text{measured}}^{\text{TPC}}$ is the measured specific energy loss in the TPC, $\langle dE/dx \rangle_{\text{e,expected}}^{\text{TPC}}$ the expected specific energy loss of an electron based on centrally provided splines, which parametrise the Bethe-Bloch curve and are data set specific, and σ^{TPC} the detector resolution, all provided for the given p of the track. The ITS PID variable ($n(\sigma_i^{\text{ITS}})$) would be calculated in the same manner, however, due to the lack of SDD information (covered in Section 4.2.1) the $n(\sigma_i^{\text{ITS}})$ variables were not considered. The TOF PID variable ($n(\sigma_i^{\text{TOF}})$) is calculated analogously using the timing information of the tracks instead of the dE/dx.

The resulting $n(\sigma_i^{\text{Det}})$ distributions should ideally, for all detectors, follow a unit Gaussian. However, due to the sensitivity of electrons and positrons, the $n(\sigma_i^{\text{Det}})$ values require a further calibration step that is performed locally. This step is referred to as *PID post calibration* and aims to ensure that the $n(\sigma_i^{\text{Det}})$ distributions for each detector are unit Gaussians as a function of the particle's p and η. This is performed both on the data and the simulations so that the simulations well reproduce the data. In order to find the

correct calibration values, a pure sample of electrons is needed from both the data and MC simulations. For the data, a so-called V0-finder is employed, described here [113], which only selects electrons originating from photon conversions. These tracks are selected from the data with kinematical selection criteria and by their displaced vertex, whereas for the simulations they can be simply chosen via the MC truth values (pdg codes). The extracted electron sample is fitted with a Gaussian in each p and η bin. The calculated mean (μ) and standard deviation (σ) from each fit is used to recalibrate the existing $n(\sigma_{\mathrm{i}}^{\mathrm{Det,raw}})$ values in each bin with

$$n(\sigma_{\mathrm{i}}^{\mathrm{Det}}) = \frac{n(\sigma_{\mathrm{i}}^{\mathrm{Det,raw}}) - \mu}{\sigma}. \tag{4.3}$$

The obtained PID post calibration maps are shown in Fig. 4.3 and Fig. 4.4 for the TPC and TOF, respectively. The MC $n(\sigma_{\mathrm{i}}^{\mathrm{TPC}})$ distributions do not require this post PID calibration step as this is performed centrally by ALICE. One can see that the largest deviations from a unit Gaussian appear at low p and large η for both the TPC and the TOF detectors. However, and more importantly, one can see that the calibration maps between data and MC for the TOF differ significantly, with the mean of the fits in data being offset by $\sim 0.2\sigma$ over the full range, whereas for the simulations the offset is $\sim 0.3\sigma$ in the opposite direction. In Fig. 4.5, the mean $n(\sigma_{\mathrm{e}}^{\mathrm{TOF}})$ ($<n(\sigma_{\mathrm{e}}^{\mathrm{TOF}})>$) as a function of run number is shown before and after the PID post calibration step. The application of the correction maps ensures that the same PID selection criteria (discussed below) applied to data and MC result in the same electron efficiency, which is crucial for the calculation of final reconstruction efficiency (detailed in section Section 4.4).

(a) Data: mean   (b) Data: width
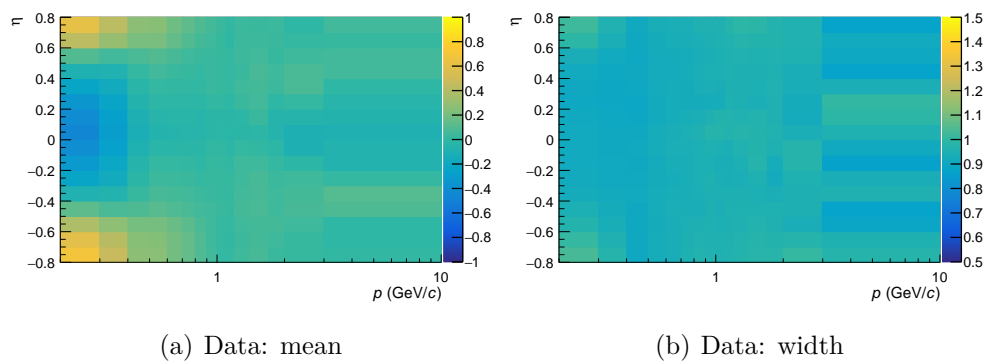
Figure 4.3: *PID post calibration maps for data $n(\sigma_{\mathrm{e}}^{\mathrm{TPC}})$ distributions as a function of p and η. The mean (left) and width (right) of the Gaussian fit in each bin is plotted.*

(a) Data: mean

(b) Data: width

(c) MC: mean

(d) MC: width
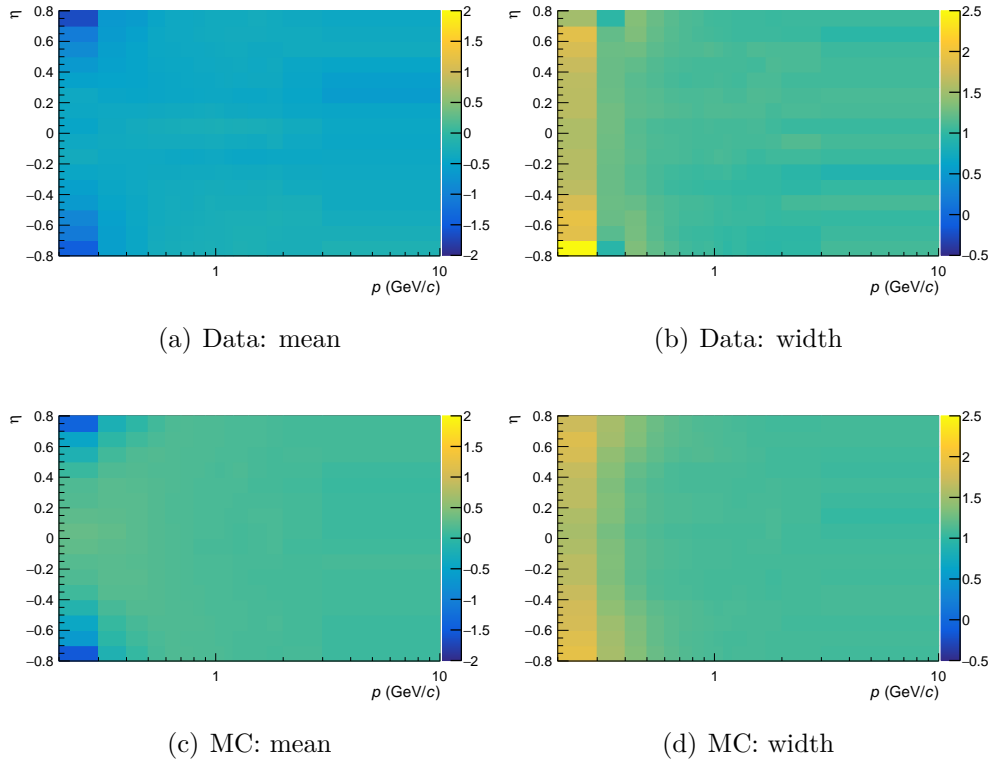
Figure 4.4: *PID post calibration maps for data and MC $n(\sigma_{\mathrm{e}}^{\mathrm{TOF}})$ distributions as a function of p and η. The mean (left) and width (right) of the Gaussian fit in each bin is plotted.*

(a) Before calibration

(b) After calibration
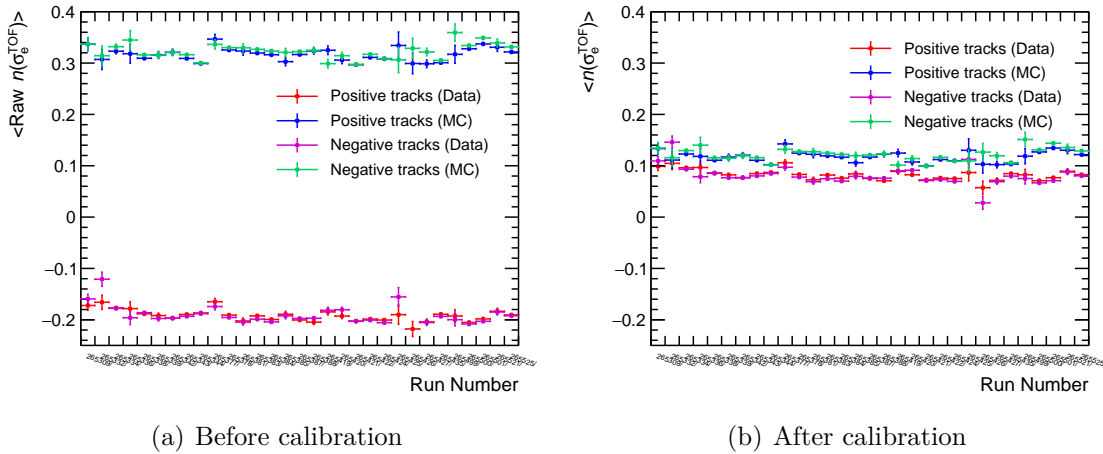
Figure 4.5: *The mean $n(\sigma_{\mathrm{e}}^{\mathrm{TOF}})$ ($\langle n(\sigma_{\mathrm{e}}^{\mathrm{TOF}})\rangle$) as function of run number before (left) and after (right) the PID post calibration step performed on data.*

The electron identification scheme is listed in Table 4.3. The procedure first applies criterion A, which selects electrons over the whole p_T range with the requirement that the track satisfies $-3 < n(\sigma_e^{\mathrm{TPC}}) < 3$, while also applying strong $\pi^\pm$ rejection with the requirement $3.5 < n(\sigma_\pi^{\mathrm{TPC}})$. Next, the track must satisfy either condition B or C. Criterion B rejects potential hadrons by requiring that the track falls outside the $\pm 3\sigma$ range of any of the $\mu^\pm$, $K^\pm$ or $p/\bar{p}$ bands. Criterion C utilises the TOF detector and requires that that track falls within $-3 < n(\sigma_e^{\mathrm{TOF}}) < 3$. A track is accepted as an electron candidate when either A and B or A and C is satisfied. Using this complex PID scheme a high level of hadron rejection is achieved while still maintaining a good detection efficiency (see Section 4.4). The final electron candidates are shown in Fig. 4.6 as a function of $n(\sigma_e^{\mathrm{TPC}})$ and p_T, where faint vertical band structures can be seen for $p_T < 1\,\mathrm{GeV}/c$ and are the result of selection criterion B's rejection of the hadron bands.

While not utilised for the final results in this thesis, considerable work was undertaken investigating the feasibility of using machine learning (ML) to perform PID. While the results were very promising, showing a significant increase in detection efficiency while retaining a low contamination rate, the efficacy of the algorithm decreased without the PID capabilities from the ITS. As approximately half the data set did not contain PID information from the ITS (explained in Section 3.2), the final analysis is performed using the more traditional approach to PID just outlined in this section, so as to utilise the whole data set. For an overview of the ML PID results see the appendix Section 7.4.

Selection	PID requirement
A	$-3 < n(\sigma_e^{\mathrm{TPC}}) < 3$
	$3.5 < n(\sigma_\pi^{\mathrm{TPC}})$
B	$-3 < n(\sigma_\mu^{\mathrm{TPC}}) < 3$
	$-3 < n(\sigma_K^{\mathrm{TPC}}) < 3$
	$-3 < n(\sigma_p^{\mathrm{TPC}}) < 3$
C	$n(\sigma_e^{\mathrm{TOF}}) < 3$

Table 4.3: *Particle identification selection criteria used in this analysis to select a pure sample of electrons and positrons. Each track has to satisfy either A and B **or** A and C in order to be accepted.*
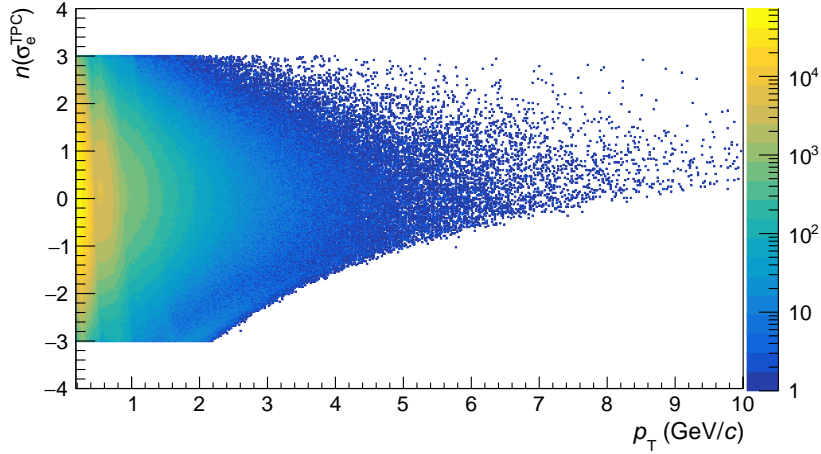
Figure 4.6: *Accepted electron candidates as a function of $n(\sigma_e^{\mathrm{TPC}})$ and p_T after track and PID selection as described in this section.*

4.3 Signal Extraction

After the selection of good quality electron tracks from the data sample, the correlated electron and positron pairs from each event must be paired together. However, as it is not experimentally possible to determine which electron and positron originated from the same decay process, a statistical approach must be taken to extract the di-electron signal. Within each event, every electron is paired with every positron and the invariant mass (m_{ee}) and pair transverse momentum ($p_{T,ee}$) are calculated (outlined in Section 7.2) in order to determine the unlike-sign spectrum ($N_{+-}(m_{ee},\ p_{T,ee})$). Due to the combinatorial pairing procedure, the $N_{+-}(m_{ee},\ p_{T,ee})$ distribution contains not only the true signal pairs ($S(m_{ee},\ p_{T,ee})$), but also unphysical combinatorial e^+e^- pairs, pairs from residual correlations from jets, and so-called cross pairs from two photon decays, for example, $\pi^0 \to \gamma\gamma \to e^+e^-e^+e^-$. In order to extract the signal, these background e^+e^- pairs ($B(m_{ee},\ p_{T,ee})$) are approximated using the same event like-sign distributions ($N_{++}(m_{ee},\ p_{T,ee})$ and $N_{--}(m_{ee},\ p_{T,ee})$). To calculate $B(m_{ee},\ p_{T,ee})$ a hybrid method is employed, whereby the geometric mean is used when both $N_{++}(m_{ee},\ p_{T,ee})$ an $N_{--}(m_{ee},\ p_{T,ee})$ contain at least one pair, and the arithmetic mean is used if one or both are empty. This approach ensures that the background is not underestimated, which can happen if the number of pairs are low and one only uses the geometric mean. In this case, the background will often be estimated as zero and thus the resulting extracted signal will be overestimated. The calculation of $B(m_{ee},\ p_{T,ee})$ is written as

$$B(m_\text{ee},\ p_\text{T,ee}) = \begin{cases} 2\sqrt{N_{++}(m_\text{ee},\ p_\text{T,ee}) \cdot N_{--}(m_\text{ee},\ p_\text{T,ee})}, & \text{if } N_{\pm\pm} > 0 \\[2ex] (N_{++}(m_\text{ee},\ p_\text{T,ee}) + N_{--}(m_\text{ee},\ p_\text{T,ee}))/2, & \text{otherwise.} \end{cases} \tag{4.4}$$

The approach to calculate the background using pairs from within the same event is preferred over using pairs from mixed events (description below), as the same event background also includes the correlated pairs that are contained in the $N_{+-}(m_\text{ee},\ p_\text{T,ee})$. Both the $N_{+-}(m_\text{ee},\ p_\text{T,ee})$ and $B(m_\text{ee},\ p_\text{T,ee})$ are shown on the left in Fig. 4.7 as a function of m_ee. However, as a result of the detector not having full coverage, there is an acceptance asymmetry between the unlike- and like-sign distributions, which must be accounted for before the subtraction. To calculate the acceptance correction factor ($R(m_\text{ee},\ p_\text{T,ee})$), electron and positron tracks from mixed events are paired such that one track is from event i and the second track from event j, given $j \neq i$, with these pairs denoted as $N_{\pm\pm}^{mixed}(m_\text{ee},\ p_\text{T,ee})$ to differentiate them from the same event pairs. To treat the mixed event pairs in the same manner as the same event pairs, only pairs from similar events, meaning a similar reconstructed vertex position as well as multiplicity as listed in Table 4.4, are paired. These mixed event e$^+$e$^-$ pairs do not contain any correlations and only reproduce the detector acceptance effects. The $R(m_\text{ee},\ p_\text{T,ee})$ is calculated as

$$R(m_\text{ee},\ p_\text{T,ee}) = \frac{N_{+-}^{mixed}(m_\text{ee},\ p_\text{T,ee})}{2\sqrt{N_{++}^{mixed}(m_\text{ee},\ p_\text{T,ee}) \cdot N_{--}^{mixed}(m_\text{ee},\ p_\text{T,ee})}}. \tag{4.5}$$

Mixing Bins	z vertex (cm)	Multiplicity (%)
	$\{-10, -7.5, -5, -2.5, 0, 2.5, 5, 7.5, 10\}$	$\{0, 10, 20, 30, 40, 60, 80, 100\}$

Table 4.4: *Binning scheme used for creating mixed-event pairs from similar event types. The mixed-event pairs are used to create the correction acceptance factor ($R(m_\text{ee},\ p_\text{T,ee})$) shown in Eq. 4.5.*

The $R(m_\text{ee},\ p_\text{T,ee})$ as a function of m_ee is shown on the right in Fig. 4.7 where one can see that only low-m_ee pairs ($m_\text{ee} \lesssim 0.3\,\text{GeV}/c^2$) are significantly affected by the correction. For $m_\text{ee} \gtrsim 0.3\,\text{GeV}/c^2$, the correction factor deviates by $\lesssim 0.05\%$ from

unity, and is therefore ignored so as to exclude the statistical fluctuations that arise for higher-m_{ee} pairs ($m_{ee} > 2\,\mathrm{GeV}/c^2$).
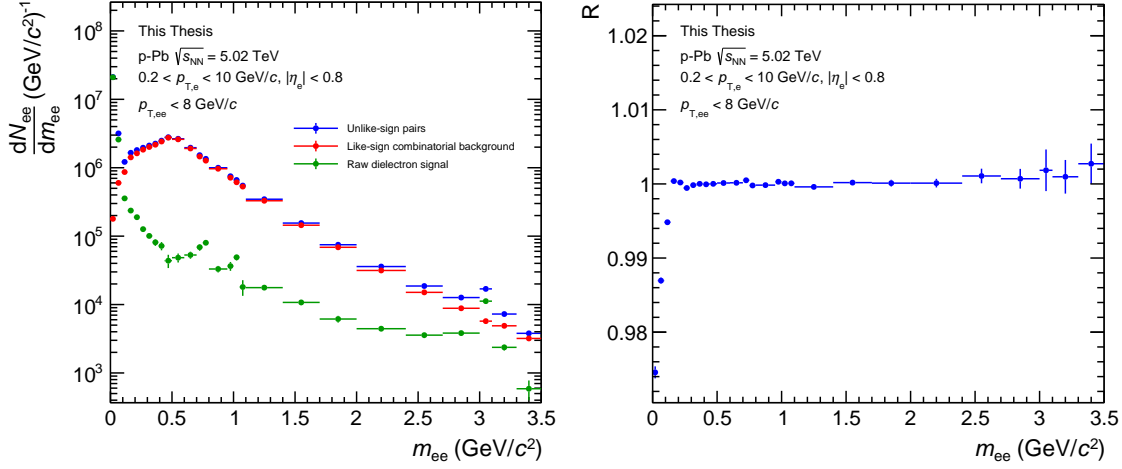
Figure 4.7: *The unlike-sign (blue), combinatorial background (red) and raw yield (green)* e^+e^- *distributions as a function of* m_{ee} *are shown on the left, and the acceptance correction factor* ($R(m_{ee},\ p_{T,ee})$) *as a function of* m_{ee} *is shown on the right.*

The raw dielectron signal is extracted with

$$S(m_{ee},\ p_{T,ee}) = N_{+-}(m_{ee},\ p_{T,ee}) - R(m_{ee},\ p_{T,ee}) \cdot B(m_{ee},\ p_{T,ee}), \tag{4.6}$$

and can be seen as a function of m_{ee} on the left in Fig. 4.7.

The statistical significance of the measurement is quantified by the ratio between the raw signal (written as S in the upcoming equations for simplicity) and the corresponding statistical uncertainty (ΔS)

$$s = \frac{S}{\Delta S}, \tag{4.7}$$

where ΔS is defined as

$$\Delta S = \sqrt{(\Delta N_{+-})^2 + (\Delta B)^2}, \tag{4.8}$$

which results in the statistical significance being calculated as

$$s = \frac{S}{\sqrt{S + 2B}}. \tag{4.9}$$

55

Both the signal-to-background ratio (S/B) and the statistical significance of the measurement are shown as functions of m_{ee} in Fig. 4.8. The S/B has a minimum of nearly 10^{-2} at $m_{\text{ee}} \approx 500$ MeV, and highlights the need for a good understanding of the background, otherwise small over- or underestimations of the background in this region can have large effects on the raw signal determination.
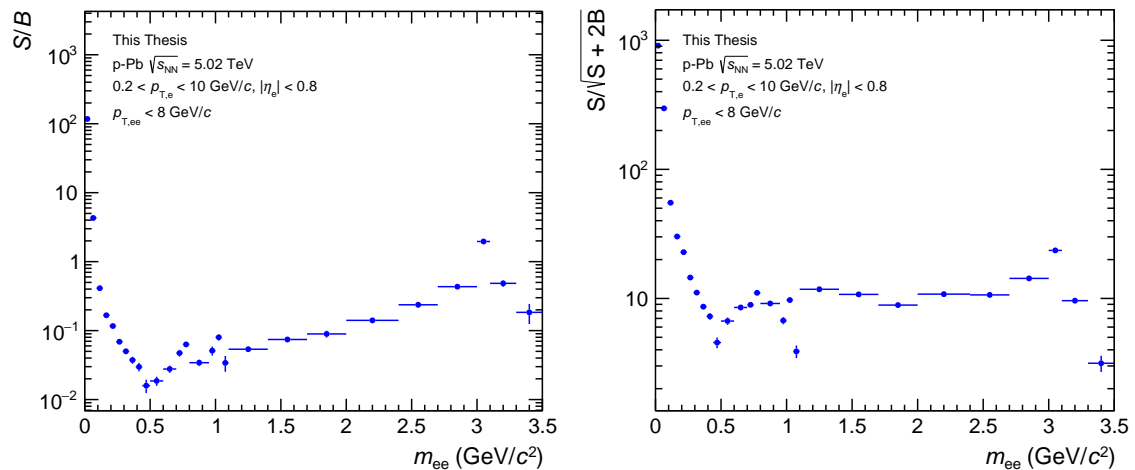
Figure 4.8: *S/B (left) and statistical significance (right) as a function of m_{ee} for the analysed data set.*

4.3.1 Photon Conversion Rejection

Photon conversions in the detector material producing e^+e^- pairs are considered background in this analysis, and need to be removed. To achieve this, three specific criteria are applied, with two being at the single track level, and one at the pair level. While the pair level criterion, which is discussed shortly, is a powerful rejecter of e^+e^- pairs from photon conversions, the track level criteria can significantly improve the statistical significance of the measurement by greatly reducing the combinatorics of the pairing procedure before the signal extraction, thus reducing the denominator in Eq. 4.9.

Each track is required to have both a hit in the first SPD layer, and to not share any hits in any of the ITS layers with other tracks from the same event. The hit in the first layer of the SPD rejects e^+e^- pairs that originate from photons whose late conversions took place beyond the first SPD layer. The restriction on the shared hits in the ITS is motivated by the fact that since photons are massless, the produced e^+e^- pairs have no intrinsic opening angle, and therefore the electron and positron tracks are likely to

share hits in the inner ITS layers as the bending effect due to the magnetic field on the charged tracks will not yet have separated them substantially enough. These two selection criteria increase the S/B by a factor of 2-4 and the statistical significance by $\sim \sqrt{2}$.

Lastly, due to the finite resolution of the detector, e^+e^- pairs from photon conversion are reconstructed with a small but non-zero m_{ee}, which would contaminate the low-m_{ee} portion of the results. In order to avoid such contamination, the fact that the e^+e^- pair has no intrinsic opening angle can again be exploited. As the opening angle between conversion e^+e^- pairs is the result of the magnetic field, it will be preferentially aligned perpendicular to the direction of the magnetic field, whereas for true signal pairs no such directional preference is a-priori expected. Therefore, the so-called φ_V angle is constructed to define the angle between the normal vector of the pair plane and the magnetic field $(\vec{z})$, and is calculated as

$$\vec{u} = \frac{\vec{p}_+ + \vec{p}_-}{|\vec{p}_+ + \vec{p}_-|} \tag{4.10}$$

$$\vec{v} = \vec{p}_+ \times \vec{p}_- \tag{4.11}$$

$$\vec{w} = \vec{u} \times \vec{v} \tag{4.12}$$

$$\vec{u}_a = \frac{\vec{u} \times \vec{z}}{|\vec{u} \times \vec{z}|} \tag{4.13}$$

$$\varphi_V = arccos\left(\frac{\vec{w} \cdot \vec{u}_a}{|\vec{w}||\vec{u}_a|}\right), \tag{4.14}$$

where $\vec{p}_-$ and $\vec{p}_+$ are the momentum vectors of the electron and positron, respectively. On the left in Fig. 4.9, the simulated m_{ee} distribution of the signal pairs is compared to the distribution of e^+e^- pairs originating from photon conversions. The reconstructed m_{ee} from photon conversions are all at very low m_{ee} ($m_{ee} < 0.14\,\mathrm{GeV}/c^2$). On the right in Fig. 4.9, the φ_V distributions are compared between signal and conversion pairs. As one can see, the e^+e^- pairs originating from photons strongly peaks near π with these pairs only starting to significantly contribute from 2 rad onwards. Due to these two characteristics, in this analysis no e^+e^- pairs with $m_{ee} < 0.14\,\mathrm{GeV}/c^2$ and $\varphi_V > 2$ are accepted, with this restriction rejecting close to all e^+e^- pairs from photon conversions, while retaining $\sim 64\%$ of the signal in this region.
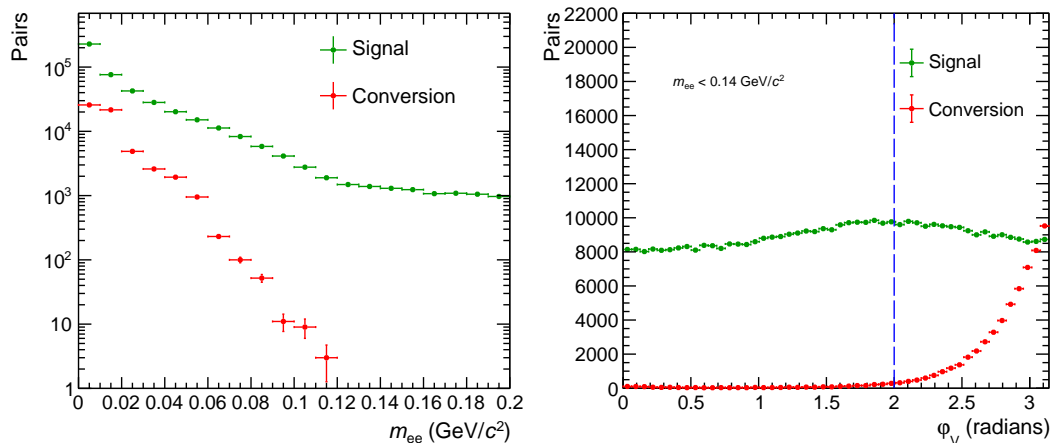
Figure 4.9: *Distribution of signal (green) and conversion (red)* e⁺e⁻ *pairs shown as a function of* m_{ee} *(left) and* φ_V *(right). All single track selection criteria are applied. The vertical blue line represents* φ_V *selection value applied in the analysis.*

4.4 Efficiency Correction

4.4.1 Monte Carlo Simulations

In order to be able to compare an experimental result to theoretical predictions, the efficiency of the measurement must be taken into account. This requires performing the analysis on simulated data, calculating the final efficiency of the selection criteria, and then using this to correct the data. For this analysis, this means accounting for the track reconstruction, the φ_V restriction, and the PID selection efficiencies. To correctly calculate the efficiency correction to the dielectron measurement, a comprehensive MC simulation must be produced, and, equally as important, the specific fluctuations of the data between the different runs must be reproduced. To achieve this, the MC simulations are "anchored" to specific data taking periods, where detector specific settings/states are implemented, for example, dead zones, voltage settings, alignment parameters etc. The simulated events, produced using different event generators based on the underlying physics which will be covered shortly, are propagated through the state of the ALICE detector using GEANT 3 [114,115], and the same reconstruction algorithms used on data are also used to reconstruct the simulated tracks. The primary simulation reproduces the light-flavour dielectron decays (π^0, η', η, ρ^0, ω and ϕ) with a realistic background. Approximately 600 million events were generated with DPMJET-III [116], which is an event generator based on the Dual Parton Model. From the simulations, each event,

58

track, and pair feature that is relevant to this analysis is compared to the data as a function of the run number, and any runs that significantly differ rejected from the analysis. An example of such a comparison is shown in Fig. 4.10, which compares the mean DCA_{xy} ($\langle DCA_{xy} \rangle$) of the positive and negative tracks between data and MC, and highlights the good agreement found between the data and simulations. No runs were rejected on the basis of these checks.
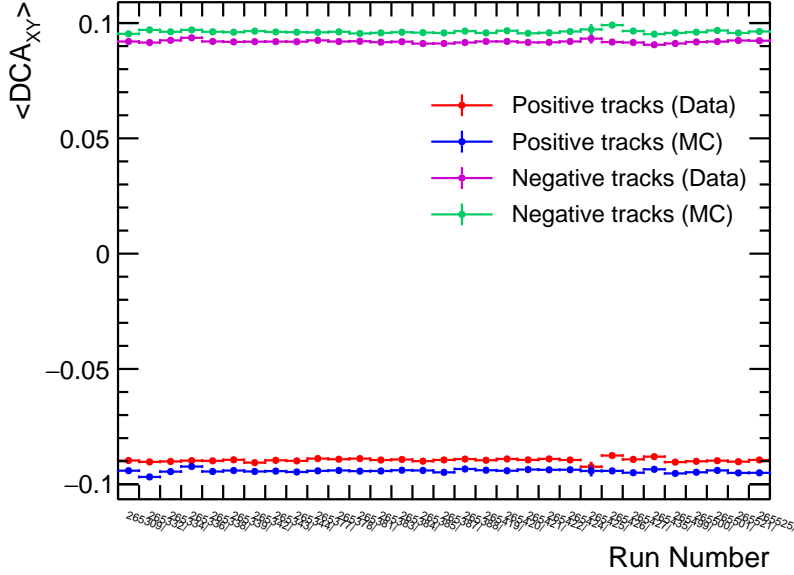
Figure 4.10: *The mean DCA_{xy} ($\langle DCA_{xy} \rangle$) as a function of run number compared between data (positron candidates in red and electron candidates in purple) and simulation (positron candidates in blue and electron candidates in teal). The simulated data in this example were produced with DPMJET-III, propagated through the detector with GEANT 3, and all track and PID criteria outlined in Section 4.2 were applied.*

The kinematic range that is investigated in this analysis is not fully covered by one specific decay type or channel (see Chapter 2), and therefore the DPMJET simulations of the light-flavour decays, which primarily populate the low m_{ee} and $p_{T,ee}$ ranges, are insufficient. In order to achieve full coverage of the measured kinematic region, additional simulations focusing on the heavy-flavour decays in the intermediate mass range ($1.1 < m_{ee} < 2.7\,\mathrm{GeV}/c^2$) are used. For these simulations, the relevant open heavy-flavour decays are generated with PYTHIA 6.4 [117], and are embedded into realistic events simulated with EPOS-LHC [118]. The generated heavy-flavour decays are:

- $c\bar{c} \to e^+e^-$: 5 million events, forced semi-leptonic decays, accepted if both electron/positron tracks are within $|\eta| < 1.2$

- $b\bar{b} \rightarrow e^+e^-$: 5 million events, forced semi-leptonic decays, accepted if both electron/positron tracks are within $|\eta| < 1.2$
- $b, c \rightarrow e$: 40 million events, no forced decays, accepted if one or more electrons or positrons originate from a b decay and are within $|\eta| < 1.2$

4.4.2 Resolution Effects

So as to ensure that the reconstruction efficiency of the measurement is correctly calculated, the relevant detector effects, such as the detector resolution and the radiative energy loss of the particles, must be accounted for. Radiative energy loss occurs when the traversing particle is either deflected by a nearby nucleus, or is bent by the strong magnetic field ($B = 0.5$ T during the recording of the data set used in this thesis). This process is known as Bremsstrahlung, and the radiated power is proportional to m^{-4} when the acceleration is perpendicular to the particles velocity, as is the case for the ALICE detector. Due to the small mass of the electron, as it traverses the detector, it is subjected to significant energy loss which cannot be ignored.

To account for these effects, a discrete folding procedure is applied to the generated tracks in the simulation. To do this, *detector response matrices* are constructed by quantifying the difference between the generated and reconstructed kinematic variables

$$\Delta p = p^{\text{reco.}} - p^{\text{gen.}} \tag{4.15a}$$

$$\Delta \eta = \eta^{\text{reco.}} - \eta^{\text{gen.}} \tag{4.15b}$$

$$\Delta \varphi = \varphi^{\text{reco.}} - \varphi^{\text{gen.}}, \tag{4.15c}$$

where the superscripts "gen." and "reco." indicate generated and reconstructed, respectively, and $\Delta \varphi$ is calculated separately for electrons and positrons due to the opposite direction of bending. The resulting detector response matrices are shown in Fig. 4.11 as a function of $p^{\text{gen.}}$. To apply these matrices for the efficiency correction, every generated particle's kinematic features are smeared by randomly sampling from each relevant distribution at the same $p^{\text{gen.}}$, and shifting the generated value accordingly. This procedure must be applied before the selection criteria when calculating the final reconstruction efficiency correction, otherwise it will significantly overestimate the required correction.

In Fig. 4.12, the ratio between $p^{\text{gen.}}$ and $p^{\text{reco.}}$ for electrons with $0.62 < p^{\text{gen.}} < 0.66$ GeV/c is plotted. One can see the effect of Bremsstrahlung illustrated by the
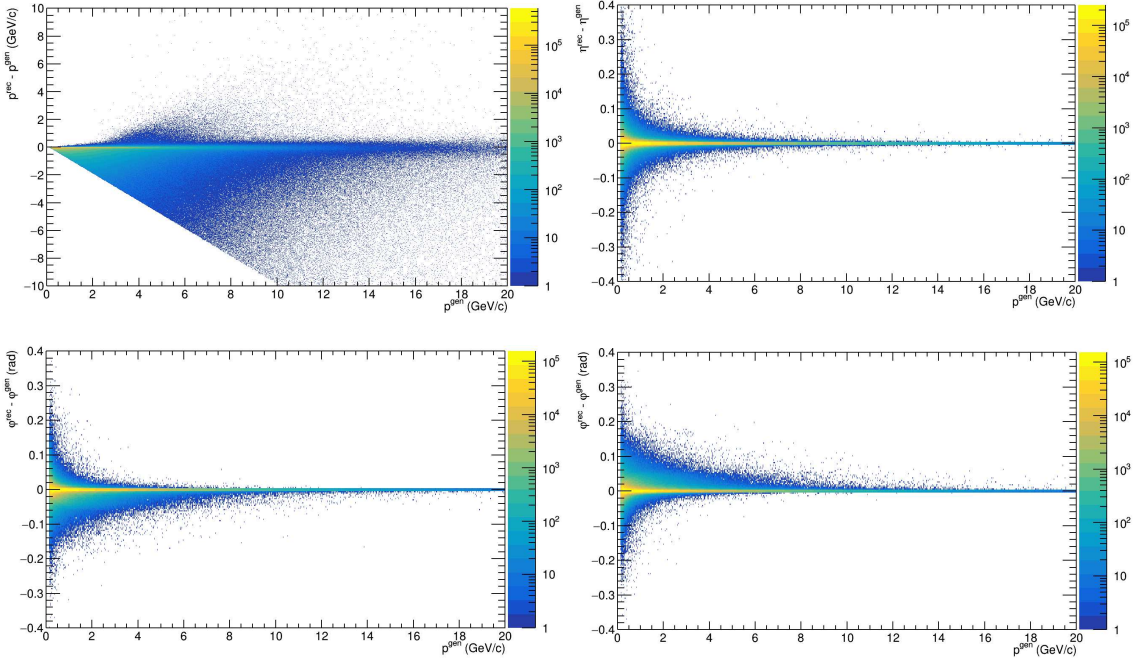
Figure 4.11: *Detector response matrices for p, η and φ obtained by calculating the difference between the generated and reconstructed kinematic variables in the simulated data.*

long tail, while the finite width of the peak is the result of the finite detector resolution.
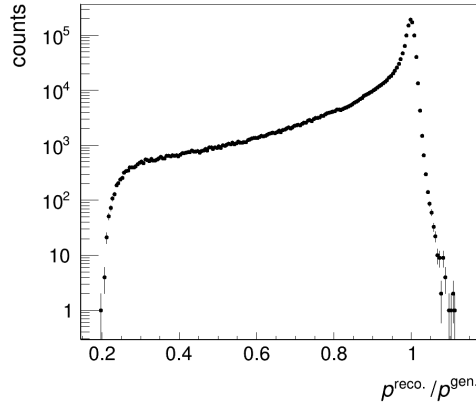
Figure 4.12: *The ratio between the reconstructed and generated momentum ($p^{\text{reco.}}/p^{\text{gen.}}$) for electrons with generated momenta in the range $0.62 < p^{\text{gen.}} < 0.66$ GeV/c.*

4.4.3 Reconstruction Efficiency

The final reconstruction efficiency correction ($\epsilon_{\text{final}}(m_{\text{ee}},\ p_{\text{T,ee}})$) is calculated as the number of reconstructed e$^+$e$^-$ pairs over the number of generated e$^+$e$^-$ pairs after smearing and the application of the kinematic restrictions. This is calculated as

$$\epsilon_{\text{final}}(m_{\text{ee}},\ p_{\text{T,ee}}) = \frac{S^{true}(m_{\text{ee}}^{reco.},\ p_{\text{T,ee}}^{reco.})}{S^{true}(m_{\text{ee}}^{smeared},\ p_{\text{T,ee}}^{smeared})} \tag{4.16a}$$

$$= \epsilon_{\text{LF}}(m_{\text{ee}},\ p_{\text{T,ee}}) \cdot \frac{\mathrm{d}N_{\text{ee}}^{\text{LF}}}{\mathrm{d}N_{\text{ee}}} + \epsilon_{\text{HF}}(m_{\text{ee}},\ p_{\text{T,ee}}) \cdot \frac{\mathrm{d}N_{\text{ee}}^{\text{HF}}}{\mathrm{d}N_{\text{ee}}}, \tag{4.16b}$$

where S^{true} represents the number of "true" signal e$^+$e$^-$ pairs selected via their pdg codes, ϵ_X represents the efficiency for light-flavour (LF) or heavy-flavour (HF) e$^+$e$^-$ pairs, and $\frac{\mathrm{d}N_{\text{ee}}^{\text{X}}}{\mathrm{d}N_{\text{ee}}}$ the relative fraction of light-flavour or heavy-flavour e$^+$e$^-$ pairs as determined from the hadronic cocktail (covered in Section 4.6). The pair reconstruction efficiencies for the track and PID selection criteria, and the φ_V requirement, are presented in Fig. 4.13.
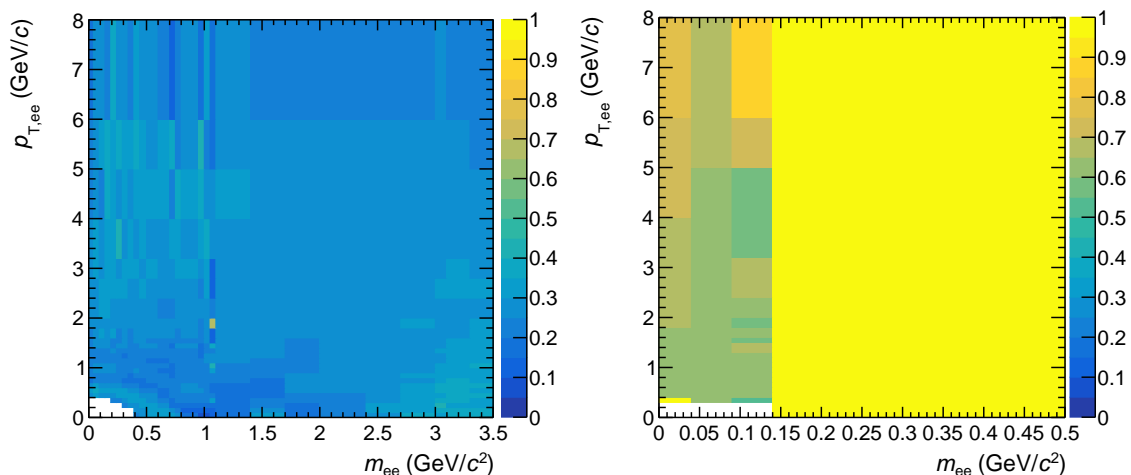
Figure 4.13: *Pair efficiencies for track and PID criteria (left), and for the φ_V requirement (right), as a function of m_{ee} and $p_{\text{T,ee}}$. The track and PID selection efficiency is determined via a weighted sum of light-flavour and heavy-flavour efficiencies. The φ_V selection efficiency is determined using only the DPMJET MC. The final reconstruction efficiency is the product of the two.*

The selection efficiency due to the track and PID criteria is approximately 30% over the entire range, with only small fluctuations in the radial direction at $m_{\text{ee}} \approx 600$ MeV

due the PID hadron band rejection technique. The φ_V selection efficiency is $\sim 64\%$ (detailed in Section 4.3.1), and is 100% for $m_{\mathrm{ee}} > 0.14\,\mathrm{GeV}/c^2$ by construction. The MB trigger and vertex reconstruction efficiency were investigated, and found to be consistent with unity. The final corrected dielectron yield is shown in Fig. 4.14 as projections onto m_{ee} and $p_{\mathrm{T,ee}}$. The corrected $\mathrm{e^+e^-}$ spectrum is compared the hadronic cocktail, along with additional models, in Chapter 5.
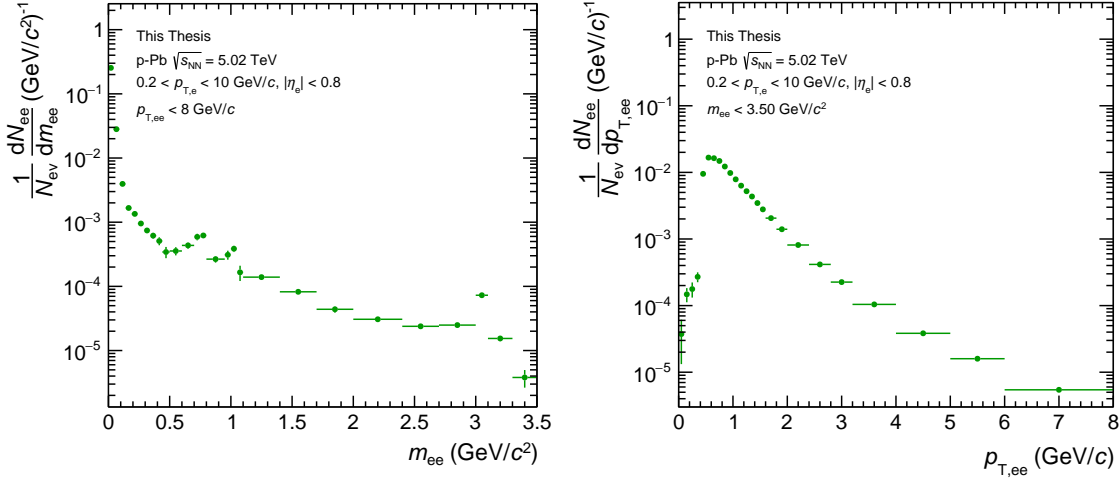
Figure 4.14: *The corrected dielectron yield measured at midrapidity in p–Pb collisions at $\sqrt{s_{\mathrm{NN}}} = 5.02$ TeV shown as a function of m_{ee} (left) and $p_{\mathrm{T,ee}}$ (right) normalised to the number of analysed events.*

4.5 Systematic Uncertainties

Ultimately, two sources of systematic uncertainties are considered. The uncertainties associated to the calculations of the expected dielectron production, which are covered in Section 4.6.4, and the uncertainties associated with the analysis of the data, which are covered in this section.

At each step during the analysis of the data, cross checks are performed to determine if the intrinsic uncertainty associated with each analysis step is significant, and if so, what is its contribution to the final total systematic uncertainty of the measurement. To suppress any statistical fluctuations being recorded as uncertainties, all cross checks are calculated in course m_{ee} and $p_{\mathrm{T,ee}}$ bins.

To calculate the uncertainties of the requirement of a hit in the first layer of the ITS (SPDfirst), as well the ITS-TPC matching efficiency, a toy-MC method is used.

An example of the process is shown in Fig. 4.15 and will now be outlined. First, the single track uncertainties are obtained by calculating the relative difference in selection efficiency for a given selection criteria between data and MC simulations as a function of p_T (top left). These uncertainties are then fed into a toy MC simulation, which populate the entire measured phase space in m_{ee} and $p_{T,ee}$ with particles which are then forced to decay into an e^+e^- pair, with the resulting uncertainty being the sum of each decay particle's uncertainty evaluated at each individual p_T (top right). Finally, the uncertainties in m_{ee} and $p_{T,ee}$ are weighted with a realistic spectrum determined from the expected dielectron $p_{T,ee}$ spectrum (see next chapter for calculation details), before being projected into ranges corresponding to the analysis (bottom panels). The uncertainties on both the SPDfirst requirement and the ITS-TPC matching efficiency are found to be ~2% with such a small m_{ee} or $p_{T,ee}$ dependence relative to the total systematic uncertainty that it is neglected.

The uncertainty of the $R(m_{ee}, p_{T,ee})$ is checked by varying the bins in which the mixed event pairs are created in. The mixed event binning scheme is presented in Table 4.5, with the resultant acceptance correction factors for the different mixing schemes shown for the low-m_{ee} region on the left in Fig. 4.16. No significant deviation is found.

Scheme	z vertex (cm)	Multiplicity (%)
1	$\{-10, -7.5, -5, -2.5, 0, 2.5, 5, 7.5, 10\}$	$\{0, 5, 10, 20, 30, 40, 60, 80, 100\}$
2	$\{-10, -5, 0, 5, 10\}$	$\{0, 5, 10, 20, 30, 40, 60, 80, 100\}$
3	$\{-10, -5, 0, 5, 10\}$	$\{0, 10, 20, 30, 40, 60, 80, 100\}$
4	$\{-10, 0, 10\}$	$\{0, 5, 10, 20, 30, 40, 60, 80, 100\}$
5	$\{-10, -7.5, -5, -2.5, 0, 2.5, 5, 7.5, 10\}$	$\{0, 20, 30, 40, 60, 80, 100\}$

Table 4.5: *Different binning schemes used to asses if any uncertainty should be associated with the acceptance correction factor used to correct the background calculation before signal extraction.*

The uncertainty of the efficiency correction method itself is investigated by comparing corrected dielectron spectra which had only used either light-flavour or heavy-flavour e^+e^- pairs for the correction. Given sufficiently relaxed restrictions on the DCA criteria, one would a priori expect these to return the same correction factor, however as shown on the right in Fig. 4.16, a very small difference between the two corrected spectra is observed, and as a result a 3% uncertainty on the efficiency correction is applied with no m_{ee} or $p_{T,ee}$ dependence.
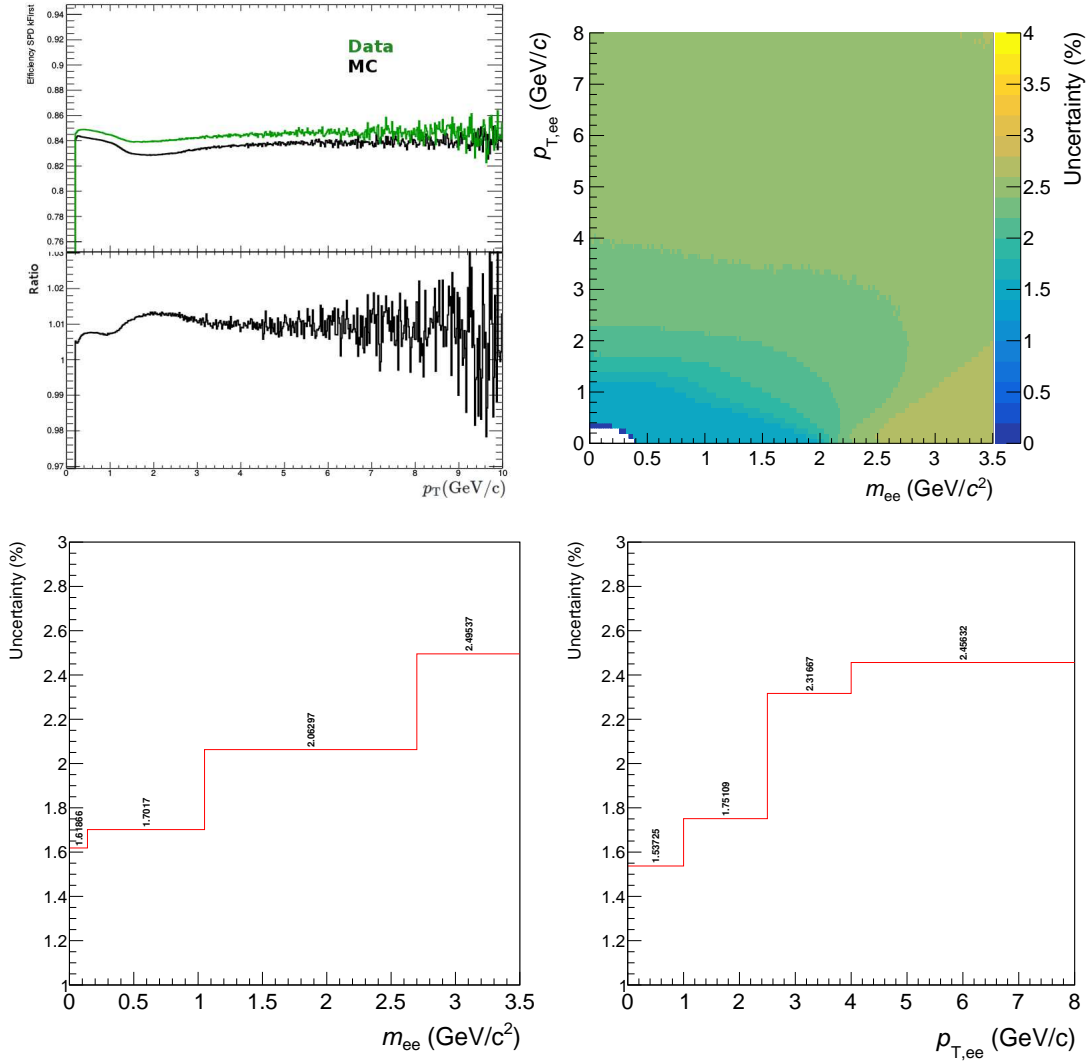
Figure 4.15: *Determining the systematic uncertainty associated with the requirement that each track have a hit in the first layer of the ITS (SPDfirst). Top left: single track SPDfirst selection efficiencies compared between data (green) and MC simulations (black) with the ratio of the two shown below. Top right: resulting uncertainties (%) propagated to m_{ee} and $p_{T,ee}$ via a toy-MC simulation. Bottom row: uncertainties projected onto the m_{ee} and $p_{T,ee}$ axes.*

The φ_V selection criteria is also investigated by varying the selection requirement around the nominal value from 1.5 to 2.7 rad, as well as comparing the selection efficiency between data and MC, as shown on the left in Fig. 4.17. A small discrepancy of $\sim2\%$ is observed. As the φ_V selection is only applied for $m_{ee} < 0.1\,\mathrm{GeV}/c^2$, the uncertainty from this criterion is not applicable for the higher mass pairs.
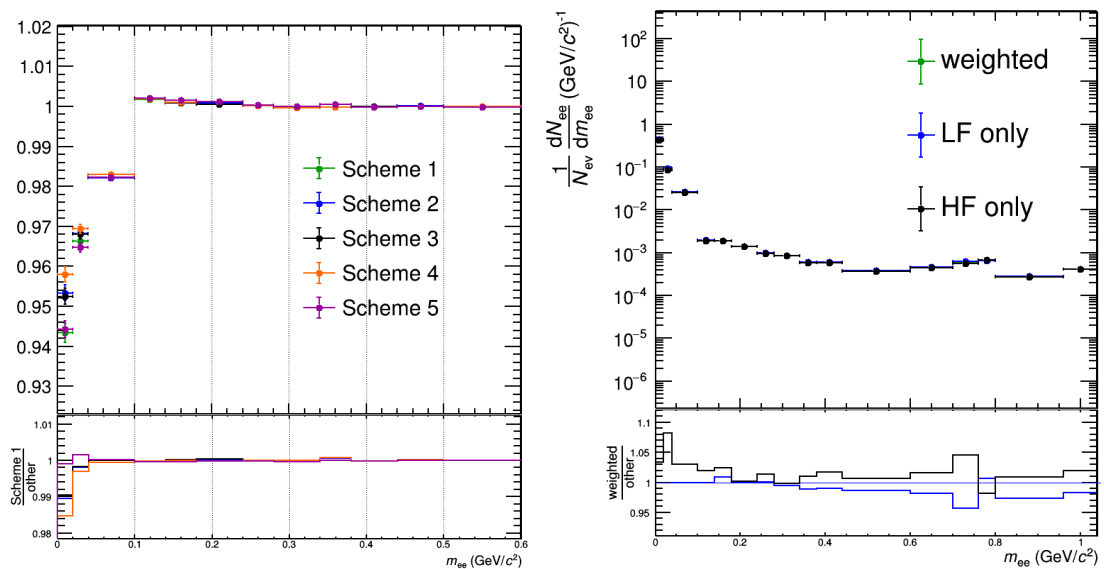
Figure 4.16: *Left: The correction acceptance factors calculated for different mixing bins as listed in Table 4.5. Right: efficiency corrected dielectron yields using only light-flavour (LF) or only heavy-flavour (HF) compared to the central value determined with the weighted method outlined in Section 4.4.3.*

The uncertainty from the requirement that no tracks shared hits in the ITS layers is calculated by loosening the criteria to allow up to four shared layers with another track (the maximum allowable) and comparing the resulting corrected spectra. This cross check also provided a test on the understanding of the background, as the S/B is varied by a factor of two when no restriction is applied. A small uncertainty of 2% for $m_{ee} < 1.1\,\mathrm{GeV}/c^2$ is observed as shown on the right in Fig. 4.17, with a slight $p_{\mathrm{T,ee}}$ dependence that is also accounted for.

The uncertainty arising from the tracking and PID selection criteria, listed in Table 4.2 and Table 4.3, respectively, are calculated by simultaneously varying the selection criteria 20 times (listed in Tables 7.2 and 7.3), and comparing the resulting spectra for any significant differences. The results from these criteria variations are presented in Fig. 4.18 in course m_{ee} bins. Both the mean of the yields as well as the mean weighted by the statistical uncertainty are shown on the plots and are in very close agreement with each
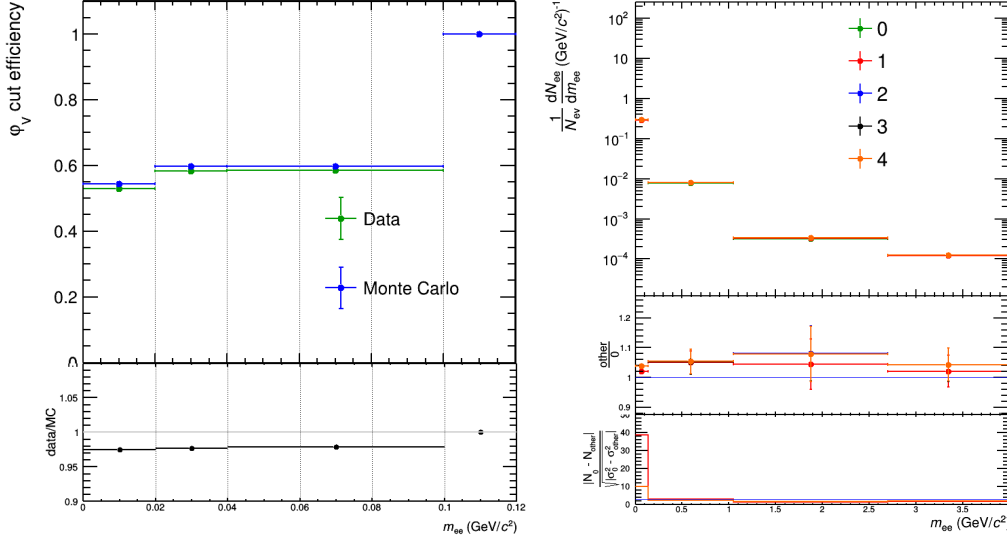
Figure 4.17: *Left: φ_V selection criteria efficiency compared between data (green) and MC simulations (blue) using DPMJet-III. Right: Corrected dielectron yields with differing number of shared hits in the ITS (indicated in by the legend) compared, with the resulting ratio and significance tests plotted below. The blue line the lowest ratio plot indicates the 3σ significance level.*

other. In addition, the PID scheme itself is investigated by comparing the resulting spectra when using the current PID selection criteria against the PID scheme used in a previous ALICE dielectron paper which analysed pp collisions at $\sqrt{s} = 7$ TeV [84]. These two uncertainties are added in quadrature. In the very low-m_{ee} region ($0 < m_{ee} < 0.14\,\mathrm{GeV}/c^2$), the uncertainty is found to be 10%, whereas for higher m_{ee} the associated uncertainty is found to be much lower at 2%.

While the hadron contamination is implicitly probed in the previous cross checks, it is also explicitly investigated with a MC analysis. Via this method, the level of contamination is known and could be tracked from the single track level to the final result after the background subtraction. Such a check is performed for all 20 PID selection settings. The resulting contamination is found to be $< 0.3\%$, and therefore is not considered for the final uncertainty calculation. The final uncertainty is calculated as the quadratic sum of all individual sources and is presented in course m_{ee} bins in Table 4.6.
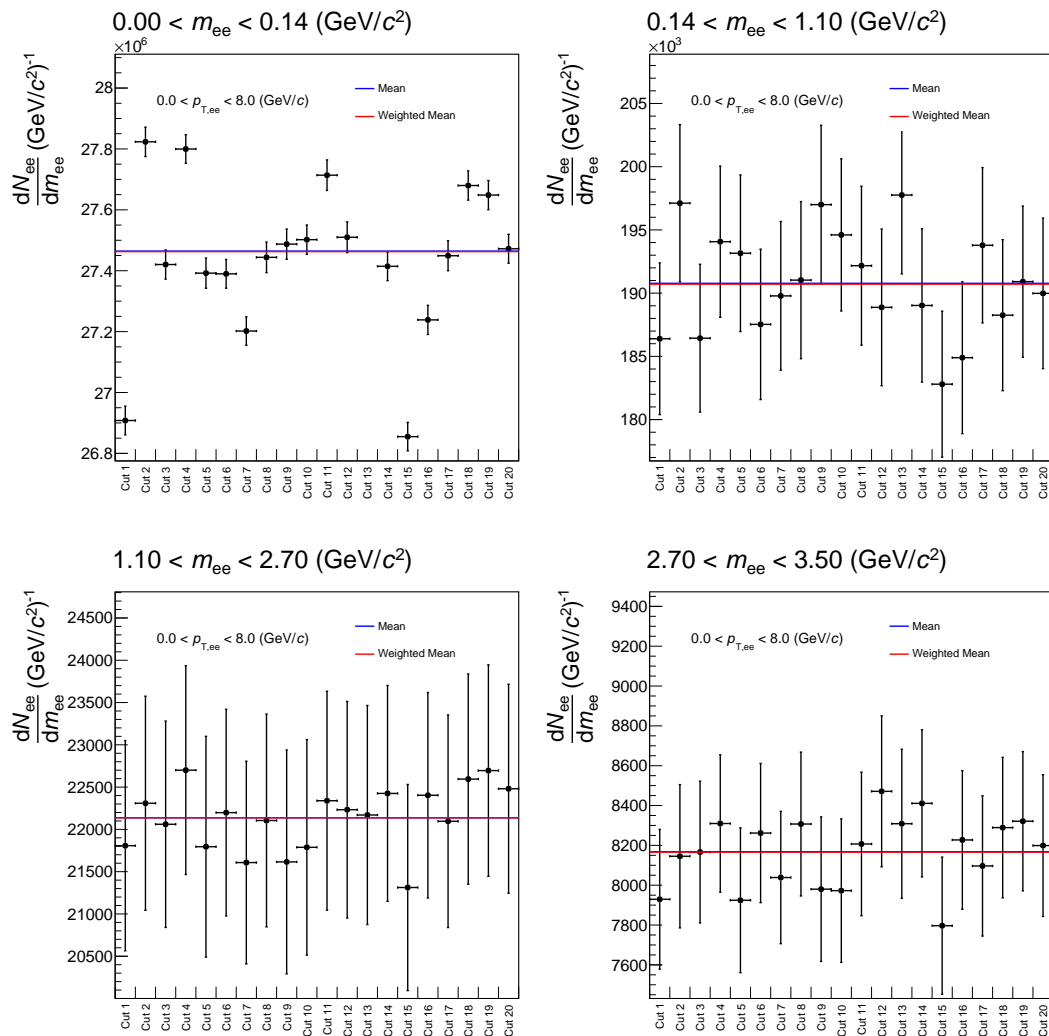
Figure 4.18: *Dielectron yields in course m_{ee} bins integrated over $0 < p_{T,ee} < 8 \, \mathrm{GeV}/c$ for the 20 different track and PID selection criteria listed in Tables 7.2 and 7.3. The mean of the yields is shown in blue and the mean weighted by the statistical uncertainty of each yield is shown in red.*

m_{ee} (GeV/c^2)	SPDfirst	ITS-TPC	Shared ITS	φ_V	Track & PID	Total
< 0.14	2 %	2 %	2 %	2 %	10 %	11 %
$0.14 - 1.1$	2 %	2 %	2 %	–	2 %	5 %
$1.1 - 2.7$	2 %	2 %	0 %	–	2 %	5 %
$2.7 - 3.5$	2 %	2 %	0 %	–	2 %	5 %

Table 4.6: *Systematic uncertainties of the requirement of a hit in the first ITS layer (SPDfirst), the ITS-TPC matching efficiency (ITS-TPC), the allowed number of shared clusters in the ITS (shared ITS), the variation of the φ_V selection, and the tracking and PID variations (Track & PID) in coarse m_{ee} intervals. The uncertainty of the light- and heavy-flavour efficiency differences of 3% is not listed, but is applied over the whole range of the measurement and included in the total uncertainty. The total systematic uncertainty is the quadratic sum of the single contributions assuming they are all uncorrelated.*

4.6 Hadronic Cocktail

This section details the process of generating the hadronic cocktail, which is a data driven simulation of all significant and known hadronic decays resulting in a e^+e^- pair. An example of such a calculation as a function of m_{ee} (left) and $p_{T,ee}$ (right) is shown in Fig. 4.19 after the application of the fiducial requirements on the single tracks ($0.2 \leq p_T \leq 10 \, \text{GeV}/c$ and $|\eta| < 0.8$). The simulation of the light-flavour hadron decays (π^0, η, η', ρ^0, ω and ϕ) is covered in Section 4.6.1, the open heavy-flavour contributions ($c\bar{c}$ and $b\bar{b}$) calculated using two separate event generators PYTHIA 6.4 and POWHEG are detailed in Section 4.6.2, and the generation of the J/ψ contribution is outlined in Section 4.6.3. For all contributions, a fast MC simulation is used whereby the generated particles are smeared with the resolution matrices outlined in Section 4.4.2, and then the fiducial selection criteria applied. The systematic uncertainties of the hadronic cocktail are presented in Section 4.6.4.

4.6.1 Light-Flavour

The simulated light-flavour hadron decays are listed in Table 4.7 along with their branching ratios and method used to generate their p_T spectra. The contributions to the dielectron yield are simulated using the phenomenological event generator EXODUS [119]. The Dalitz decays are generated according to the Kroll-Wada equation [120]
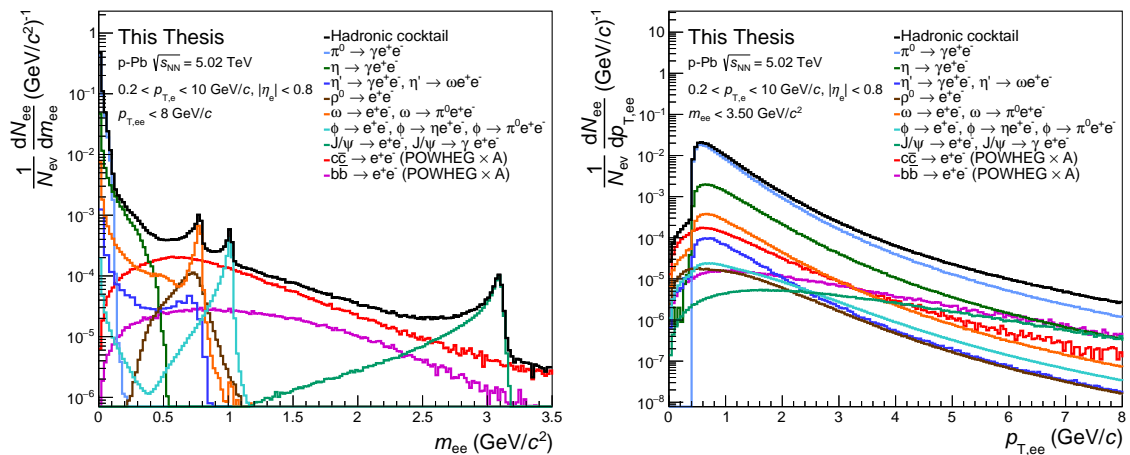
Figure 4.19: *The expected dielectron yield per event in p–Pb collisions at $\sqrt{s_{NN}} = 5.02$ TeV assuming simple atomic mass scaling (A = 208) of the heavy-flavour contributions, generated with POWHEG, presented as a function of m_{ee} (left) and $p_{T,ee}$ (right).*

$$\frac{\mathrm{d}^2N}{\mathrm{d}m_{ee}\mathrm{d}p_{T,ee}} = \frac{2\alpha_{EM}}{3\pi}\sqrt{1 - \frac{3m_e^2}{m_{ee}^2}}\left(1 + \frac{2m_e^2}{m_{ee}^2}\right)\frac{1}{m_{ee}}S(m_{ee},\ p_{T,ee})\frac{\mathrm{d}N_h}{\mathrm{d}p_T}, \qquad (4.17)$$

where α_{EM} is the electromagnetic fine structure constant ($\alpha_{EM} \approx 1/137$), $S(m_{ee},\ p_{T,ee})$ the electromagnetic form factor, and $\frac{\mathrm{d}N_h}{\mathrm{d}p_T}$ the measured yield of the hadron as a function of p_T. The form factors, as well as the ρ^0 line shape, that are used in this thesis were measured by the NA60 Collaboration [121,122]. The two-body decays of ω and ϕ are simulated using the Gounaris-Sakurai formula [123].

The left plot in Fig. 4.20 compares the available π^0 and $\pi^\pm$ p_T spectra from p–Pb collisions at $\sqrt{s_{NN}} = 5.02$ TeV in the multiplicity[2] range 60 - 80% [124,125][3]. The $\pi^\pm$ p_T measurement extends down to far lower p_T ($p_T \approx 100$ MeV) than the π^0 p_T measurement ($p_T \approx 400$ MeV). In order to ensure that the fit is constrained at low p_T, which is particularly important for this analysis, the $\pi^\pm$ p_T spectrum is taken as a proxy for the π^0. The fit is performed with a modified Hagedorn function [126] defined as

$$\frac{\mathrm{d}^2N}{\mathrm{d}y\mathrm{d}p_T} = p_T \cdot A \cdot \left(exp(B \cdot p_T + C \cdot p_T^2) + \frac{p_T}{D}\right)^{-E}, \qquad (4.18)$$

---

[2]As the geometric interpretation applied in AA collisions is not well-defined for pp and pA collisions, multiplicity percentiles are used instead.

[3]Measured p_T spectra of $\pi^\pm$ and ϕ production in p–Pb collisions at $\sqrt{s_{NN}} = 5.02$ TeV were only available in multiplicity classes at the time of this thesis.

Particle	Simulated decays	Branching ratio (%)	Calculated with
π^0	γe^+e^-	(1.17 ± 0.04)	fit($\pi^\pm$) (data)
η	γe^+e^-	$(6.90 \pm 0.40) \cdot 10^{-3}$	fit(η/π^0) (data)
η'	γe^+e^-	$< 9 \cdot 10^{-4}$	m_T scaling
	ωe^+e^-	$(2.00 \pm 0.40) \cdot 10^{-5}$	
ρ^0	e^+e^-	$(4.72 \pm 0.05) \cdot 10^{-4}$	fit(ρ^0/π^0) (PYTHIA 8.1)
ω	e^+e^-	$(7.28 \pm 0.14) \cdot 10^{-5}$	fit(ω/π^0) (PYTHIA 8.1)
	$\pi^0 \, e^+e^-$	$(7.70 \pm 0.60) \cdot 10^{-4}$	
ϕ	e^+e^-	$(2.95 \pm 0.03) \cdot 10^{-4}$	fit(ϕ) (data)
	$\eta \, e^+e^-$	$(1.15 \pm 0.10) \cdot 10^{-4}$	
	$\pi^0 \, e^+e^-$	$(1.12 \pm 0.28) \cdot 10^{-5}$	

Table 4.7: *Simulated light-flavour hadron decays calculated for the expected dielectron yield in p–Pb collisions at $\sqrt{s_\mathrm{NN}} = 5.02$ TeV. Also listed are the branching ratios along with the associated uncertainty, and the method used to generate the input p_T spectrum for the simulations.*

where A, B, C, D and E are the fit parameters. An example of a fit to the $\pi^\pm$ p_T spectrum, performed in the multiplicity range 60 - 80 %, is shown on the left in Fig. 4.22. The ratio shows good agreement between the data and the fit, with the shown uncertainties being the statistical and systematic uncertainties of the data added in quadrature. However, while the constraint at low p_T motivates the use of the $\pi^\pm$ p_T spectrum, small differences between the π^0 and $\pi^\pm$ p_T spectra are still expected due to isospin-violating decays, in particular from the η meson [127]. To account for this, a p_T-dependent scaling factor is calculated using an effective model which is able to describe hadron spectra at low p_T, and includes both strong and electromagnetic decays [128]. The final $\pi^\pm$ scaling factor, along with the fit function, is shown on the right in Fig. 4.20. The dashed vertical blue line is drawn at $p_\mathrm{T,ee} = 400$ MeV to represent the radius of the acceptance hole due to the kinematic restrictions, and highlights why the scaling factor has only a small effect ($\approx 2\%$) in the very low-m_ee region, and is negligible once the contributions from the open heavy-flavour decays, primarily $c\bar{c}$, become significant. The upper and lower fits in the plot will be covered in Section 4.6.4.

Measured p_T spectra for η, η', ω and ρ^0 in p–Pb collisions at $\sqrt{s_\mathrm{NN}} = 5.02$ TeV were not available during the time of this thesis. To construct the η p_T spectrum, a wide range of experimental measurements of η/π^0 are used to determine a ratio that is well constrained down to low p_T. The low energy points were measured by the HELIOS
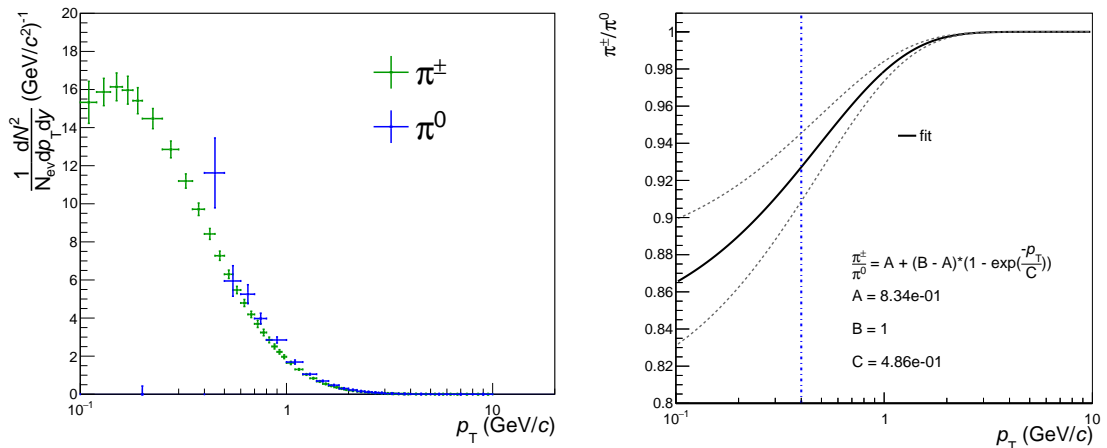
Figure 4.20: *Left: π^0 (blue) and $\pi^\pm$ (green) p_T spectra in p–Pb collisions at $\sqrt{s_{NN}} = 5.02$ TeV measured with ALICE [124, 125]. The $\pi^\pm$ is used as an input for the dielectron cocktail generation as it is constrained down to much lower p_T than the π^0 p_T spectrum. Right: Ratio used to weight the $\pi^\pm$ p_T spectrum to account for isospin-violating decays.*

and CERES/TAPS collaborations and were recorded in p–Au and p–Be collisions at $\sqrt{s_{NN}} = 29.1$ GeV [129], whereas the high energy data points were recorded by the ALICE collaboration in pp and p–Pb collisions at $\sqrt{s} = 7$ and 8 TeV and $\sqrt{s_{NN}} = 5.02$ TeV [124, 130, 131], respectively. The procedure to parametrise η/π^0 ratio is covered in detail in [132] with the final fit shown in Fig. 4.21. In the region where the different measurements overlap ($0.4 \leq p_T \leq 1.5$ GeV/c), the data are in good agreement within uncertainties, and seem to validate the assumption that at the current precision the light-flavour ratios can be treated as energy independent.

The input p_T spectra for the ω and ρ^0 simulations are generated by calculating the $\omega/\pi^\pm$ and $\rho^0/\pi^\pm$ ratios in pp collisions at $\sqrt{s} = 5.02$ TeV generated using PYTHIA 8.1 [133]. A different collision system for the ratio calculations is used so that the systematic uncertainties on the simulated nuclear modification factors (presented in Section 5.3) from these decays would be fully correlated and therefore cancel each other out.

The η' input p_T spectrum is calculated assuming the validity of m_T scaling [134–136], which states that the p_T shape of the light mesons is the same and only differs by a scaling factor when expressed as a function of the particle's transverse mass (m_T), where $m_T = \sqrt{m_0^2 + p_T^2}$ with m_0 representing the pole mass of the meson. The m_T scaling factor for η' is determined using PYTHIA 8.1 and found to be 0.40±0.08.

Finally, the ϕ input p_T spectrum is determined directly from fits to an ALICE measurement recorded in p–Pb collisions at $\sqrt{s_{NN}} = 5.02$ TeV [137]. The ϕ p_T fits were performed using a modified Hagedorn function (see Eq. 4.18), and an example of a fit in the multiplicity class 0–5 % is shown on the right in Fig. 4.22, where good agreement between the data and fit are observed.

The final light-flavour hadronic cocktail as function of m_{ee} is presented in Fig. 4.23, with the generated distribution shown on the left, and the reconstructed result after fiducial selection criteria on the right.
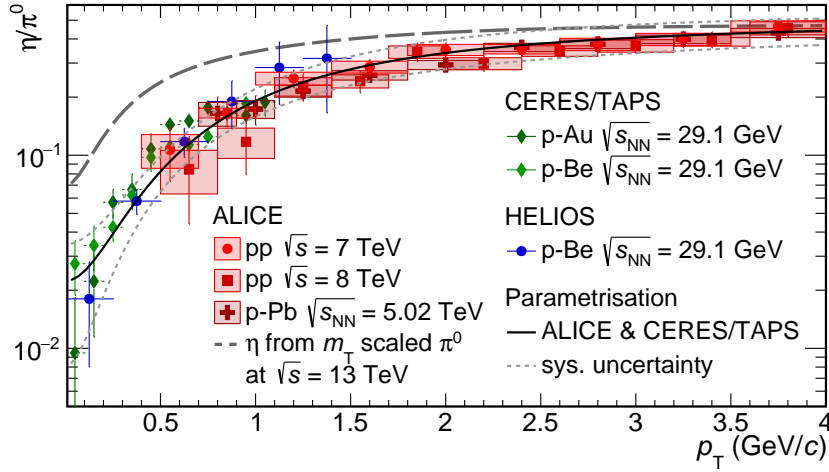
Figure 4.21: *The η/π^0 p_T ratio constructed from multiple measurements in different collision systems at varying energies [132]. The low-energy data points are from the HELIOS and CERES/TAPS collaborations recorded in p–Au and p–Be collisions at $\sqrt{s_{NN}} = 29.1$ GeV [129]. The high-energy data points are from pp and p–Pb collisions recorded with ALICE at $\sqrt{s} = 7$ and 8 TeV and $\sqrt{s_{NN}} = 5.02$ TeV [124, 130, 131], respectively.*

4.6.2 Open Heavy-Flavour

The contributions to the hadronic cocktail from the semi-leptonic open heavy-flavour decays, namely from open charm and open beauty hadrons as outlined in Section 2.2, are calculated with two different MC event generators.

PYTHIA 6.4 [117] is a leading-order (LO) event generator and includes next-to-leading-order (NLO) parton shower processes. The framework uses the phenomenological Lund string model for the fragmentation and hadronisation processes of the charm and beauty quarks, and the parameters were tuned according to the Perugia2011 tune [138] and used the CTEQ5L [139] PDF.

(a) $\pi^{\pm}$

(b) ϕ
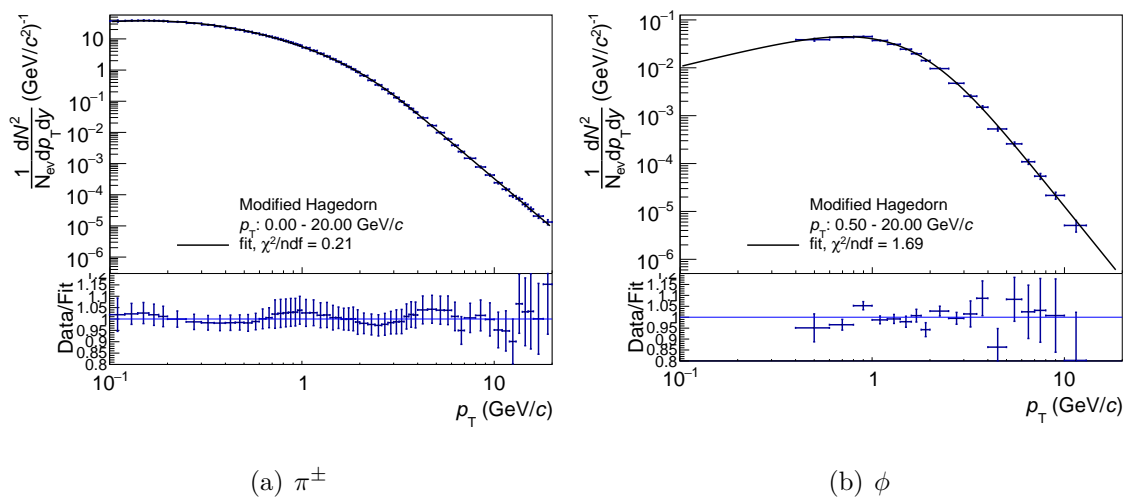
Figure 4.22: *$\pi^{\pm}$ (left) and ϕ (right) p_{T} spectra measured in p–Pb collisions at $\sqrt{s_{\mathrm{NN}}} = 5.02$ TeV by the ALICE collaboration [125, 137]. The fit was performed using a modified Hagedorn function (Eq. 4.18).*
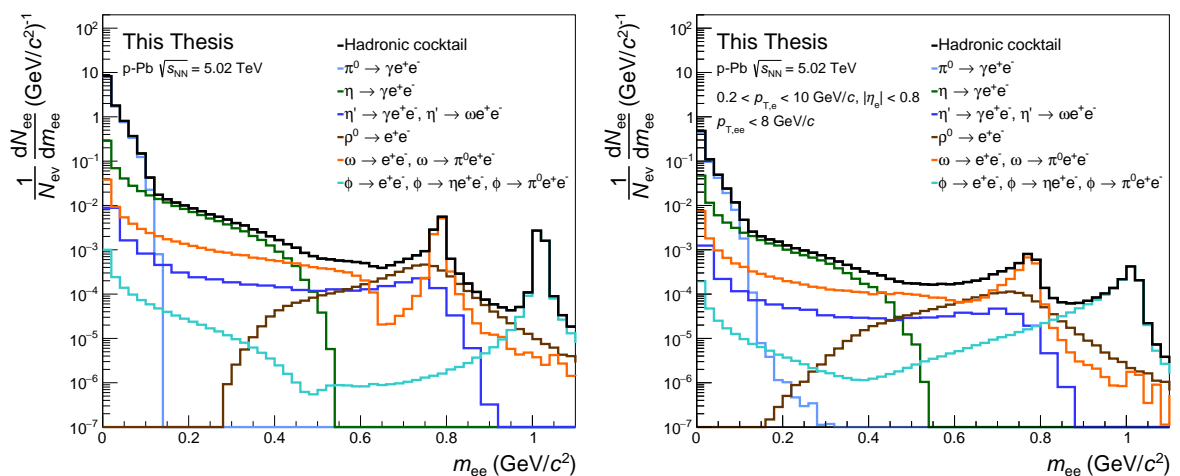
Figure 4.23: *The expected dielectron yield per event from light-flavour hadron decays in p–Pb collision at $\sqrt{s_{\mathrm{NN}}} = 5.02$ TeV as a function of m_{ee}. The left plot shows the generated expected yield without detector effects and fiducial selection criteria. The right plot shows the expected yield after both detector effects and fiducial selection criteria have been applied.*

POWHEG [140–142] (POsitive Weight Hardest Emission Generator) is a NLO event generator used to calculate the initial hard scattering processes at NLO, which can then be passed to any MC parton shower generator, in this case PYTHIA 6.4. The calculations involving POWHEG employed the CTEQ6.6 PDF [143].

In order to treat the simulations in the same manner as the data, the signal is extracted via the like-sign subtraction method (outlined in Section 4.3). Simulations including a small rapidity shift to account for the asymmetric beam energies were also performed and found to have a very small effect. For the first time in the high energy regime, dielectron production measurements at the same energy in both pp and p–Pb collisions are now available. As a result, the shapes of the simulated differential e^+e^- cross sections from $c\bar{c}$ and $b\bar{b}$ decays could be scaled to the measured e^+e^- cross sections, rather than relying on FONLL scaled cross sections, which introduces extra uncertainties, as has been the case so far. The measured $d\sigma_{c\bar{c}}/dy|_{y=0}$ and $d\sigma_{b\bar{b}}/dy|_{y=0}$ in pp collisions at $\sqrt{s} = 5.02$ TeV were determined via a double-differential fit in m_{ee} and $p_{T,ee}$ in the intermediate mass region $(1.1 < m_{ee} < 2.7 \,\text{GeV}/c^2)$ with the procedure covered in detail here [83], and an overview given with the results presented in Section 2.6. After scaling the heavy-flavour simulations to the measured pp cross sections, the contributions are then scaled by the atomic number of the Pb ion (A = 208). This scaling assumption is the simplest approach, and only assumes that production rate in p–Pb collisions is a superposition of 208 pp collisions. The final simulated e^+e^- yield per event from open heavy-flavour decays in p–Pb collisions at $\sqrt{s_{NN}} = 5.02$ TeV is presented in Fig. 4.24 for both POWHEG (solid lines) and PYTHIA 6.4 (dashed lines). As with the results from the pp measurement, in the intermediate mass region where the double differential fit was performed the two generators are in agreement. However, due to the substantially different measured $d\sigma_{c\bar{c}}/dy|_{y=0}$ and $d\sigma_{b\bar{b}}/dy|_{y=0}$ (listed in Table 2.1), discrepancies of ∼10-15% are visible in low-m_{ee} region $m_{ee} \lesssim 1.1 \,\text{GeV}/c^2$, where the differences in the production mechanisms for heavy-flavour generation between the two event generators becomes more substantial. Current uncertainties from both the data and from the light-flavour cocktail prevent any capitalisation on this aspect, however, if the prompt and non-prompt sources could be separated, via a multiplicity or *DCA* dependent study, then these generation processes could be explored and the results fed back into the MC generators. This idea is discussed more in the outlook (see Chapter 6).
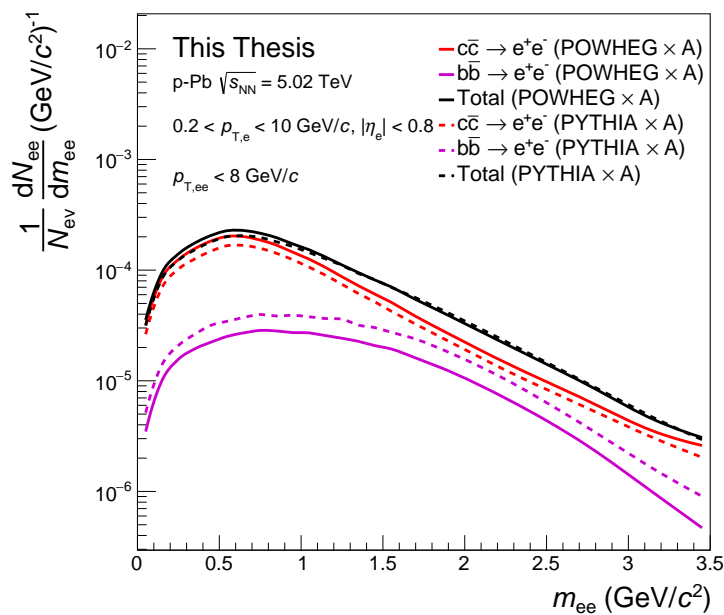
Figure 4.24: *The expected dielectron yield per event in p–Pb collisions at $\sqrt{s_{NN}} = 5.02$ TeV from c$\bar{c}$ (red) and b$\bar{b}$ (pink) decays as a function of m_{ee}. The simulated yields, performed with POWHEG (solid) and PYTHIA 6.4 (dashed), are scaled to the dielectron cross section measured in pp collision at $\sqrt{s_{NN}} = 5.02$ TeV [83], and multiplied by the atomic number of the Pb ion (A = 208).*

4.6.3 J/ψ

To generate the J/ψ contribution to the expected dielectron yield, the J/ψ p_T spectrum in p–Pb collisions at $\sqrt{s_{NN}} = 5.02$ TeV by ALICE [144] is first parametrised. The measurement and resulting fit are shown on the left in Fig. 4.25, along with the central, upper, and lower fits, and is parametrised with the following function

$$\frac{\mathrm{d}^2 N}{\mathrm{d}p_T \mathrm{d}y} = A \cdot \frac{p_T}{\left(1 + \frac{p_T^2}{B^2}\right)^2}, \tag{4.19}$$

where A and B are the fit parameters. The J/ψ dielectron decays are simulated using PHOTOS [145], which also includes the radiative QED decay (J/$\psi \to \gamma e^+ e^-$), and are scaled to the parametrised fit, before the smearing matrices and fiducial selection criteria are applied. The final contribution to the dielectron yield from J/ψ decays is shown on the right in Fig. 4.25 as a function of m_{ee}.
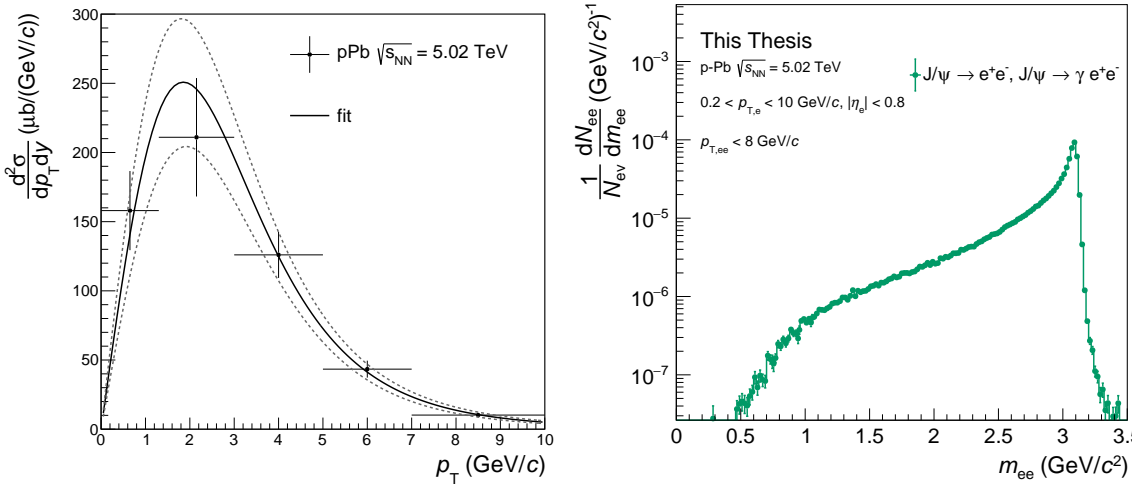
Figure 4.25: *The fit to the measured* J/ψ p_T *spectrum (left) in p–Pb collisions at* $\sqrt{s_{NN}} = 5.02$ *TeV [144] used as input to generate the contribution to the dielectron yield (right). The* J/ψ *decay is performed with PHOTOS [145] and also accounts for the radiative decay (*J/$\psi \to \gamma e^+ e^-$ *).*

4.6.4 Systematic Uncertainties

The systematic uncertainties of the hadronic cocktail originate from three main sources; branching ratios, parametrisations/fits, and cross sections. Each particle and the corresponding systematic uncertainty is listed in Table 4.8. The final uncertainty of the

cocktail is the weighted quadratic sum of the individual components, where the weighting factors are the relative contributions of each decay to the total cocktail. The uncertainty of the π^0 stems from two sources. The parametrisation uncertainty from the fit to the $\pi^{\pm}$ p_{T} spectrum, which is obtained by varying the fit up and down by the statistical and systematic uncertainties added in quadrature (see ratio in Fig. 4.20), and amounts to 10%. And an additional uncertainty from the $\pi^0/\pi^{\pm}$ ratio, which is determined by varying the first fit parameter of the fit function by $\pm 5\%$ (see right plot in Fig. 4.20), and results in an uncertainty of 2%. The uncertainty on the η/π^0 ratio comes from a variation of the fit parameters, with the result indicated by the light dashed grey lines in Fig. 4.21. An additional p_{T}-dependent uncertainty is considered which begins at 20% and decreases linearly to 7% at $p_{\mathrm{T}} = 10$ GeV/c. It is introduced to cover any potential biases from using such a wide range of energies and collision systems, and is added in quadrature with the η/π^0 ratio uncertainty. A 20% systematic uncertainty on the ω and ρ^0 ratio fits are determined by comparing the same ratios from measurements and simulations in pp collisions at $\sqrt{s} = 5.02$ TeV [146] and $\sqrt{s} = 2.76$ TeV. A 20% systematic uncertainty is also applied to the m_T scaling factor used for the η' generation, which is in agreement with previous ALICE dielectron papers [84, 85]. The parametrisation uncertainties of ϕ and J/ψ contributions are obtained directly from the fit procedure on data by again varying the fit up and down by the uncertainties of the data added in quadrature (see Fig. 4.22 and Fig. 4.25). The systematic uncertainty of the heavy-flavour cross sections are from the fit procedure to the pp data (covered in Section 4.6.2), and are the result of the statistical and systematic uncertainties of the data points themselves. As the measurement in pp collisions was also performed in the dielectron decay channel, the branching ratio uncertainty is ignored. The final systematic uncertainty assigned to the dielectron cocktail is presented in Fig. 4.26 as a function of m_{ee}.

Particle	BR (%)	Parametrisation (%)	Cross Section (%)
π^0	2.98	11	0.0
η	5.80	20 - 1 (p_T dep.)	0.0
η'	6.38	20	0.0
ρ^0	1.11	20	0.0
ω	1.92	20	0.0
ϕ	1.02	3	0.0
$c\bar{c}$	0.00	0	11.2
$b\bar{b}$	0.00	0	18.2
J/ψ	0.54	17	0.0

Table 4.8: *Summary of systematic uncertainties assigned to the hadronic cocktail. For each each particle the sources of uncertainties are listed as a percentage. Parametrisations cover uncertainties during the fitting procedures, and cross section uncertainties on the heavy-flavour contributions arise from the fitting procedure to the pp results (as outlined in Section 4.6.2). The final uncertainty is determined by adding the individual contributions in quadrature.*
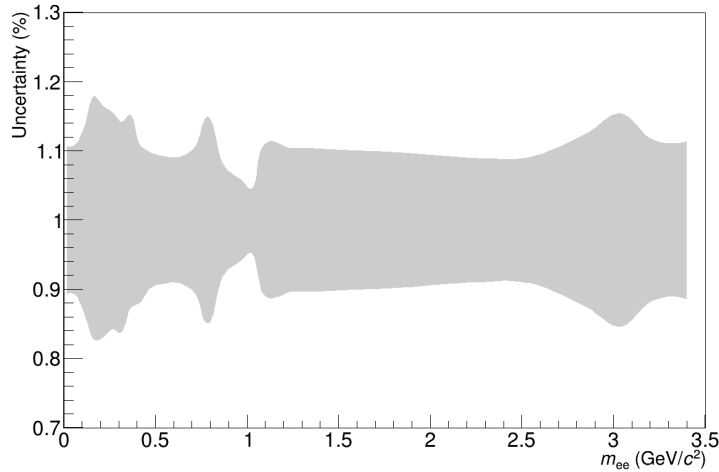
Figure 4.26: *The final systematic uncertainty on the hadronic cocktail as a function of m_ee. The final systematic uncertainty is calculated by weighting each individual contribution by the particles relative fraction in the cocktail and adding the contributions in quadrature.*

4.6.5 Additional Models

Two additional models are calculated and will be covered in this section. The final comparisons with the data are presented in Chapter 5.

Thermal Dielectron Production

A thermal model for dielectron production, outlined in Section 4.6.5, was calculated for p–Pb collisions at $\sqrt{s_{\mathrm{NN}}} = 5.02$ TeV by Ralf Rapp, and follows the procedure outlined in [63]. The temperature of the system is determined with an expanding fireball calculation for a mean charged-particle multiplicity at midrapidity of $\langle \mathrm{d}N_{ch}/\mathrm{d}y \rangle = 20$ (which corresponds to the data in this thesis) and is corrected for weak decay feed-down. The equation of state has a cross-over temperature $T_{\mathrm{c}} = 170$ MeV ,which is extracted from lattice QCD calculations, as well as a chemical freeze-out temperature $T_{\mathrm{ch}} = 160$ MeV. The standard ρ^0 contribution to the cocktail is removed and replaced by a broadened ρ^0 from the hadronic phase. The same kinematic restrictions on p_{T} and η as in this analysis are applied, however the detector resolution effects (discussed in Section 4.4.2) are not accounted for and no uncertainties on the calculations are available.

In Fig. 4.27, the predictions are shown as a function of m_{ee} in the top panel, and in the two investigated mass ranges as a function of $p_{\mathrm{T,ee}}$ in the lower two panels. As a function of m_{ee}, the partonic contribution from the QGP is dominant over the hadronic contribution for the whole range, although both contribute roughly the same amount around the ρ^0 peak. The total thermal contribution varies as a function of m_{ee} and $p_{\mathrm{T,ee}}$ with respect to the hadronic cocktail, with a maximum of $\approx 10\%$. The exact variation can be seen in the ratio presented in Fig. 5.5. The thermal contributions as a function of $p_{\mathrm{T,ee}}$ are calculated for the lower mass range ($0.5 < m_{\mathrm{ee}} < 1.1\,\mathrm{GeV}/c^2$) and the intermediate mass range ($1.1 < m_{\mathrm{ee}} < 2.7\,\mathrm{GeV}/c^2$). For both $p_{\mathrm{T,ee}}$ predictions, the QGP is the dominant source in the lower $p_{\mathrm{T,ee}}$ range ($p_{\mathrm{T,ee}} < 3\,\mathrm{GeV}/c$), whereas at higher $p_{\mathrm{T,ee}}$ they are approximately equivalent. In both cases, the thermal contribution as a fraction of the hadronic cocktail is $\approx 10\%$ for $p_{\mathrm{T,ee}} \lesssim 1\,\mathrm{GeV}/c$. While the predictions as a function of $p_{\mathrm{T,ee}}$ only extend to $p_{\mathrm{T,ee}} < 5\,\mathrm{GeV}/c$ (the analysis extends to $p_{\mathrm{T,ee}} < 8\,\mathrm{GeV}/c$), the contributions from thermal sources decrease much faster than the known hadronic sources at high $p_{\mathrm{T,ee}}$, therefore ensuring the discrepancy in the kinematic ranges can be safely ignored.
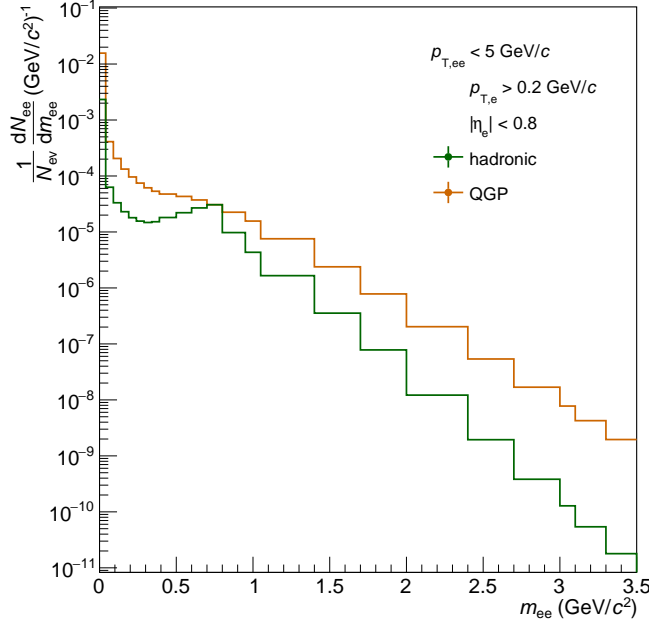
(a) m_{ee}
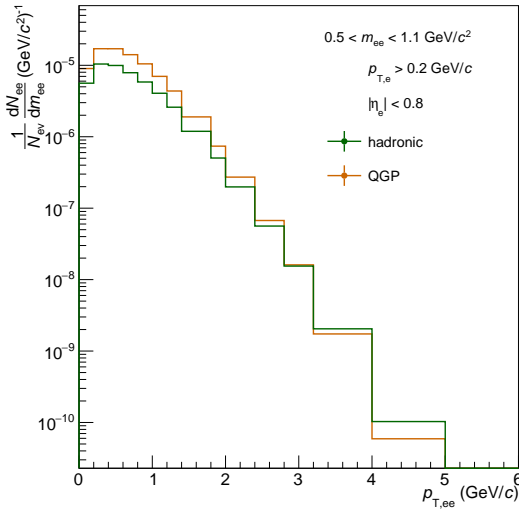
(b) $p_{T,ee}$: $0.5 < m_{ee} < 1.1\,\mathrm{GeV}/c^2$
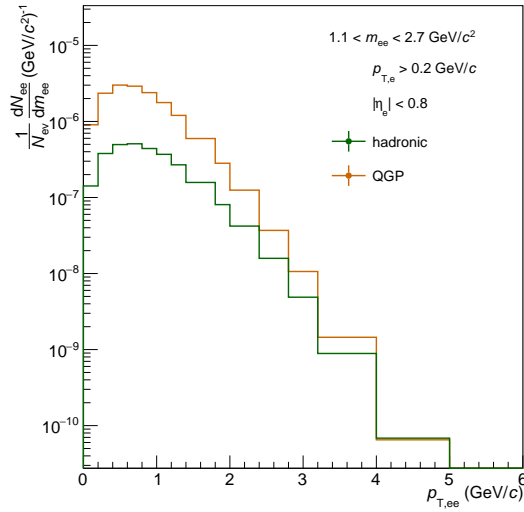
(c) $p_{T,ee}$: $1.1 < m_{ee} < 2.7\,\mathrm{GeV}/c^2$

Figure 4.27: *Differential thermal dielectron production calculations for p–Pb collisions at $\sqrt{s_{\mathrm{NN}}} = 5.02$ TeV as a function of m_{ee}, as well as $p_{T,ee}$ for two mass ranges, shown separately for the partonic (orange) and hadronic (green) phases. The model parameters are outlined in the text and the full procedure is presented in detail in [63].*

81

Cold Nuclear Matter

To estimate potential cold nuclear matter effects on the dielectron spectrum in p–Pb collisions, the charm contribution to the spectrum was modified using the EPS09 set of nPDFs [69]. An introduction to nPDFs was presented in Section 2.2. To calculate the EPS09 nPDFs, three different types of measurements were incorporated into the global analysis which calculates the nPDFs at NLO in pQCD: deep inelastic $l+A$ scattering, Drell-Yan dilepton production in pA collisions, and inclusive pion production in $d+A$ and pp collisions at RHIC. The resulting modification factors (defined in Eq. 2.2) are shown for two Q scales for Pb ions in Fig. 4.28 for valence quarks (R_V^{Pb}), sea quarks (R_S^{Pb}) and gluons (R_G^{Pb}).
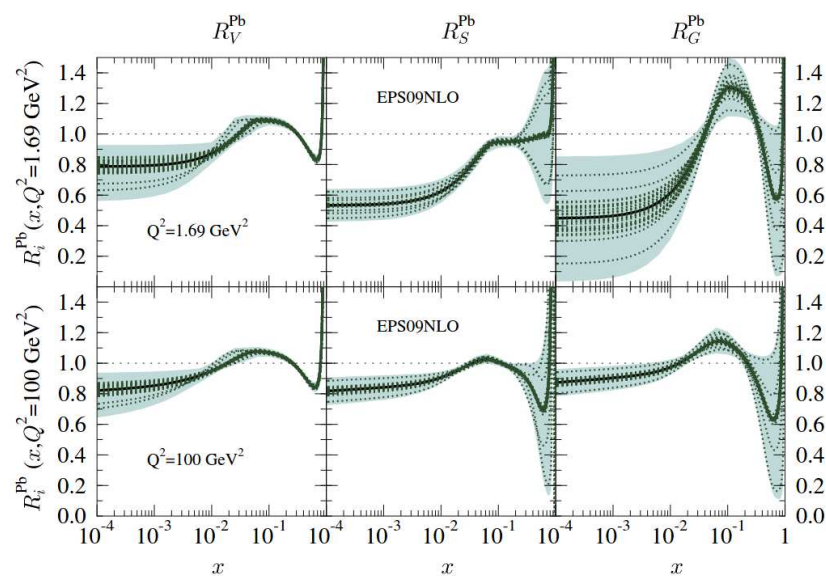
Figure 4.28: *The nuclear modifications for valence quarks (R_V^{Pb}), sea quarks (R_S^{Pb}) and gluons (R_G^{Pb}) for Pb at $Q^2 = 1.69$ GeV^2 and $Q^2 = 100$ GeV^2 [69]. The black line represents the result with the best fit, and the thick green band the uncertainty.*

In Fig. 4.29, the modified charm contribution to the dielectron yield in p–Pb collisions is presented as a function m_{ee}, along with the upper and lower uncertainty ranges which come from the nPDFs themselves. The modified charm production rate compared to the vacuum rate is reduced by $\approx 14\%$ across the whole mass range, which is expected at LHC energies where the energy transfers are large (high Q) and the fractional energy contained by each parton low (small x). Beauty production is expected to be less affected by the nPDFs and was therefore not simulated.
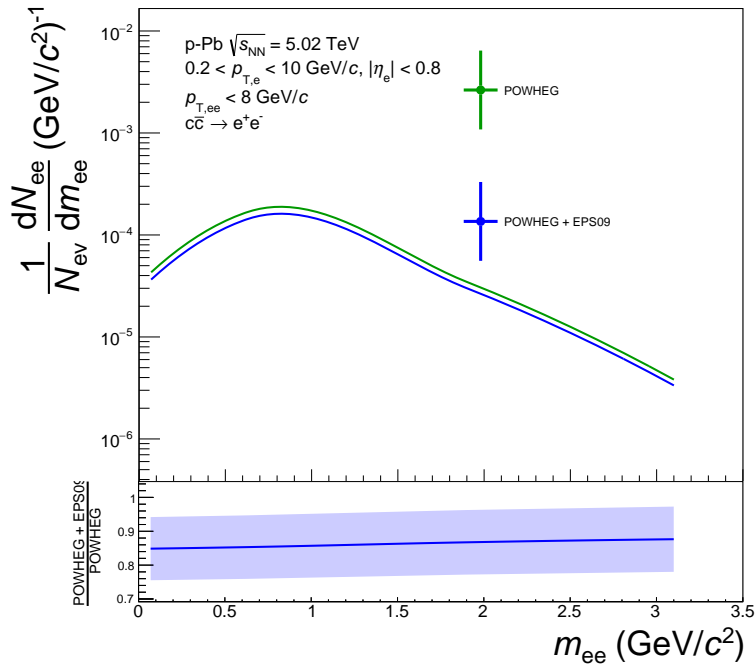
Figure 4.29: *The expected dielectron yield from open-charm hadron decays in p–Pb collisions at $\sqrt{s_{\mathrm{NN}}} = 5.02$ TeV. The vacuum expectation from POWHEG (green) is compared to calculations incorporating the EPS09 nPDF (blue). The blue band in the ratio represents the uncertainty on the nPDF.*

5 Results

The following sections present the first dielectron analysis of p–Pb collisions at $\sqrt{s_{\mathrm{NN}}} = 5.02$ TeV. The data were recorded with the ALICE detector in 2016 at midrapidity ($|\eta| < 0.8$) and are corrected for the reconstruction efficiency. However, the final results are not corrected for the acceptance (p_{T} and η restrictions), as extrapolating down to $p_{\mathrm{T}} = 0$ GeV/c would introduce a significant dependence on the chosen model. The data are compared to the hadronic cocktail as outlined in Section 4.6, as well as two additional theoretical predictions described in Section 4.6.5. In Section 5.1, the differential cross section measurements are presented and compared to the hadronic cocktail, in Section 5.2 the data are compared to the additional model calculations and in Section 5.3 the analysis results are combined with measurements of dielectron production recorded in pp collisions at $\sqrt{s} = 5.02$ TeV with the resulting differential nuclear modification factors presented.

All results are shown as differential cross sections calculated with

$$\frac{\mathrm{d}^2\sigma_{\mathrm{e}e}}{\mathrm{d}m_{\mathrm{ee}}\mathrm{d}p_{\mathrm{T,ee}}} = \frac{1}{\mathcal{L}_{\mathrm{int}}}\frac{1}{\Delta m_{\mathrm{ee}}}\frac{1}{\Delta p_{\mathrm{T,ee}}}\frac{S(m_{\mathrm{ee}},\ p_{\mathrm{T,ee}})}{\epsilon_{\mathrm{e}e}(m_{\mathrm{ee}},\ p_{\mathrm{T,ee}})}, \tag{5.1}$$

where

- Δm_{ee} and $\Delta p_{\mathrm{T,ee}}$ are the widths of the m_{ee} and $p_{\mathrm{T,ee}}$ intervals, respectively

- $\mathcal{L}_{\mathrm{int}}$ the integrated luminosity discussed in Section 4.1 ($\mathcal{L}_{\mathrm{int}} = 299 \pm 11\ \mu\mathrm{b}^{-1}$)

- $S(m_{\mathrm{ee}},\ p_{\mathrm{T,ee}})$ the uncorrected dielectron yield detailed in Section 4.3

- and $\epsilon_{\mathrm{ee}}(m_{\mathrm{ee}},\ p_{\mathrm{T,ee}})$ the reconstruction efficiency covered in Section 4.4.

5.1 Minimum-Bias Dielectron Production

The measured dielectron production in p–Pb collisions at $\sqrt{s_{\mathrm{NN}}} = 5.02$ TeV is presented in this section and compared to the hadronic cocktail which does not consider thermal dielectrons or a suppression of the open charm hadron production rate. Figures 5.1 and 5.2 show the differential dielectron cross section as a function of m_{ee} integrated over $0 < p_{\mathrm{T,ee}} < 8\,\mathrm{GeV}/c$ with the heavy-flavour contributions calculated with POWHEG and PYTHIA 6.4, respectively, and scaled by the atomic mass number of the Pb ion (as discussed in Section 4.6.2). The vertical blue bars represent the statistical uncertainty on the data while the boxes represent the systematic uncertainty. The expected dielectron cross section is labelled 'Hadronic cocktail' with the grey band representing the total uncertainty on the calculations. The 3.7% normalisation uncertainty originating from the luminosity determination is not plotted. The data are in agreement over the entire m_{ee} range with the hadronic cocktail within uncertainties. However, in the very low mass range ($m_{\mathrm{ee}} < 0.14\,\mathrm{GeV}/c^2$) the data are slightly yet systematically underestimated. In this region no large effects from either of the models are predicted. As the $\pi^{\pm}$ p_{T} spectrum is used to construct the other light-flavour cocktail contributions (excluding ϕ), this discrepancy must be kept in mind when formulating conclusions in the other ranges that include significant light-flavour contributions.

In Figs. 5.3 and 5.4, the differential dielectron cross section is presented as a function of $p_{\mathrm{T,ee}}$ in four non-overlapping mass intervals.

The region $0 < m_{\mathrm{ee}} < 0.14\,\mathrm{GeV}/c^2$ is dominated by π^0 Dalitz decays. As a result, the open heavy-flavour contributions do no significantly contribute and the agreement with data is essentially identical between the two cocktail calculations using the different event generators to produce the heavy-flavour contributions. For $p_{\mathrm{T,ee}} < 3\,\mathrm{GeV}/c$, the expected cross section appears to be slightly overestimated in particular at very low $p_{\mathrm{T,ee}}$, however the large systematic uncertainties on both the data and calculation ensure the discrepancy is not significant.

For $0.14 < m_{\mathrm{ee}} < 0.5\,\mathrm{GeV}/c^2$, the spectrum is dominated by η decays but also has significant contributions from ω and $c\bar{c}$. As in the π^0 dominated region, the data appear to be slightly underestimated in the low-$p_{\mathrm{T,ee}}$ region, however again no discrepancy between data and simulation can be discerned due to the large systematic uncertainties.

The low-mass region (LMR) spans $0.5 < m_{\mathrm{ee}} < 1.1\,\mathrm{GeV}/c^2$ and contains the resonances from the vector mesons. Here the largest contributor is from $c\bar{c}$ decays for $p_{\mathrm{T,ee}} \lesssim 3\,\mathrm{GeV}/c$ and from $b\bar{b}$ decays for $p_{\mathrm{T,ee}} \gtrsim 3\,\mathrm{GeV}/c$, with the exact crossover

between these two $p_{T,ee}$ ranges varying slightly between the different generators. Contributions from the light-flavour decays are present over the whole $p_{T,ee}$ range. For $p_{T,ee} \lesssim 1\,\mathrm{GeV}/c$ the data appear to be slightly overestimated, however the large uncertainties preclude any strong statements.

Lastly, the intermediate-mass region (IMR) $1.1 < m_{ee} < 2.7\,\mathrm{GeV}/c^2$ is essentially dominated by the open heavy-flavour hadron decays, primarily from c$\bar{\text{c}}$, with a small contribution from J/ψ. As the heavy-flavour cross section fit in pp was performed in this mass region, both generators fit the data well with only a minor difference between the two. Both generators show a hint of an excess in the low-$p_{T,ee}$ region ($p_{T,ee} < 1.2\,\mathrm{GeV}/c$), while being in agreement for higher $p_{T,ee}$.
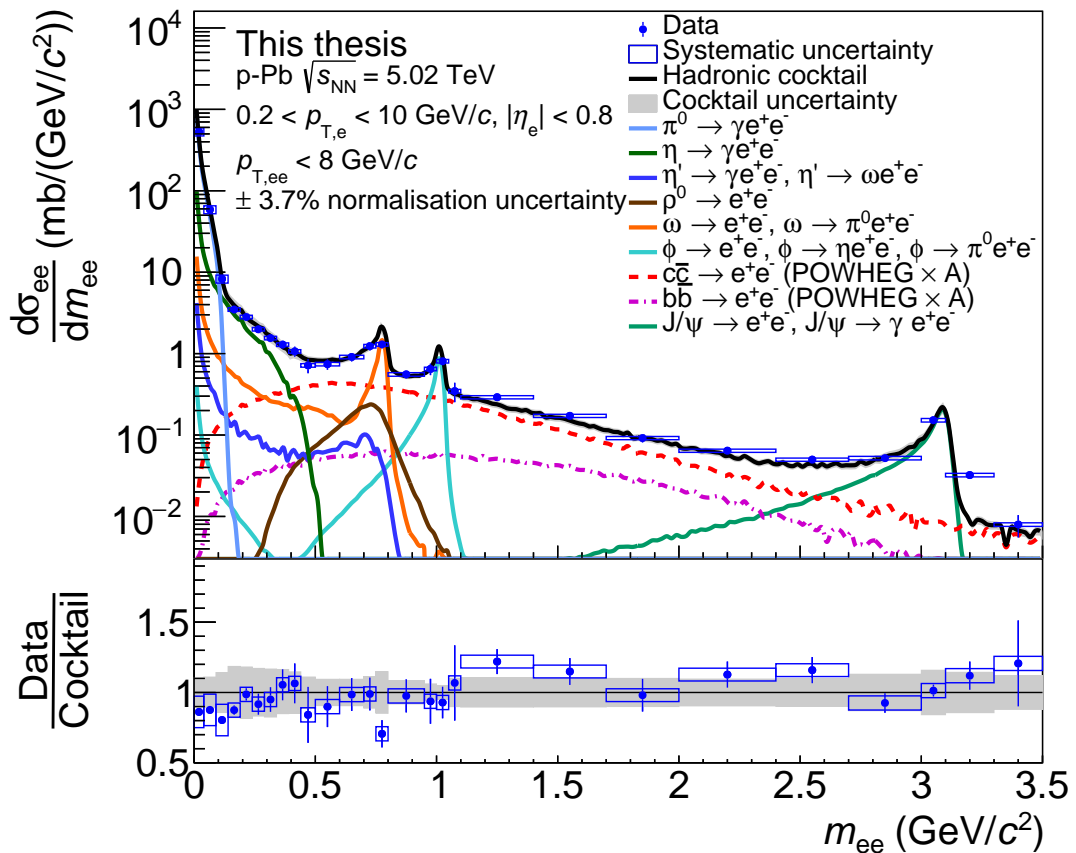
Figure 5.1: *The differential dielectron cross section measured in p–Pb collisions at $\sqrt{s_{NN}} = 5.02$ TeV as function of m_{ee} integrated over the range $0 < p_{T,ee} < 8\,\mathrm{GeV}/c$. The data are compared to a hadronic cocktail with the heavy-flavour contributions, generated with POWHEG, fit to the cross sections measured in pp collisions [83] and scaled with the atomic mass number of the Pb nucleus (A = 208). The grey band represents the systematic uncertainty of the hadronic cocktail. The lower panel shows the ratio of the data over the hadronic cocktail.*
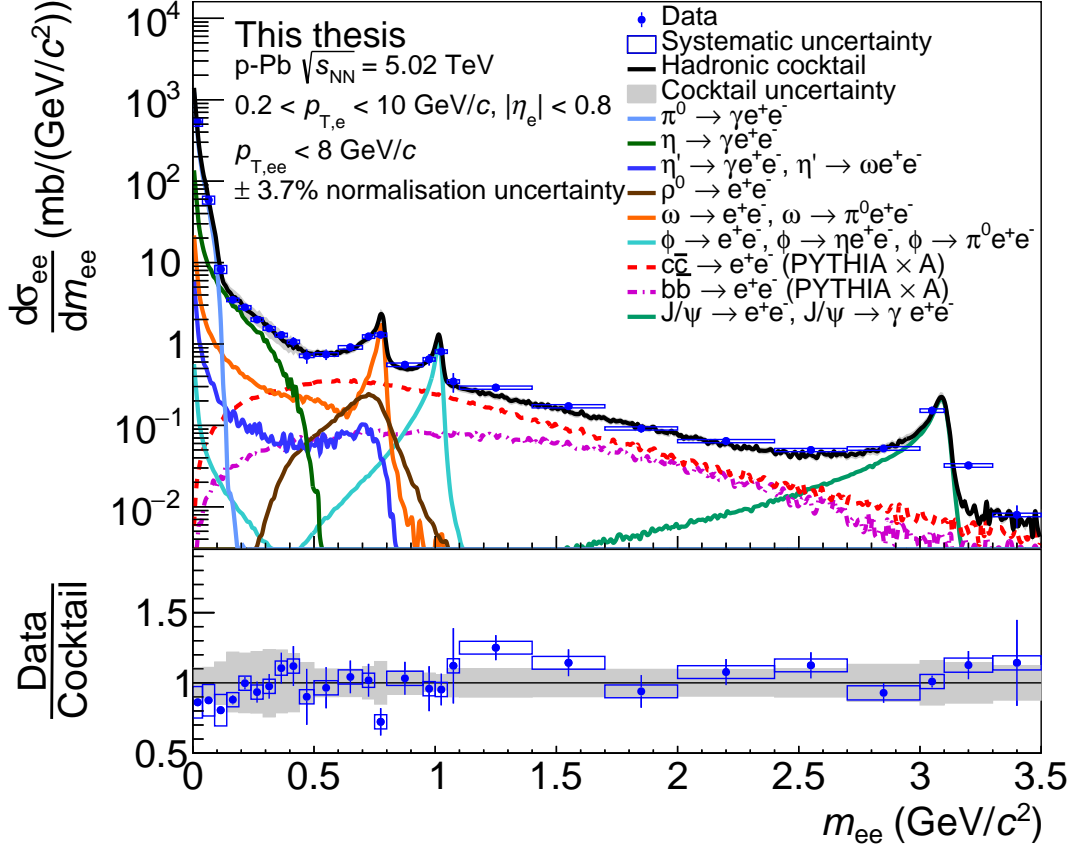
Figure 5.2: *The differential dielectron cross section measured in p–Pb collisions at $\sqrt{s_{NN}} = 5.02$ TeV as function of m_{ee} integrated over the range $0 < p_{T,ee} < 8\,GeV/c$. The data are compared to a hadronic cocktail with the heavy-flavour contributions, generated with PYTHIA 6, fit to the cross sections measured in pp collisions [83] and scaled with the atomic mass number of the Pb nucleus (A = 208). The grey band represents the systematic uncertainty of the hadronic cocktail. The lower panel shows the ratio of the data over the hadronic cocktail.*

(a) $m_{ee} < 0.14 \, \mathrm{GeV}/c^2$

(b) $0.14 < m_{ee} < 0.50 \, \mathrm{GeV}/c^2$

(c) $0.50 < m_{ee} < 1.10 \, \mathrm{GeV}/c^2$

(d) $1.10 < m_{ee} < 2.70 \, \mathrm{GeV}/c^2$
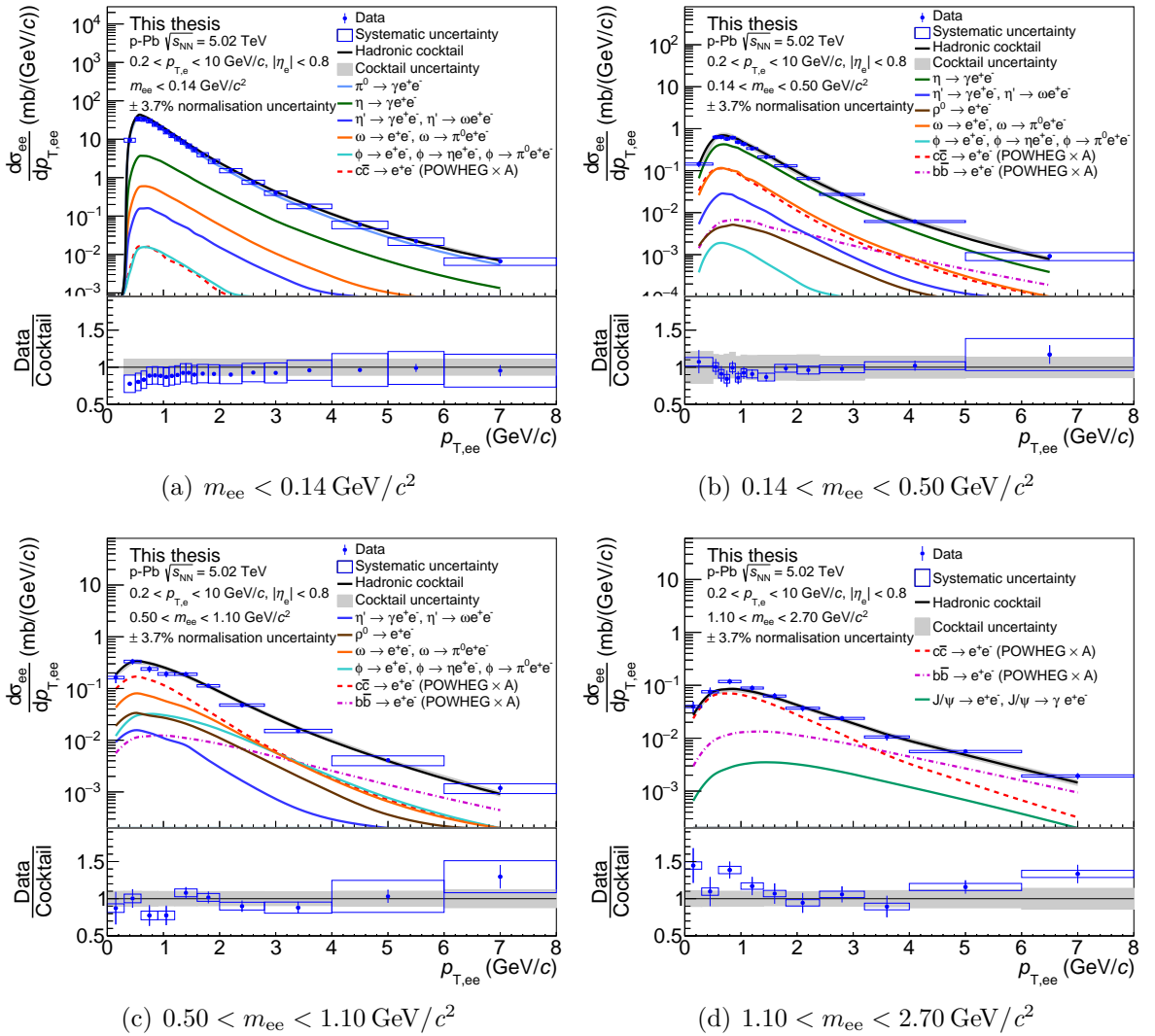
Figure 5.3: *The differential dielectron cross section measured in p–Pb collisions at $\sqrt{s_{\mathrm{NN}}} = 5.02$ TeV as function of $p_{\mathrm{T,ee}}$ in four separate mass intervals. The data are compared to a hadronic cocktail with the heavy-flavour contributions, generated with POWHEG, fit to the cross sections measured in pp collisions [83] and scaled with the atomic mass number of the Pb nucleus (A = 208). The grey band represents the systematic uncertainty of the hadronic cocktail. The lower panel shows the ratio of the data over the hadronic cocktail.*

(a) $m_{ee} < 0.14\,\mathrm{GeV}/c^2$

(b) $0.14 < m_{ee} < 0.50\,\mathrm{GeV}/c^2$

(c) $0.50 < m_{ee} < 1.10\,\mathrm{GeV}/c^2$

(d) $1.10 < m_{ee} < 2.70\,\mathrm{GeV}/c^2$
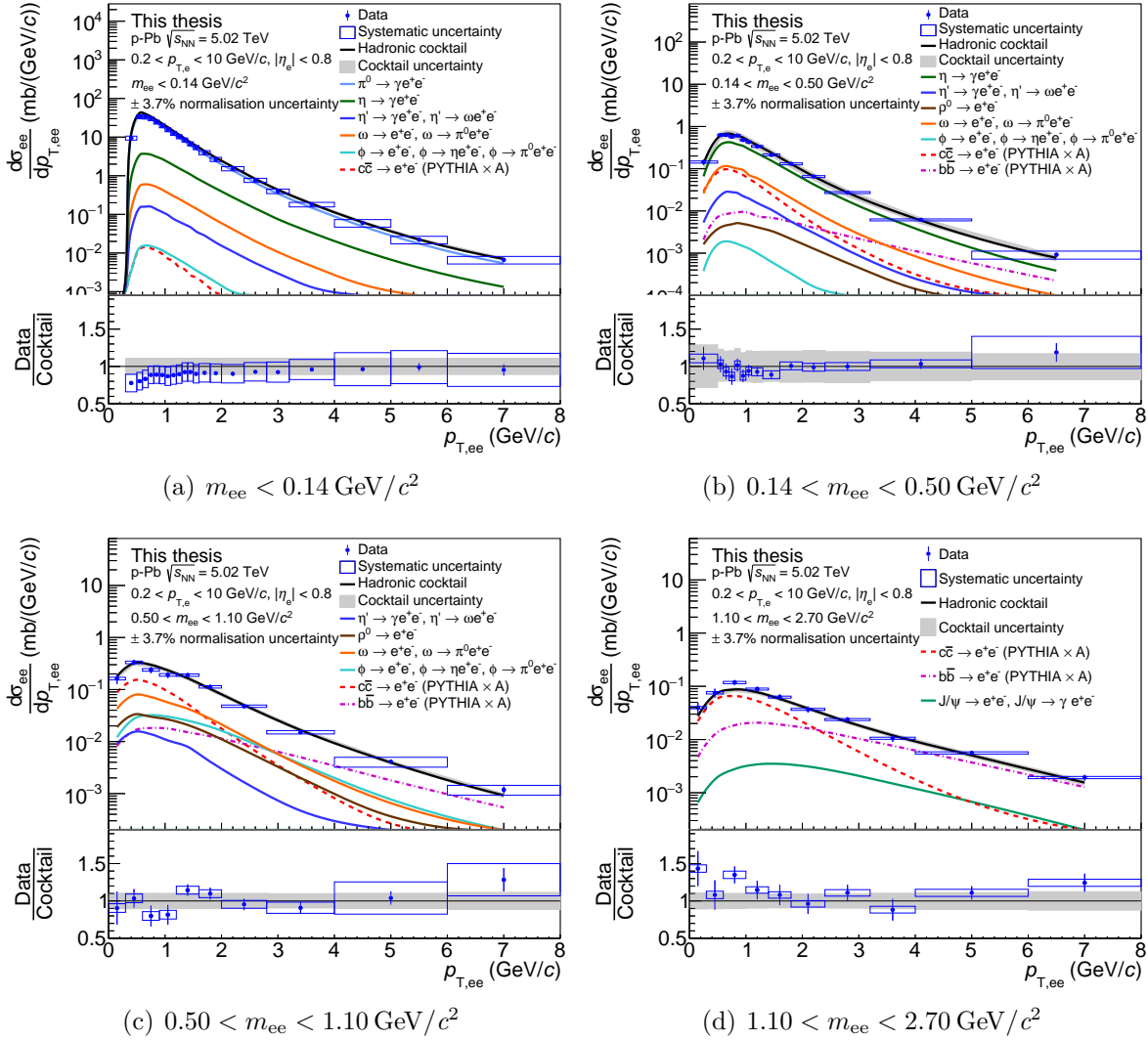
Figure 5.4: *The differential dielectron cross section measured in p–Pb collisions at $\sqrt{s_{NN}} = 5.02$ TeV as function of $p_{T,ee}$ in four separate mass intervals. The data are compared to a hadronic cocktail with the heavy-flavour contributions, generated with PYTHIA 6, fit to the cross sections measured in pp collisions [83] and scaled with the atomic mass number of the Pb nucleus (A = 208). The grey band represents the systematic uncertainty of the hadronic cocktail. The lower panel shows the ratio of the data over the hadronic cocktail.*

89

5.2 Model Comparisons

In this section two additional models are compared to the measured dielectron production. As the measurable differences between the heavy-flavour generators PYTHIA 6.4 and POWHEG are negligible for this analysis, and the computation time to fully calculate the expected suppression is significant, only comparisons using POWHEG will be shown from this point on. Furthermore, comparisons with data are not shown for the range $m_{ee} < 0.5 \, \mathrm{GeV}/c^2$, as both models do not alter the comparison significantly enough in this region to have a notable effect given the current precision. In the figures presented in this section, the contribution labelled "QGP + HG (Rapp et al.)" corresponds to a thermal model which includes dielectron production from the partonic phase (QGP) and the hadronic phase (HG = hadron gas). As the hot hadronic phase calculations also contain a broadened ρ^0 mass shape due to interactions with the medium, the in-vacuum ρ^0 shown in the hadronic cocktail is subtracted from the thermal cocktail before determining the comparison shown in the ratio. The thermal calculations do not include detector resolution effects and no uncertainties were provided. The label containing "EPS09" indicates that the calculation includes a suppressed open charm hadron production rate and was calculated using the EPS09 nPDFs. The red uncertainty band on the EPS09 model originates from the nPDF calculations and does not include the uncertainties from the other dielectron sources shown in grey.

In Fig. 5.5, the measured differential dielectron cross section as a function of m_{ee} integrated over $0 < p_{T,ee} < 8 \, \mathrm{GeV}/c$ is now compared to the hadronic cocktail, which contains all sources above the black line, as well as the two additional models. In the lower panel all three calculations are compared to the data. In the LMR, the data are in agreement with all three cocktails within uncertainties. The model with a suppressed open charm hadron production is slightly favoured by the data which is systematically below unity in this region, however, both the deviation from unity by the data and the expected additional thermal contribution is small, prohibiting any of the calculations from being excluded. In the IMR, the situation is similar but reversed. In this case, the thermal model is favoured over the open charm hadron suppressed model, however when the uncertainties from the CNM calculations and the hadronic cocktail contributions are considered, the data would not rule it out.

In Fig. 5.6, the measured differential cross section is further investigated as a function of $p_{T,ee}$ for the LMR (left) and the IMR (right). In the LMR, the charm suppressed model would be favoured over the thermal model for $p_{T,ee} < 2 \, \mathrm{GeV}/c$. For higher $p_{T,ee}$, both

models marginally improve the agreement with the central value of the data but within uncertainties all three models agree with the data. In the IMR for $p_{\text{T,ee}} \lesssim 1.5\,\text{GeV}/c$, the thermal model is clearly favoured over the charm suppressed model by the data, although the modification to the significance of the disagreement between data and expectation is not greatly improved, again due to the non-negligible uncertainties. For $p_{\text{T,ee}} > 1.5\,\text{GeV}/c$, both models do not alter the cocktail in a consequential manner, and the data are in agreement with all three calculations.
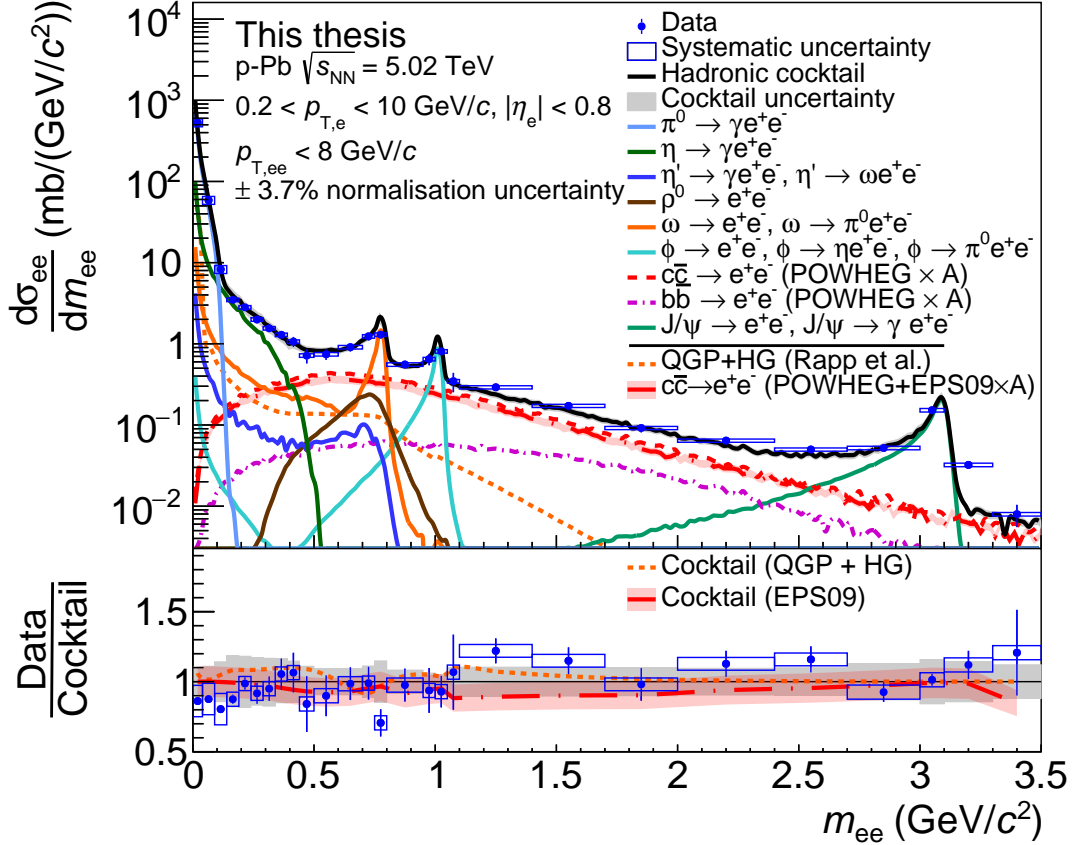
Figure 5.5: *The differential dielectron cross section measured in p–Pb collisions at $\sqrt{s_{\text{NN}}} = 5.02$ TeV as function of m_{ee} integrated over the range $0 < p_{\text{T,ee}} < 8\,\text{GeV}/c$. The data are compared to a hadronic cocktail with the heavy-flavour contributions, generated with POWHEG, fit to the cross sections measured in pp collisions [83] and scaled with the atomic mass number of the Pb nucleus (A = 208). Additional models including thermal sources of dielectrons (QGP + HG) [63] and a suppression of the open charm hadron production rate (POWHEG+EPS09) [69] are also presented. In the lower ratio panel all three calculations are compared to the data. The grey band represents the systematic uncertainty of the hadronic cocktail, and the red band represents the uncertainty of the nPDF calculation.*

Figure 5.6: *The differential dielectron cross section measured in p–Pb collisions at $\sqrt{s_{\mathrm{NN}}} = 5.02$ TeV as function of $p_{\mathrm{T,ee}}$ in two separate mass intervals. The data are compared to a hadronic cocktail with the heavy-flavour contributions, generated with POWHEG, fit to the cross sections measured in pp collisions [83] and scaled with the atomic mass number of the Pb nucleus (A = 208). Additional models including thermal sources of dielectrons (QGP + HG) [63] and a suppression of the open charm hadron production rate (POWHEG+EPS09) [69] are also presented. In the lower ratio panel all three calculations are compared to the data. The grey band represents the systematic uncertainty of the hadronic cocktail, and the red band represents the uncertainty of the nPDF calculation.*

5.3 Nuclear Modification Factor

In this section the measured dielectron production in p–Pb collisions is compared to the dielectron production rates measured in pp collisions at the same center-of-mass energy ($\sqrt{s_{\mathrm{NN}}} = 5.02$ TeV). The pp measurements were presented in Section 2.6. The combined results are presented as differential nuclear modification factors (R_{pPb}), which were introduced in Eq. 1.9. The cocktail R_{pPb} uncertainties are the result of adding the π^0, ϕ and J/ψ uncertainties together in quadrature, weighted by their relative contributions as determined from the cocktail itself. All other uncertainties, for example, the η/π^0 parametrisation, are fully correlated and therefore cancel each other out. The normalisation uncertainty is not plotted, and is calculated by adding the uncertainties from both the pp and p–Pb luminosity scans in quadrature.

In Fig. 5.7, the dielectron R_{pPb} is presented as a function of m_{ee} and compared to

the hadronic cocktail as well as the two cocktails containing the previously introduced models. Again, the uncertainty plotted on the cocktail using the EPS09 nPDFs to model a suppressed open charm hadron production rate only shows the uncertainty stemming from the calculation on the nPDFs. The relative fraction of dielectrons from light-flavour decays, determined from the hadronic p–Pb cocktail, is also plotted in light green. Overall the data are reproduced by the hadronic cocktail within uncertainties. A different scaling behaviour between the light-flavour and heavy-flavour production rates seen in data is reproduced by the calculations. As heavy-flavour quarks are produced in initial hard processes (detailed in Section 2.2) a scaling with N_{coll} (or equivalently A when measuring cross sections as was done here) is expected, whereas light-flavour production is governed by soft processes (outlined in Section 2.1) which depend on the size of the interacting system and therefore scales proportionally to N_{part}.

In the LMR, the expected R_{pPb} is consistently higher than the data, however it is in agreement within uncertainties. In this region, the suppressed open charm hadron production cocktail appears to be more favoured by the data, but neither model can be ruled out. In the IMR, the hadronic cocktail reproduces the data within uncertainties, however the addition of a thermal source does slightly improve the agreement. The EPS09 cocktail on the other hand seems somewhat disfavoured by the data in this region, but cannot be ruled out when considering the uncertainties.

In Fig. 5.8, the R_{pPb} is further analysed as a function of $p_{\mathrm{T,ee}}$ in the LMR (left) and the IMR (right). The relative fraction of light-flavour production is not plotted in either case. In the LMR, the light-flavour fraction is essentially constant at $\approx 20\%$, and in the IMR it is $\approx 0\%$. The R_{pPb} in the LMR is well reproduced by the hadronic cocktail, although the addition of a suppression factor to the open charm hadron production rate does increase the agreement at very low $p_{\mathrm{T,ee}}$ ($p_{\mathrm{T,ee}} \lesssim 3\,\mathrm{GeV}/c$)). The cocktail with thermal contributions is disfavoured by the data for $p_{\mathrm{T,ee}} \lesssim 1\,\mathrm{GeV}/c$. In the IMR all three cocktails are in agreement with the data for $p_{\mathrm{T,ee}} > 1\,\mathrm{GeV}/c$. Below this, the cocktail with thermal contributions noticeably improves the agreement with the data, however none of the models can be definitively ruled out due to the large uncertainties.
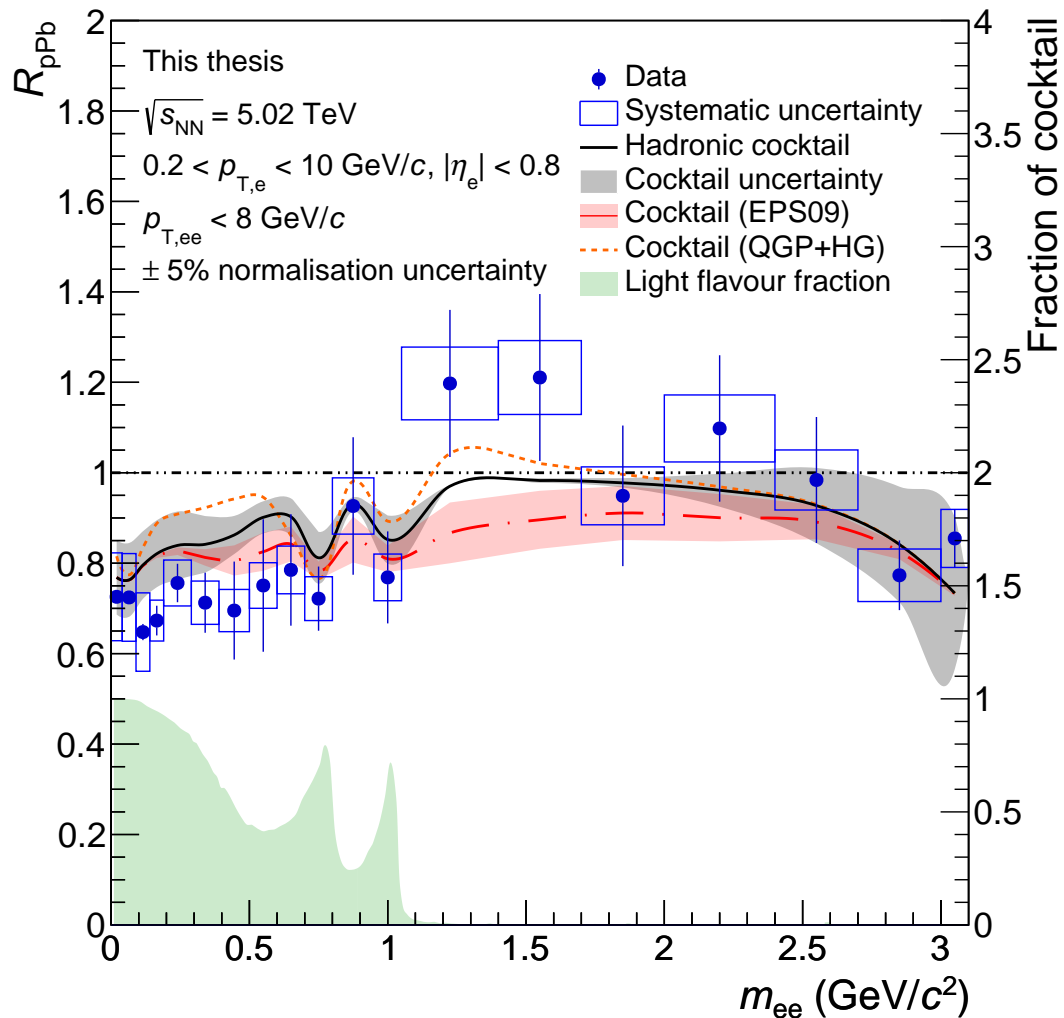
Figure 5.7: *The dielectron nuclear modification factor (R_{pPb}) as a function of m_{ee} measured at midrapidity at $\sqrt{s_{NN}} = 5.02$ TeV [83]. The hadronic cocktail shown in black represents the baseline expectation with the heavy-flavour contributions generated with POWHEG and the total uncertainty shown in grey. The cocktail (EPS09) (red) incorporates a suppression to the open charm hadron production rate [69], whereas the cocktail (QGP+HG) (orange) includes thermal radiation from the partonic and hadronic phases [63]. The red band represents the uncertainty from the nPDF calculation and the green shaded area is the fraction of light-flavour decays determined from the hadronic p–Pb cocktail.*

(a) $0.50 < m_{ee} < 1.10\,\mathrm{GeV}/c^2$

(b) $1.10 < m_{ee} < 2.70\,\mathrm{GeV}/c^2$
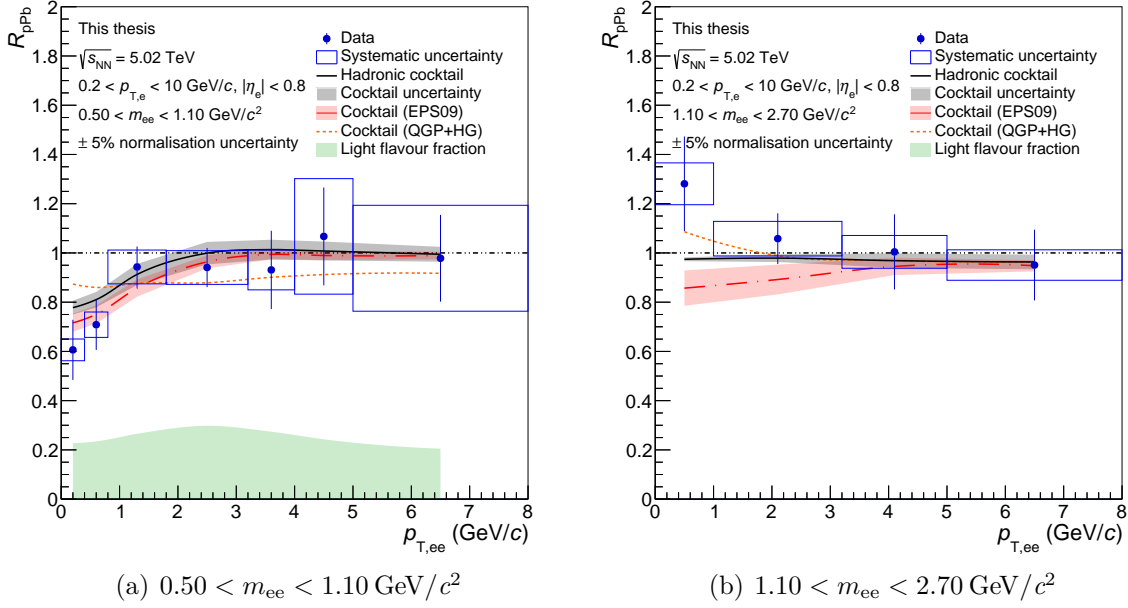
Figure 5.8: *The dielectron nuclear modification factor (R_{pPb}) as a function of $p_{T,ee}$ measured at midrapidity at $\sqrt{s_{NN}} = 5.02$ TeV in two mass intervals [83]. The hadronic cocktail (black) represents the baseline expectation with the heavy-flavour contributions generated with POWHEG and the total uncertainty shown in grey. The cocktail (EPS09) (red) incorporates a suppression to the open charm hadron production rate [69], whereas the cocktail (QGP+HG) (orange) includes thermal radiation from the partonic and hadronic phases [63]. The red band represents the uncertainty from the nPDF calculation.*

6 Summary and Outlook

This thesis presents the first-ever dielectron measurement in p–Pb collisions in the TeV energy regime ($\sqrt{s_{\mathrm{NN}}} = 5.02$ TeV). The measurement is performed at midrapidity ($|\eta| < 0.8$) with a minimum transverse momentum requirement of $p_{\mathrm{T}} > 0.2\,\mathrm{GeV}/c$. The differential dielectron cross section measurement is compared to data driven simulations containing all known hadronic decay sources of dielectrons: π^0, η, η', ρ^0, ω, ϕ, and J/ψ, as well as semi-leptonic decays from open heavy-flavour hadrons ($c\bar{c}$ and $b\bar{b}$). The semi-leptonic open heavy-flavour hadron decays are generated using two different event generators PYTHIA 6.4 and POWHEG. The heavy-flavour contributions are fit to a dielectron cross section measurement in pp collisions at $\sqrt{s} = 5.02$ TeV in the intermediate mass range (IMR, $1.1 < m_{\mathrm{ee}} < 2.7\,\mathrm{GeV}/c^2$) where $c\bar{c}$ and $b\bar{b}$ dominate dielectron production. The resulting fits are then scaled by the atomic mass of the Pb ion for comparison with this analysis.

Both calculations are able to reproduce the measured dielectron production reasonably well over the entire investigated range within the uncertainties, however systematic deviations from the calculations can be seen. The differences in the heavy-flavour cross sections measured using the two generators, which stem from the different heavy-flavour production mechanisms implemented by the event generators, is not large enough to be able to distinguish between the two at the current level of precision. In the low-mass region (LMR, $0.5 < m_{\mathrm{ee}} < 1.1\,\mathrm{GeV}/c^2$), the data are slightly overestimated, which could hint at a potential suppression to the dielectron production, whereas in the IMR, the data are slightly underestimated, potentially indicating the additional presence of a hot medium producing dielectrons.

These two proposed scenarios are also calculated and compared to the data. The first additional simulation includes a source of thermal dielectrons which are produced both in the partonic stage (the QGP), and in the hadronic stage which also induces a broadening of the ρ^0 mass shape due to interactions with the medium. The second supplementary calculation modified the open charm hadron production rate in the collisions due to the presence of the Pb ion and is calculated using the EPS09 nPDFs, one of the so-called

cold nuclear matter effects. Including the suppressed open charm hadron production does improve the agreement with the data in the LMR, however all calculations are within the uncertainties. In the IMR, the addition of the thermal calculations helps the agreement with the data, and in this case the charm suppression is somewhat disfavoured. Ultimately, given the large statistical uncertainties on the data and large systematic uncertainties on the calculations, none of the simulated expectations can be ruled out.

Also presented in this thesis is the dielectron nuclear modification factor (R_{pPb}). The results of this thesis were combined with the dielectron production measured in pp collisions at $\sqrt{s} = 5.02$ TeV, and compared to calculations including those with thermal dielectron production or a suppressed open charm hadron production. The R_{pPb} highlights the different scaling behaviour between the light-flavour and heavy-flavour particles, with the atomic scaling of the heavy-flavour appearing to be compatible with the data within the large uncertainties. The additional models improve the agreement between data and simulation analogously to the results described above, but the final result suffers from large statistical uncertainties preventing concrete conclusions from being drawn. Furthermore, one must also consider the possibility that an extra thermal contribution may present as well as a suppression of the open charm hadron production rate. When looking at the dielectron m_{ee} and $p_{\mathrm{T,ee}}$ spectra, these competing effects would appear to cancel each other out. So, while distinguishing the extreme cases (i.e., only one additional modification) from the hadronic cocktail will soon be within reach, one could still not be certain that both additional effects are not present.

The results presented in this thesis highlight the necessity to separate the prompt dielectron sources from the non-prompt dielectron sources, that is the light-flavour and potential thermal contributions from the open heavy-flavour decays. This idea was investigated in pp collisions at $\sqrt{s} = 7$ TeV [84] by harnessing the separating power of the distance-of-closest approach (DCA) variable which measures the distance between the reconstructed vertex and the dielectron tracks, allowing one to separate the prompt from non-prompt sources. Using this approach, it would be possible to isolate the thermal (prompt) contributions in the IMR, allowing for a precise determination of the contribution. Additionally, studies are planned to investigate the multiplicity dependence of dielectron production. As the rate of thermal dielectron production is predicted to scale faster with increasing multiplicity than the light-flavour hadron contributions, analyses of the multiplicity dependence could shed light on the thermal production rate. Finally, precise neutral meson measurements, in particular π^0 and η p_{T} spectra which extend down to low p_{T}, would significantly increase the discriminating power of dielectron mea-

surements with respect to the models just discussed, and should therefore be prioritised.

Moving on to the future improvements to the ALICE detector itself, the current upgrades taking place during LHC Long-Term Shutdown 2 (LS2), predicted to end 2021, will include significant improvements to the ITS and TPC [147, 148]. These upgrades will increase the tracking and vertex reconstruction precision, which will further increase the separating power of the upcoming multiplicity and DCA dependent studies. The maximum data taking rate during Run 3 (2021-2024) is expected to increase by a factor of $\sim$50, and will greatly help the analyses by reducing the statistical uncertainties [149]. Further plans for Run 3 include data periods with a lowered magnetic field (B = 0.2 T). This would reduce the kinematic restrictions from $p_{\mathrm{T}} > 0.2\,\mathrm{GeV}/c$ to $p_{\mathrm{T}} > 0.075\,\mathrm{GeV}/c$, greatly increasing the acceptance and precision of the analysis in the very low-m_{ee} region. For LHC LS3 (2024-2027), a proposal to upgrade the three most inner layers of the ITS with advanced wafer-scale ultra-thin silicon sensors (MAPS technology) has been proposed [150], and would reduce the ITS material budget for the inner layers near the interaction point by a factor of six. In Run 5 (2032-2034) and beyond, plans to replace the whole ALICE detector with a detector comprised solely of cylindrical silicon detector layers has begun [151]. This detector would be close to massless and could extend the momentum range down to a few tens of MeV/c, substantially reduce the background coming from photon conversions due to interactions with the material, while handling luminosities 20 to 50 times higher than the Run 3 and 4 version of ALICE.

7 Appendix

7.1 ALICE Coordinate System

The coordinate system used by ALICE is a right-handed orthogonal Cartesian system with the beam interaction point centered at the origin $(x, y, z = 0)$. In Fig. 7.1 the ALICE detector is overlaid with the coordinate system axes, pointing in their positive directions, as well the associated angles. The azimuthal angle (φ) increases counter-clockwise from x ($\varphi = 0$) to y ($\varphi = \pi/2$). The polar angle (θ) ranges from z ($\theta = 0$) to the x, y plane ($\theta = \pi/2$) to $-z$ ($\theta = \pi$).
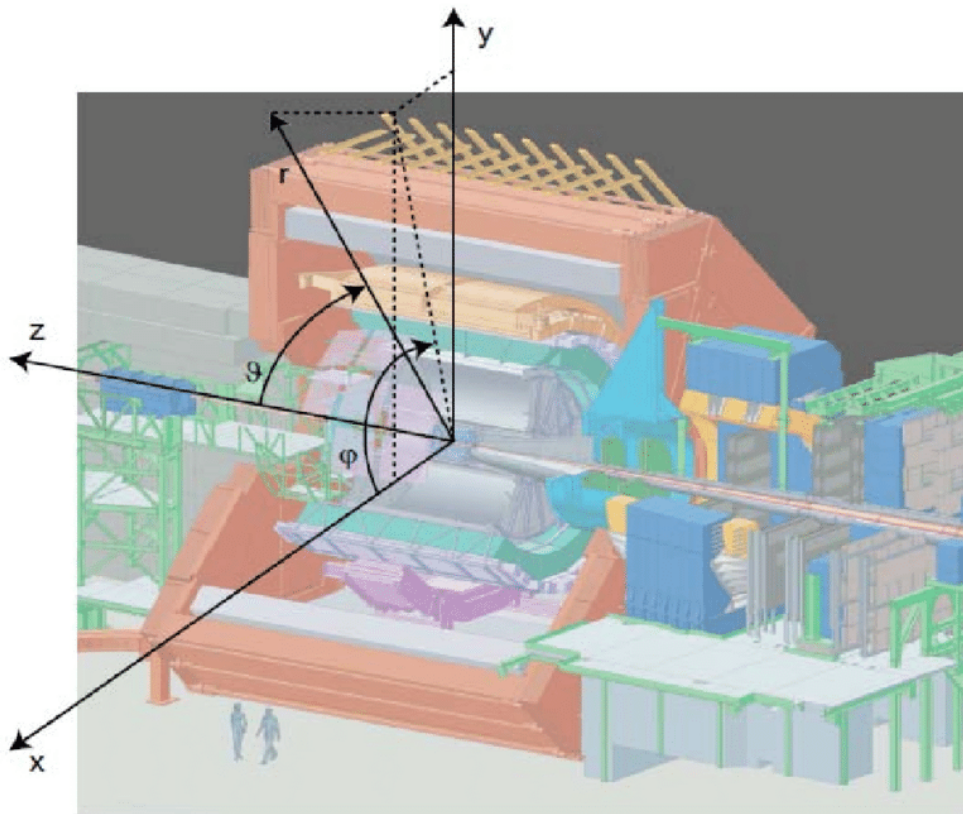

Figure 7.1: *Diagram of the ALICE detector indicating the coordinate system .*

7.2 Kinematic Variables

This section of the appendix presents the ALICE coordinate system and outlines how to calculate the kinematic variables used in this thesis and naturally uses natural units ($c = \hbar = 1$).

The energy and momentum of a particle can be written together in four-vector notation as

$$p_\mu = (E, p_x, p_y, p_z), \tag{7.1}$$

where E is the energy and $\vec{p} = (p_x, p_y, p_z)$ the momentum of the particle. As is the case for ALICE, the coordination system is chosen such that the beams velocity is in the z-direction.

The momentum of the particles created in the collision can then be separated into a longitudinal component (p_z), and a transverse component $\vec{p_T} = (p_x, p_y)$, with the magnitude of the transverse component calculated as

$$p_T = \sqrt{p_x^x + p_y^2}. \tag{7.2}$$

From this one can also define the transverse mass (m_T) as

$$m_T = \sqrt{m + p_T^2}, \tag{7.3}$$

which, like p_T, is a Lorentz invariant quantity under boosts along z.

Another useful kinematic variable at the single track level is rapidity (y) which is defined as

$$y = \frac{1}{2}\ln\left(\frac{E + p_z}{E - p_z}\right). \tag{7.4}$$

However, to calculate the rapidity of a track the mass of the particle in question must be known. As this is not always possible to determine, pseudo-rapidity (η) is more commonly used and is written as

$$\eta = -\ln\left(\tan\left(\frac{\theta}{2}\right)\right), \tag{7.5}$$

where θ is the polar angle between the z-axis and $\vec{p}$. In the limit where the particle's mass becomes negligible, i.e. $|\vec{p}| >> m$, then the pseudorapidity converges to the rapidity ($\eta \to y$).

In the case of a two-body decay, the invariant mass (m_{ee}) of the original particle can

be calculated with

$$m_{\text{ee}} = \sqrt{m_1^2 + m_2^2 + 2E_1 E_2 - 2\vec{p}_1 \cdot \vec{p}_2} \tag{7.6}$$

and the transverse momentum $(p_{\text{T,ee}})$ with

$$p_{\text{T,ee}} = \sqrt{(p_{x,1} + p_{x,2})^2 + (p_{y,1} + p_{y,2})^2} \tag{7.7}$$

where the subscripts 1 and 2 refer to the two decay products.

7.3 Run List

The table below lists the analysed runs in this thesis and corresponds to the data taking period `LHC16q`. The list was taken from the central *Data Preparation Group* wiki page, with the run list called

`RunList_LHC16q_pass1_CentralBarrelTracking_electronPID_20171129_v2.txt`

265309	265332	265334	265336
265338	265339	265342	265343
265344	265377	265378	265381
265383	265384	265385	265387
265388	265419	265420	265421
265422	265424	265425	265426
265427	265435	265499	265500
265501	265521	265525	

Table 7.1: *List of analysed run numbers from the data taking period LHC16q.*

7.4 PID with Machine Learning

While the PID procedure used in this thesis (outlined in Section 4.2.2) ensured that a high purity sample of electrons is selected, time was also spent investigating the benefits of using a Machine Learning (ML) approach for this step of the analysis. For these PID studies, the software package Toolkit for Multivariate Analysis (TMVA) [152] was used along side ROOT 6.13 [153]. The TMVA package is a comprehensive machine learning toolkit which provides a large number of different ML algorithms. During the PID studies many of these algorithms were tested, for example, neural networks, support vector machines etc, however the robustness of the Boosted Decision Tree (BDT) to overtraining as well as the conceptual simplicity of the final selection process made it an obvious choice.

A BDT is labelled as *supervised machine learning* as the algorithm is trained to classify signal from background, in this case electrons from all other particles, by using MC simulations from which the pdg codes can be used to provide feedback at each iteration ,allowing the algorithm to refine the classification decision boundary with each step. The classifier is provided with an input set of features x, along with the target classification (pdg code) y_0, and returns a value between -1 and 1 with -1, with values closer to 0 indicating more background-like tracks and values closer to 1 more signal-like tracks. To suppress the possibility of overtraining, that is learning not the true signal and background boundaries but rather learning fluctuations specific to the training data set, the MC data are split into subsets. The first data set is the *training set* which is used to perform the initial training of the classifier. The trained classifier is then applied to the second data subset, the *validation set*, in order to check for potential overtraining. This process is repeated many times with changes to the hyperparameters (the features of the algorithm which control the learning process) of the classifier until the desired signal and background separation is reached. For a thorough introduction to ML see [154].

During training, the BDT classifier was shown five features typically used in a dielectron analysis for electron PID: p_T, $n(\sigma_e^{ITS})$, $n(\sigma_e^{TPC})$, $n(\sigma_e^{TOF})$ and $n(\sigma_\pi^{TPC})$. An example of $n(\sigma_e^{TPC})$ vs p_T is shown in Fig. 4.6 after the PID selection criteria have been applied. A cursory hyperparameter scan was performed in order to determine a relatively good architecture, and after each scan both the training and validation outputs were compared in order to monitor any overtraining. A Kolmogorov-Smirnov test, which is a nonparametric test of equality which can be applied to two distributions, was also performed between the train/test outputs after each training cycle. Scans over the three

most common splitting criteria, Gini Index, Cross Entropy, and Misidentification were also performed, however no substantial differences were found, so the Gini Index was taken as it is least computationally greedy function.
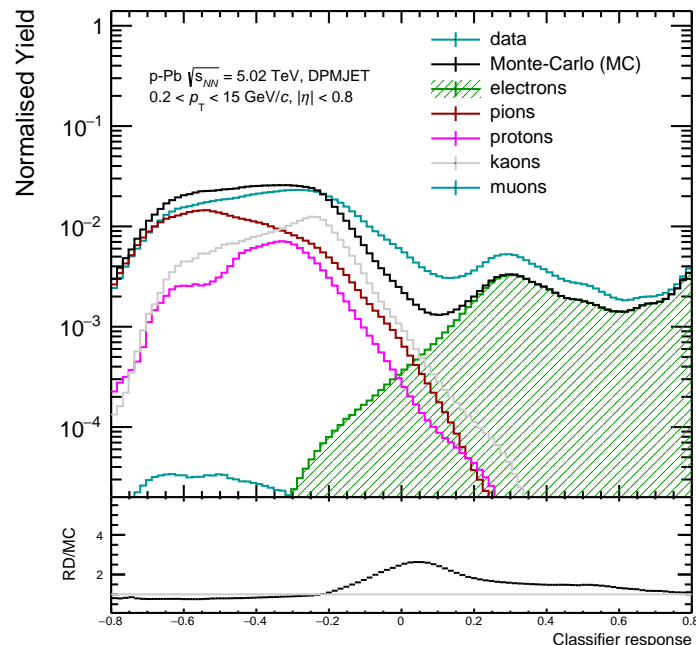
Figure 7.2: *BDT classifier response outputs compared between data and the corresponding Monte Carlo production. The classifier output from the Monte Carlo data is decomposed into its constituent particle species with the green area corresponding to electrons (signal). The lower plot shows the ratio of the classifier responses for data (RD) and Monte Carlo.*

The final architecture of the BDT is as follows: features = 5, max depth = 10, trees = 200, learning rate = 0.5, and minimum node size = $\sim 30,000$ tracks. The result of the classifier output is shown in Fig. 7.2. The classified MC tracks (black) can be decomposed into the constituent particle species via the track's pdg code and are also plotted. The classifier is also applied to the data (cyan) with the data/MC ratio shown in the lower panel. The classifier quite easily separates the majority of the electrons from the other tracks, however the region $-0.2 < x < 0.2$ contains both signal and background tracks in similar proportions. This region is the result of the fundamental separation power of each detector, and the intrinsic regions where electrons cannot be separated from other tracks in specific p_T intervals. The ratio plot indicates the agreement of the features

provided to classifier between data and MC simulations. Ideally, this ratio would be flat, meaning the MC simulations perfectly reproduce the data, however this is rare. In any case, the magnitude of the discrepancy can be quantified as a systematic uncertainty just like was done in the standard analysis by varying the selection criteria (for the BDT a simple cut on the MVA output), and calculating the final differences on the spectrum. As a result, the ML technique itself does not introduce additional uncertainties to the analysis.

To highlight the benefit of this approach, the BDT classifier was compared to what is labelled the "traditional approach" which is still quite common within HEP. In the traditional approach, each variable used for PID is sequentially restricted, and no two variables are simultaneously considered. The traditional selection criteria are listed in Fig. 7.3 where the electron PID efficiency and purity are compared between the two methods. The selection criteria on the BDT output was chosen so as to obtain a similar purity as the traditional method. While the traditional method has a near flat 70% efficiency over the whole p_T range, the BDT is able to increase this to near 100% outside of the three drops which correspond to regions where π^0's, K's and protons cannot be fully disentangled from electrons. This significant increase in efficiency translates to an approximately 10-15% decrease in the statistical uncertainties of the measured dielectron spectrum, with the systematic uncertainties remaining essentially the same. Given a data set with full PID capabilities (e.g., ITS included), the ML approach is clearly an improvement. However, in the case of this thesis, the data set could be doubled by excluding the ITS PID information, and therefore the benefits from the ML approach were somewhat nullified. For future analyses a ML approach should definitely be considered.
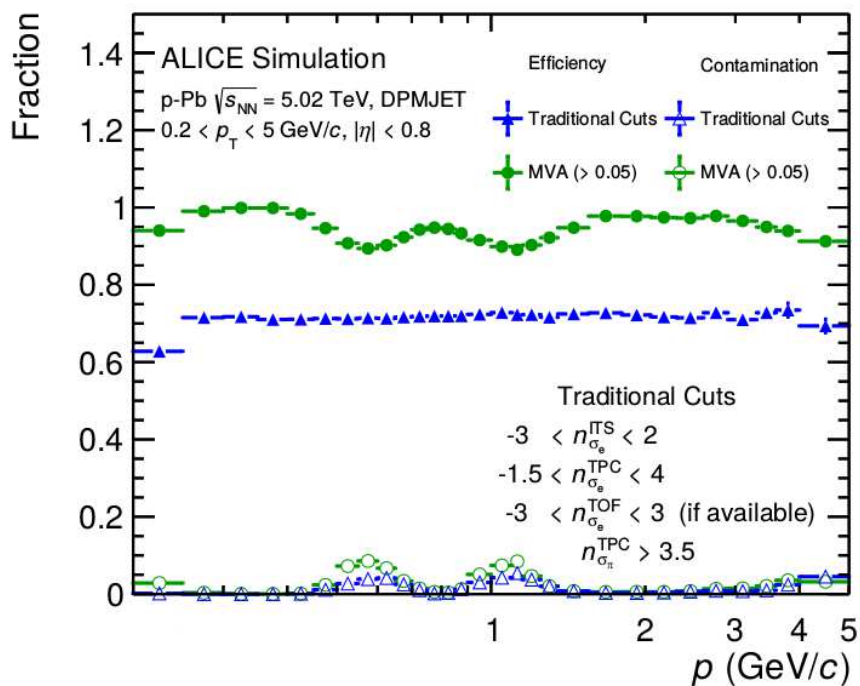
ALI-SIMUL-149767

Figure 7.3: *Electron PID efficiency and contamination compared between the BDT algorithm outlined in the text and a traditional PID approach whose selection criteria are listed in the lower right box.*

7.5 Track Selection Variations

Cut	$n_{cr.rows,min}^{TPC}$	$n_{find.cl.,min}^{TPC}$	$n_{cr.rows,min}^{TPC}/n_{find.cl.}^{TPC}$	$n_{cl.}^{ITS}$	$\chi_{max.}^{2}/n_{cl.}^{ITS}$
1	100	80	0.8	3	5.5
2	80	70	0.7	2	4.5
3	110	90	0.6	3	6.5
4	90	80	0.8	2	6.5
5	100	100	0.8	3	4.5
6	100	80	0.8	3	6.5
7	80	70	0.6	2	5.5
8	100	90	0.9	3	5.5
9	80	90	0.6	3	4.5
10	110	90	0.8	3	5.5
11	90	100	0.7	2	4.5
12	100	100	0.6	3	5.5
13	80	80	0.8	2	5.5
14	100	80	0.8	3	6.5
15	80	100	0.5	3	6.5
16	110	70	0.6	2	5.5
17	80	70	0.7	3	4.5
18	90	100	0.8	3	6.5
19	100	90	0.8	2	6.5
20	100	80	0.9	3	6.5

Table 7.2: *Track selection criteria variations used to determine the associated systematic uncertainties.*

Cut	$n\sigma_e^{TPC}$	$n\sigma_e^{TOF}$	$n\sigma_\pi^{TPC}$	$n\sigma_K^{TPC}$	$n\sigma_p^{TPC}$
1	2.5	2	3.0	-3.5 - 2.5	-3.0 - 3.0
2	3.0	3	3.0	-3.0 - 3.0	-2.5 - 3.5
3	3.0	3	4.0	-3.0 - 3.0	-2.5 - 3.5
4	3.5	3	3.5	-2.5 - 3.5	-3.0 - 3.0
5	3.0	2	3.5	-3.0 - 3.0	-2.5 - 3.5
6	3.0	3	3.5	-3.5 - 2.5	-3.0 - 3.0
7	2.5	3	3.5	-2.5 - 3.5	-2.5 - 3.5
8	3.0	3	4.0	-3.0 - 3.0	-3.0 - 3.0
9	3.5	2	3.5	-2.5 - 3.5	-2.5 - 3.5
10	3.5	3	3.5	-2.5 - 3.5	-2.5 - 3.5
11	3.0	2	4.0	-3.0 - 3.0	-3.0 - 3.0
12	3.0	2	4.5	-3.5 - 2.5	-3.0 - 3.0
13	3.5	3	3.0	-3.5 - 2.5	-2.5 - 3.5
14	3.0	3	3.0	-3.0 - 3.0	-3.5 - 2.5
15	2.5	2	3.5	-3.0 - 3.0	-2.5 - 3.5
16	2.5	3	4.0	-3.5 - 2.5	-3.0 - 3.0
17	3.0	3	3.5	-3.0 - 3.0	-2.5 - 3.5
18	3.0	2	4.0	-3.0 - 3.0	-3.0 - 3.0
19	3.0	2	4.0	-2.5 - 3.5	-3.0 - 3.0
20	2.5	3	3.5	-3.0 - 3.0	-3.0 - 3.0

Table 7.3: *PID selection criteria variations used to determine the associated systematic uncertainties. When only one number is listed the selection or rejection limits are symmetrical.*

Bibliography

[1] **Planck** Collaboration, N. Aghanim *et al.*, "Planck 2018 results. VI. Cosmological parameters," *Astron. Astrophys.* **641** (2020), p. A6, `arXiv:1807.06209 [astro-ph.CO]`. (Cited on page 1)

[2] C. Schmidt and S. Sharma, "The phase structure of QCD," *J. Phys. G* **44** no. 10, (2017), p. 104002, `arXiv:1701.04707 [hep-lat]`. (Cited on page 1)

[3] **ALICE** Collaboration. `https://alice-figure.web.cern.ch/node/11218`, accessed 2020-03-23. (Cited on page 1, 37)

[4] **ALICE** Collaboration, "The ALICE experiment at the CERN LHC," *JINST* **3** (2008), p. S08002. (Cited on page 1, 37, 39, 40, 41, 43)

[5] **Particle Data Group** Collaboration, "Review of Particle Physics," *Progress of Theoretical and Experimental Physics* **2020** no. 8, (2020). (Cited on page 2, 3, 4, 5, 8, 21, 23, 40)

[6] W. Pauli, "The Connection Between Spin and Statistics," *Phys. Rev.* **58** (1940), pp. 716–722. (Cited on page 2)

[7] F. Englert and R. Brout, "Broken Symmetry and the Mass of Gauge Vector Mesons," *Phys. Rev. Lett.* **13** (1964), pp. 321–323. (Cited on page 3)

[8] P. W. Higgs, "Broken Symmetries and the Masses of Gauge Bosons," *Phys. Rev. Lett.* **13** (1964), pp. 508–509. (Cited on page 3)

[9] G. S. Guralnik, C. R. Hagen, and T. W. B. Kibble, "Global Conservation Laws and Massless Particles," *Phys. Rev. Lett.* **13** (1964), pp. 585–587. (Cited on page 3)

[10] Cush, "Wikipedia, The Free Encyclopedia," 2019. `https://commons.wikimedia.org/wiki/File:`

`Standard_Model_of_Elementary_Particles.svg`. [Online; accessed 20-July-2020]. (Cited on page 3)

[11] J. Greensite, *An Introduction to the Confinement Problem*, vol. 821. 2011. (Cited on page 4)

[12] D. J. Gross and F. Wilczek, "Ultraviolet Behavior of Non-Abelian Gauge Theories," *Phys. Rev. Lett.* **30** (1973), pp. 1343–1346. (Cited on page 4)

[13] K. G. Wilson, "Confinement of quarks," *Phys. Rev. D* **10** (1974), pp. 2445–2459. (Cited on page 5)

[14] **HPQCD, UKQCD, MILC, and Fermilab Lattice** Collaboration, C. Davies *et al.*, "High precision lattice QCD confronts experiment," *Phys. Rev. Lett.* **92** (2004), p. 022001, `arXiv:hep-lat/0304004`. (Cited on page 5)

[15] R. Hagedorn, "Statistical thermodynamics of strong interactions at high-energies," *Nuovo Cim. Suppl.* **3** (1965), pp. 147–186. (Cited on page 5)

[16] N. Cabibbo and G. Parisi, "Exponential Hadronic Spectrum and Quark Liberation," *Phys. Lett. B* **59** (1975), pp. 67–69. (Cited on page 5)

[17] P. Bicudo, "QCD confinement and chiral crossovers, two critical points?," *PoS* **FACESQCD** (2010), p. 015. (Cited on page 6)

[18] K. Rajagopal and F. Wilczek, *The Condensed matter physics of QCD*, pp. 2061–2151. 2000. `arXiv:hep-ph/0011333`. (Cited on page 6)

[19] P. Braun-Munzinger, V. Koch, T. Schäfer, and J. Stachel, "Properties of hot and dense matter from relativistic heavy ion collisions," *Phys. Rept.* **621** (2016), pp. 76–126, `arXiv:1510.00442 [nucl-th]`. (Cited on page 7)

[20] V. Koch, "Introduction to chiral symmetry," in *3rd TAPS Workshop on Electromagnetic and Mesonic Probes of Nuclear Matter*. 1995. `arXiv:nucl-th/9512029`. (Cited on page 7)

[21] H. Sazdjian, "Introduction to chiral symmetry in QCD," *EPJ Web Conf.* **137** (2017), p. 02001, `arXiv:1612.04078 [hep-ph]`. (Cited on page 7, 8)

[22] W. W. S. Klimt, M. Lutz, "Chiral phase transition in the SU(3) Nambu and Jona-Lasinio model," *Physics Letters B* **249** no. 3, (1990), pp. 386 – 390. (Cited on page 8, 9)

[23] G. Hering, *Dielectron production in heavy ion collisions at 158 GeV/c per nucleon.* PhD thesis, Darmstadt, Tech. Hochsch., 2001. `arXiv:nucl-ex/0203004`. (Cited on page 8, 9)

[24] G. E. Brown and M. Rho, "Scaling effective Lagrangians in a dense medium," *Phys. Rev. Lett.* **66** (1991), pp. 2720–2723. (Cited on page 8)

[25] P. M. Hohler and R. Rapp, "Is ρ-Meson Melting Compatible with Chiral Restoration?," *Phys. Lett. B* **731** (2014), pp. 103–109. (Cited on page 8, 9)

[26] A. K. Chaudhuri, *A Short Course on Relativistic Heavy Ion Collisions.* 2053-2563. IOP Publishing, 2014. (Cited on page 8)

[27] R. Snellings, "Collective Expansion at the LHC: selected ALICE anisotropic flow measurements," *J. Phys. G* **41** no. 12, (2014), p. 124007, `arXiv:1408.2532 [nucl-ex]`. (Cited on page 11)

[28] M. L. Miller, K. Reygers, S. J. Sanders, and P. Steinberg, "Glauber modeling in high energy nuclear collisions," *Ann. Rev. Nucl. Part. Sci.* **57** (2007), pp. 205–243, `arXiv:nucl-ex/0701025`. (Cited on page 12)

[29] **ALICE** Collaboration, M. Floris, "Charged particle production in Pb–Pb collisions at the LHC with the ALICE detector," *Nucl. Phys. A* **910-911** (2013), pp. 343–346. (Cited on page 12)

[30] **ALICE** Collaboration, B. Abelev *et al.*, "Centrality determination of Pb–Pb collisions at $\sqrt{s_{NN}} = 2.76$ TeV with ALICE,"*Phys. Rev. C* **88** (2013), p. 044909. (Cited on page 12)

[31] J. Schukraft and R. Stock, *Toward the Limits of Matter: Ultra-relativistic nuclear collisions at CERN*, vol. 23, pp. 61–87. 2015. (Cited on page 13)

[32] **NA57** Collaboration, F. Antinori *et al.*, "Energy dependence of hyperon production in nucleus nucleus collisions at SPS," *Phys. Lett. B* **595** (2004), pp. 68–74. (Cited on page 13)

[33] **STAR** Collaboration, B. Abelev *et al.*, "Enhanced strange baryon production in Au+Au collisions compared to p+p at $\sqrt{s_{NN}} = 200$ GeV," *Phys. Rev. C* **77** (2008), p. 044908, `arXiv:0705.2511 [nucl-ex]`. (Cited on page 13)

[34] **ALICE** Collaboration, B. B. Abelev *et al.*, "Multi-strange baryon production at mid-rapidity in Pb-Pb collisions at $\sqrt{s_{NN}} = 2.76$ TeV," *Phys. Lett. B* **728** (2014), pp. 216–227. [Erratum: Phys.Lett.B 734, 409–410 (2014)]. (Cited on page 13)

[35] **PHENIX** Collaboration, K. Adcox *et al.*, "Suppression of hadrons with large transverse momentum in central Au+Au collisions at $\sqrt{s_{NN}} = 130$ GeV," *Phys. Rev. Lett.* **88** (2002), p. 022301, arXiv:nucl-ex/0109003. (Cited on page 13)

[36] **CMS** Collaboration, S. Chatrchyan *et al.*, "Observation and studies of jet quenching in PbPb collisions at $\sqrt{s_{NN}} = 2.76$ TeV,"*Phys. Rev. C* **84** (2011), p. 024906. (Cited on page 13)

[37] **ATLAS** Collaboration, G. Aad, B. Abbott, *et al.*, "Observation of a Centrality-Dependent Dijet Asymmetry in Lead-Lead Collisions at $\sqrt{s_{NN}} = 2.76$ TeV with the ATLAS Detector at the LHC,"*Phys. Rev. Lett.* **105** (2010), p. 252303. (Cited on page 13)

[38] **ALICE** Collaboration, J. Adam *et al.*, "Measurement of jet quenching with semi-inclusive hadron-jet distributions in central Pb-Pb collisions at $\sqrt{s_{NN}} = 2.76$ TeV," *JHEP* **09** (2015), p. 170. (Cited on page 13)

[39] **ALICE** Collaboration, B. B. Abelev *et al.*, "Elliptic flow of identified hadrons in Pb-Pb collisions at $\sqrt{s_{NN}} = 2.76$ TeV," *JHEP* **06** (2015), p. 190. (Cited on page 14)

[40] **ALICE** Collaboration, J. Adam *et al.*, "Higher harmonic flow coefficients of identified hadrons in Pb-Pb collisions at $\sqrt{s_{NN}} = 2.76$ TeV," *JHEP* **09** (2016), p. 164. (Cited on page 14)

[41] **PHENIX** Collaboration, A. Bickley, "Quarkonium production in PHENIX," *Nucl. Phys. A* **783** (2007), pp. 285–292, arXiv:nucl-ex/0701035. (Cited on page 14)

[42] **NA50** Collaboration, B. Alessandro *et al.*, "A New measurement of J/ψ suppression in Pb-Pb collisions at 158-GeV per nucleon," *Eur. Phys. J. C* **39** (2005), pp. 335–345, arXiv:hep-ex/0412036. (Cited on page 14)

[43] **CMS** Collaboration, S. Chatrchyan and Anonymous, "Erratum: Observation of sequential Υ suppression in pbpb collisions [phys. rev. lett. 109, 222301 (2012)],"*Phys. Rev. Lett.* **120** (2018), p. 199903. (Cited on page 14)

[44] **ALICE** Collaboration, A. Maire, "Measurements of inclusive J/ψ production in Pb–Pb collisions at $\sqrt{s_{\mathrm{NN}}} = 2.76$ TeV with the ALICE experiment," *PoS* **ConfinementX** (2012), p. 211. (Cited on page 14)

[45] J. Hong and S. H. Lee, "$\Upsilon(1S)$ transverse momentum spectra through dissociation and regeneration in heavy-ion collisions," *Physics Letters B* **801** (2020), p. 135147. (Cited on page 14)

[46] **ALICE** Collaboration, B. Abelev *et al.*, "Transverse momentum distribution and nuclear modification factor of charged particles in p–Pb collisions at $\sqrt{s_{\mathrm{NN}}} = 5.02$ TeV" *Phys. Rev. Lett.* **110** no. 8, (2013), p. 082302. (Cited on page 16)

[47] J. L. Nagle and W. A. Zajc, "Small System Collectivity in Relativistic Hadronic and Nuclear Collisions," *Ann. Rev. Nucl. Part. Sci.* **68** (2018), pp. 211–235, arXiv:1801.03477 [nucl-ex]. (Cited on page 17)

[48] C. Loizides, "Experimental overview on small collision systems at the LHC," *Nucl. Phys. A* **956** (2016), pp. 200–207, arXiv:1602.09138 [nucl-ex]. (Cited on page 17)

[49] **CMS** Collaboration, V. Khachatryan *et al.*, "Observation of Long-Range Near-Side Angular Correlations in Proton-Proton Collisions at the LHC," *JHEP* **09** (2010), p. 091. (Cited on page 17)

[50] **ATLAS** Collaboration, G. Aad *et al.*, "Observation of Associated Near-Side and Away-Side Long-Range Correlations in $\sqrt{s_{\mathrm{NN}}}$=5.02 TeV Proton-Lead Collisions with the ATLAS Detector," *Phys. Rev. Lett.* **110** no. 18, (2013), p. 182302. (Cited on page 17)

[51] **CMS** Collaboration, S. Chatrchyan *et al.*, "Observation of Long-Range Near-Side Angular Correlations in Proton-Lead Collisions at the LHC," *Phys. Lett. B* **718** (2013), pp. 795–814. (Cited on page 17)

[52] **ALICE** Collaboration, B. Abelev *et al.*, "Long-range angular correlations on the near and away side in p–Pb collisions at $\sqrt{s_{\mathrm{NN}}} = 5.02$ TeV" *Phys. Lett. B* **719** (2013), pp. 29–41. (Cited on page 17)

[53] C. Loizides, "First results from p-Pb collisions at the LHC," *EPJ Web Conf.* **60** (2013), p. 06004. (Cited on page 17)

[54] **ALICE** Collaboration, J. Adam *et al.*, "Enhanced production of multi-strange hadrons in high-multiplicity proton-proton collisions," *Nature Phys.* **13** (2017), pp. 535–539. (Cited on page 17)

[55] **ALICE** Collaboration, J. Adam *et al.*, "Multi-strange baryon production in p-Pb collisions at $\sqrt{s_{NN}} = 5.02$ TeV," *Phys. Lett. B* **758** (2016), pp. 389–401. (Cited on page 17)

[56] Jan-e Alam and Sibaji Raha and Bikash Sinha, "Electromagnetic probes of quark gluon plasma," *Physics Reports* **273** no. 5, (1996), pp. 243–362. (Cited on page 18)

[57] T. Dahms, *Dilepton spectra in p+p and Au+Au collisions at RHIC*. PhD thesis, SUNY, Stony Brook, 2008. `arXiv:0810.3040 [nucl-ex]`. (Cited on page 18, 20)

[58] J.J. Sakurai and D. Schildknecht, "Generalized vector dominance and inelastic electron-proton scattering," *Physics Letters B* **40** no. 1, (1972), pp. 121 – 126. (Cited on page 19)

[59] A. Caliva, *Low-mass dielectron measurement in Pb–Pb collisions at $\sqrt{s_{NN}} = 2.76$ TeV with ALICE at the LHC*. PhD thesis, Utrecht U., 2017. (Cited on page 19)

[60] R. Rapp, G. Chanfray, and J. Wambach, "Medium modifications of the ρ meson at CERN SPS energies," *Phys. Rev. Lett.* **76** (1996), pp. 368–371, `arXiv:hep-ph/9508353`. (Cited on page 19, 26)

[61] R. Rapp and J. Wambach, "Chiral symmetry restoration and dileptons in relativistic heavy ion collisions," *Adv. Nucl. Phys.* **25** (2000), p. 1, `arXiv:hep-ph/9909229`. (Cited on page 19)

[62] R. Rapp, J. Wambach, and H. van Hees, *The Chiral Restoration Transition of QCD and Low Mass Dileptons*, vol. 23, p. 134. 2010. `arXiv:0901.3289 [hep-ph]`. (Cited on page 19)

[63] R. Rapp, "Dilepton Spectroscopy of QCD Matter at Collider Energies," *Adv. High Energy Phys.* **2013** (2013), p. 148253. (Cited on page 19, 24, 80, 81, 91, 92, 94, 95)

[64] Y. L. Dokshitzer and D. Kharzeev, "Heavy quark colorimetry of QCD matter," *Phys. Lett. B* **519** (2001), pp. 199–206. (Cited on page 21)

[65] J. C. Collins, D. E. Soper, and G. F. Sterman, *Factorization of Hard Processes in QCD*, vol. 5, pp. 1–91. 1989. `arXiv:hep-ph/0409313`. (Cited on page 21)

[66] G. Altarelli and G. Parisi, "Asymptotic Freedom in Parton Language," *Nucl. Phys. B* **126** (1977), pp. 298–318. (Cited on page 21)

[67] K. J. Eskola, P. Paakkinen, H. Paukkunen, and C. A. Salgado, "EPPS16: Nuclear parton distributions with LHC data," *Eur. Phys. J. C* **77** no. 3, (2017), p. 163. (Cited on page 21)

[68] T. Sloan, *History of the European Muon Collaboration (EMC)*. CERN Yellow Reports: Monographs. CERN, Geneva, 2019. `https://cds.cern.ch/record/2690197`. (Cited on page 22)

[69] K. Eskola, H. Paukkunen, and C. Salgado, "EPS09: A New Generation of NLO and LO Nuclear Parton Distribution Functions," *JHEP* **04** (2009), p. 065. (Cited on page 22, 82, 91, 92, 94, 95)

[70] S. Drell and T.-M. Yan, "Massive Lepton Pair Production in Hadron-Hadron Collisions at High-Energies," *Phys. Rev. Lett.* **25** (1970), pp. 316–320. [Erratum: Phys.Rev.Lett. 25, 902 (1970)]. (Cited on page 23)

[71] Esm, "Wikipedia, The Free Encyclopedia," 2006. `https://upload.wikimedia.org/wikipedia/commons/9/9f/Drell-Yan.svg`. [Online; accessed 10-August-2020]. (Cited on page 24)

[72] H. van Hees and R. Rapp, "Thermal Dileptons at LHC," *J. Phys. G* **35** no. 5, (2008), p. 054001.153, `arXiv:0706.4443 [hep-ph]`. (Cited on page 24, 25)

[73] **CERES** Collaboration, G. Agakichiev *et al.*, "Enhanced production of low mass electron pairs in 200-GeV/u S–Au collisions at the CERN SPS," *Phys. Rev. Lett.* **75** (1995), pp. 1272–1275. (Cited on page 25, 26)

[74] G.-Q. Li, C. Ko, and G. Brown, "Enhancement of low mass dileptons in heavy ion collisions," *Phys. Rev. Lett.* **75** (1995), pp. 4007–4010, `arXiv:nucl-th/9504025`. (Cited on page 26)

[75] D. Adamová, G. Agakichiev, *et al.*, "Modification of the ρ meson detected by low-mass electron–positron pairs in central PbAu collisions at 158A GeV/c," *Physics Letters B* **666** no. 5, (2008), pp. 425 – 429. (Cited on page 26, 27)

[76] **NA60** Collaboration, R. Arnaldi *et al.*, "First Measurement of the ρ Spectral Function in High-Energy Nuclear Collisions," *Phys. Rev. Lett.* **96** (2006), p. 162302, `arXiv:nucl-ex/0605007`. (Cited on page 26, 27)

[77] **NA60** Collaboration, R. Arnaldi *et al.*, "Evidence for radial flow of thermal dileptons in high-energy nuclear collisions," *Phys. Rev. Lett.* **100** (2008), p. 022302, `arXiv:0711.1816 [nucl-ex]`. (Cited on page 27)

[78] **PHENIX** Collaboration, A. Adare *et al.*, "Detailed measurement of the e^+e^- pair continuum in $p + p$ and Au+Au collisions at $\sqrt{s_{\mathrm{NN}}} = 200$ GeV and implications for direct photon production," *Phys. Rev. C* **81** (2010), p. 034911, `arXiv:0912.0244 [nucl-ex]`. (Cited on page 27)

[79] **STAR** Collaboration, L. Adamczyk *et al.*, "Di-electron spectrum at mid-rapidity in $p + p$ collisions at $\sqrt{s} = 200$ GeV," *Phys. Rev. C* **86** (2012), p. 024906, `arXiv:1204.1890 [nucl-ex]`. (Cited on page 27)

[80] **PHENIX** Collaboration, A. Adare *et al.*, "Cross section for $b\bar{b}$ production via dielectrons in d+Au collisions at $\sqrt{s_{\mathrm{NN}}} = 200$ GeV," *Phys. Rev. C* **91** no. 1, (2015), p. 014907, `arXiv:1405.4004 [nucl-ex]`. (Cited on page 27, 28)

[81] **PHENIX** Collaboration, A. Adare *et al.*, "Dielectron production in Au+Au collisions at $\sqrt{s_{\mathrm{NN}}} = 200$ GeV," *Phys. Rev. C* **93** no. 1, (2016), p. 014904, `arXiv:1509.04667 [nucl-ex]`. (Cited on page 27, 29)

[82] **STAR** Collaboration, L. Adamczyk *et al.*, "Dielectron Mass Spectra from Au+Au Collisions at $\sqrt{s_{\mathrm{NN}}} = 200$ GeV," *Phys. Rev. Lett.* **113** no. 2, (2014), p. 022301, `arXiv:1312.7397 [hep-ex]`. [Addendum: Phys.Rev.Lett. 113, 049903 (2014)]. (Cited on page 27, 29)

[83] **ALICE** Collaboration, S. Acharya *et al.*, "Dielectron production in proton-proton and proton-lead collisions at $\sqrt{s_{\mathrm{NN}}} = 5.02$ TeV," `arXiv:2005.11995 [nucl-ex]`. (Cited on page 28, 30, 32, 33, 35, 36, 75, 76, 86, 87, 88, 89, 91, 92, 94, 95)

[84] **ALICE** Collaboration, S. Acharya *et al.*, "Dielectron production in proton-proton collisions at $\sqrt{s} = 7$ TeV," *JHEP* **09** (2018), p. 064. (Cited on page 28, 29, 67, 78, 97)

[85] **ALICE** Collaboration, S. Acharya *et al.*, "Dielectron and heavy-quark production in inelastic and high-multiplicity proton–proton collisions at $\sqrt{s_{\mathrm{NN}}}$ = 13 TeV," *Phys. Lett. B* **788** (2019), pp. 505–518. (Cited on page 28, 29, 78)

[86] **ALICE** Collaboration, S. Acharya *et al.*, "Measurement of dielectron production in central Pb–Pb collisions at $\sqrt{s_{\mathrm{NN}}}$ = 2.76 TeV" *Phys. Rev. C* **99** no. 2, (2019), p. 024002. (Cited on page 28, 30)

[87] **ALICE** Collaboration, J. Adam, Adamová, *et al.*, "*D*-meson production in p–Pb collisions at $\sqrt{s_{\mathrm{NN}}}$ = 5.02 TeV and in pp collisions at $\sqrt{s}$ = 7 TeV,"*Phys. Rev. C* **94** (2016), p. 054908. (Cited on page 28)

[88] **ALICE** Collaboration, S. Acharya *et al.*, "Measurement of prompt D^0, D^+, D^{*+}, and D_S^+ production in p–Pb collisions at $\sqrt{s_{\mathrm{NN}}}$ = 5.02 TeV," *JHEP* **12** (2019), p. 092. (Cited on page 28)

[89] **ALICE** Collaboration, J. Adam *et al.*, "Measurement of electrons from heavy-flavour hadron decays in p–Pb collisions at $\sqrt{s_{\mathrm{NN}}}$ = 5.02 TeV," *Phys. Lett. B* **754** (2016), pp. 81–93. (Cited on page 30, 31)

[90] **ALICE** Collaboration, S. Acharya *et al.*, "Measurement of electrons from semileptonic heavy-flavour hadron decays at midrapidity in pp and Pb–Pb collisions at $\sqrt{s_{\mathrm{NN}}}$ = 5.02 TeV" *Phys. Lett. B* **804** (2020), p. 135377. (Cited on page 30)

[91] **ALICE** Collaboration, J. Adam *et al.*, "Measurement of azimuthal correlations of D mesons and charged particles in pp collisions at $\sqrt{s}$ = 7 TeV and p–Pb collisions at $\sqrt{s_{\mathrm{NN}}}$ = 5.02 TeV," *Eur. Phys. J. C* **77** no. 4, (2017), p. 245. (Cited on page 30)

[92] **ALICE** Collaboration, S. Acharya *et al.*, "Prompt and non-prompt J/ψ production and nuclear modification at mid-rapidity in p–Pb collisions at $\sqrt{s_{\mathrm{NN}}}$ = 5.02 TeV," *Eur. Phys. J. C* **78** no. 6, (2018), p. 466. (Cited on page 30, 31)

[93] **LHCb** Collaboration, R. Aaij *et al.*, "Study of prompt D^0 meson production in p–Pb collisions at $\sqrt{s_{\mathrm{NN}}}$ = 5 TeV," *JHEP* **10** (2017), p. 090. (Cited on page 30)

[94] **LHCb** Collaboration, R. Aaij *et al.*, "Prompt and nonprompt J/ψ production and nuclear modification in pPb collisions at $\sqrt{s_{\mathrm{NN}}} = 8.16$ TeV" *Phys. Lett. B* **774** (2017), pp. 159–178. (Cited on page 30)

[95] **ALICE** Collaboration, S. Acharya *et al.*, "Production of muons from heavy-flavour hadron decays in p–Pb collisions at $\sqrt{s_{\mathrm{NN}}} = 5.02$ TeV" *Phys. Lett. B* **770** (2017), pp. 459–472. (Cited on page 30)

[96] M. Cacciari, M. Greco, and P. Nason, "The p_{T} spectrum in heavy flavor hadroproduction," *JHEP* **05** (1998), p. 007. (Cited on page 31)

[97] M. Cacciari, S. Frixione, N. Houdeau, M. L. Mangano, P. Nason, and G. Ridolfi, "Theoretical predictions for charm and bottom production at the LHC," *JHEP* **10** (2012), p. 137. (Cited on page 31)

[98] **ALICE** Collaboration, B. B. Abelev *et al.*, "Performance of the ALICE Experiment at the CERN LHC," *Int. J. Mod. Phys.* **A29** (2014), p. 1430044. (Cited on page 38)

[99] P. Billoir, "Track fitting with multiple scattering: A new method," *Nuclear Instruments and Methods in Physics Research* **225** no. 2, (1984), pp. 352 – 366. (Cited on page 38)

[100] R. Frühwirth, "Application of Kalman filtering to track and vertex fitting," *Nucl. Instrum. Meth. A* **262** (1987), pp. 444–450. (Cited on page 38)

[101] **ALICE** Collaboration, M. Bondila *et al.*, "ALICE T0 detector," *IEEE Trans. Nucl. Sci.* **52** (2005), pp. 1705–1711. (Cited on page 38)

[102] **ALICE** Collaboration, J. Adam *et al.*, "Determination of the event collision time with the ALICE detector at the LHC," *Eur. Phys. J. Plus* **132** no. 2, (2017), p. 99. (Cited on page 38)

[103] **ALICE** Collaboration, P. Cortese *et al.*, *ALICE forward detectors: FMD, TO and VO: Technical Design Report.* Technical Design Report ALICE. CERN, Geneva, 2004. https://cds.cern.ch/record/781854. Submitted on 10 Sep 2004. (Cited on page 38)

[104] **ALICE** Collaboration, *ALICE Inner Tracking System (ITS): Technical Design Report.* Technical Design Report ALICE. CERN, Geneva, 1999. https://cds.cern.ch/record/391175. (Cited on page 39)

[105] **ALICE** Collaboration, K. Aamodt *et al.*, "Alignment of the ALICE Inner Tracking System with cosmic-ray tracks," *JINST* **5** (2010), p. P03003. (Cited on page 39)

[106] **ALICE** Collaboration, G. Dellacasa *et al.*, *ALICE time projection chamber: Technical Design Report*. Technical Design Report ALICE. CERN, Geneva, 2000. https://cds.cern.ch/record/451098. (Cited on page 40)

[107] **ALICE** Collaboration, J. Alme *et al.*, "The ALICE TPC, a large 3-dimensional tracking device with fast readout for ultra-high multiplicity events," *Nucl. Instrum. Methods Phys. Res. A* **622** no. 1, (2010), p. 316–367. (Cited on page 41)

[108] H. Bichsel, *The Interaction of Radiation with Matter*. 2011. (Cited on page 42)

[109] **ALICE** Collaboration, *ALICE Time-Of-Flight system (TOF): Technical Design Report*. Technical Design Report ALICE. CERN, Geneva, 2000. https://cds.cern.ch/record/430132. (Cited on page 41)

[110] **ALICE** Collaboration, N. Jacazio, "PID performance of the ALICE-TOF detector at Run 2," *PoS* **LHCP2018** (2018), p. 232. (Cited on page 42)

[111] **ALICE** Collaboration, B. Abelev *et al.*, "Measurement of visible cross sections in proton-lead collisions at $\sqrt{s_{\mathrm{NN}}} = 5.02$ TeV in van der Meer scans with the ALICE detector," *JINST* **9** (2014), p. P11003. (Cited on page 44)

[112] S. Lehner, *Dielectron production and a search for highly-charged particles in Pb–Pb collisions*. PhD thesis, 2019. https://cds.cern.ch/record/2705740. Presented 16 Dec 2019. (Cited on page 48)

[113] **ALICE** Collaboration, C. W. Fabjan *et al.*, "ALICE: Physics performance report, volume II," *J. Phys. G* **32** (2006), pp. 1295–2040. (Cited on page 50)

[114] R. Brun, R. Hagelberg, M. Hansroul, and J. C. Lassalle, *Simulation program for particle physics experiments, GEANT: user guide and reference manual*. CERN, Geneva, 1978. https://cds.cern.ch/record/118715. (Cited on page 58)

[115] R. Brun, F. Bruyant, F. Carminati, S. Giani, M. Maire, A. McPherson, G. Patrick, and L. Urban, *GEANT: Detector Description and Simulation Tool*. CERN Program Library. CERN, Geneva, 1993. Long Writeup W5013. (Cited on page 58)

[116] S. Roesler, R. Engel, and J. Ranft, "The Monte Carlo event generator DPMJET-III," in *Advanced Monte Carlo for radiation physics, particle transport simulation and applications. Proceedings, Conference, MC2000, Lisbon, Portugal, 2000*, pp. 1033–1038. 2000. arXiv:hep-ph/0012252 [hep-ph]. (Cited on page 58)

[117] T. Sjostrand, S. Mrenna, and P. Z. Skands, "PYTHIA 6.4 Physics and Manual," *JHEP* **05** (2006), p. 026. (Cited on page 59, 73)

[118] T. Pierog, I. Karpenko, J. M. Katzy, E. Yatsenko, and K. Werner, "EPOS LHC: Test of collective hadronization with data measured at the CERN Large Hadron Collider," *Phys. Rev.* **C92** (2015), p. 034906, arXiv:1306.0121 [hep-ph]. (Cited on page 59)

[119] **PHENIX** Collaboration, A. Adare *et al.*, "Detailed measurement of the e^+e^- pair continuum in $p + p$ and Au+Au collisions at $\sqrt{s_{\mathrm{NN}}} = 200$ GeV and implications for direct photon production," *Phys. Rev.* **C81** (2010), p. 034911, arXiv:0912.0244 [nucl-ex]. (Cited on page 69)

[120] N. M. Kroll and W. Wada, "Internal Pair Production Associated with the Emission of High-Energy Gamma Rays," *Phys. Rev.* **98** (1955), pp. 1355–1359. (Cited on page 69)

[121] **NA60** Collaboration, R. Arnaldi *et al.*, "Study of the electromagnetic transition form-factors in $\eta \to \mu^+\mu^-\gamma$ and $\omega \to \mu^+\mu^-\pi^0$ decays with NA60," *Phys. Lett. B* **677** (2009), pp. 260–266. (Cited on page 70)

[122] **NA60** Collaboration, R. Arnaldi *et al.*, "Precision study of the $\eta \to \mu^+\mu^-\gamma$ and $\omega \to \mu^+\mu^-\pi^0$ electromagnetic transition form-factors and of the $\rho \to \mu^+\mu^-$ line shape in NA60," *Phys. Lett. B* **757** (2016), pp. 437–444. (Cited on page 70)

[123] G. J. Gounaris and J. J. Sakurai, "Finite-Width Corrections to the Vector-Meson-Dominance Prediction for $\rho \to e^+e^-$," *Phys. Rev. Lett.* **21** (1968), pp. 244–247. (Cited on page 70)

[124] **ALICE** Collaboration, S. Acharya *et al.*, "Neutral pion and η meson production in p-Pb collisions at $\sqrt{s_{\mathrm{NN}}} = 5.02$ TeV" *Eur. Phys. J. C* **78** no. 8, (2018), p. 624. (Cited on page 70, 72, 73)

[125] **ALICE** Collaboration, B. Abelev *et al.*, "Multiplicity Dependence of π, K, p and Λ Production in p–Pb Collisions at $\sqrt{s_{\mathrm{NN}}} = 5.02$ TeV" *Phys. Lett.* **B728** (2014), pp. 25–38. (Cited on page 70, 72, 74)

[126] R. Hagedorn, "Multiplicities, p_T Distributions and the Expected Hadron $\rightarrow$ Quark - Gluon Phase Transition," *Riv. Nuovo Cim.* **6N10** (1983), pp. 1–50. (Cited on page 70)

[127] F. Binon *et al.*, "The isospin-violating decay $\eta' \rightarrow 3\pi^0$," *Physics Letters B* **140** no. 3, (1984), pp. 264 – 268. (Cited on page 71)

[128] K. Reygers, A. Schmah, A. Berdnikova, and X. Sun, "Blast-wave description of Υ elliptic flow at energies available at the CERN Large Hadron Collider," *Phys. Rev. C* **101** (2020), p. 064905. (Cited on page 71)

[129] R. Baur *et al.*, "First results of the CERES electron pair spectrometer from p+Be, p+Au and S+Au collisions," *Nuclear Physics A* **566** (1994), pp. 87 – 94. (Cited on page 72, 73)

[130] **ALICE** Collaboration, B. Abelev *et al.*, "Neutral pion and η meson production in proton-proton collisions at $\sqrt{s} = 0.9$ TeV and $\sqrt{s} = 7$ TeV," *Phys. Lett. B* **717** (2012), pp. 162–172. (Cited on page 72, 73)

[131] **ALICE** Collaboration, S. Acharya *et al.*, "π^0 and η meson production in proton-proton collisions at $\sqrt{s} = 8$ TeV," *Eur. Phys. J. C* **78** no. 3, (2018), p. 263. (Cited on page 72, 73)

[132] **ALICE** Collaboration, S. Acharya *et al.*, "Soft-dielectron excess in proton-proton collisions at $\sqrt{s} = 13$ TeV," arXiv:2005.14522 [nucl-ex]. (Cited on page 72, 73)

[133] T. Sjostrand, S. Mrenna, and P. Z. Skands, "A Brief Introduction to PYTHIA 8.1" *Comput. Phys. Commun.* **178** (2008), pp. 852–867, arXiv:0710.3820 [hep-ph]. (Cited on page 72)

[134] **WA80** Collaboration, R. Albrecht *et al.*, "Production of η mesons in 200-A/GeV S+S and S+Au reactions," *Phys. Lett.* **B361** (1995), pp. 14–20, arXiv:hep-ex/9507009 [hep-ex]. (Cited on page 72)

[135] P. K. Khandai, P. Shukla, and V. Singh, "Meson spectra and m_T scaling in $p+p$, $d+$Au, and Au$+$Au collisions at $\sqrt{s_{NN}} = 200$ GeV," *Phys. Rev. C* **84** (2011), p. 054904, arXiv:1110.3929. (Cited on page 72)

[136] L. Altenkämper, F. Bock, C. Loizides, and N. Schmidt, "Applicability of transverse mass scaling in hadronic collisions at energies available at the CERN Large Hadron Collider," *Phys. Rev.* **C96** (2017), p. 064907. (Cited on page 72)

[137] **ALICE** Collaboration, J. Adam *et al.*, "Production of K$^*(892)^0$ and $\phi(1020)$ in p–Pb collisions at $\sqrt{s_{NN}} = 5.02$ TeV," *Eur. Phys. J.* **C76** (2016), p. 245. (Cited on page 73, 74)

[138] P. Z. Skands, "Tuning Monte Carlo Generators: The Perugia Tunes," *Phys. Rev.* **D82** (2010), p. 074018, arXiv:1005.3457 [hep-ph]. (Cited on page 73)

[139] **CTEQ** Collaboration, H. Lai, J. Huston, S. Kuhlmann, J. Morfin, F. I. Olness, J. Owens, J. Pumplin, and W. Tung, "Global QCD analysis of parton structure of the nucleon: CTEQ5 parton distributions," *Eur. Phys. J. C* **12** (2000), pp. 375–392, arXiv:hep-ph/9903282. (Cited on page 73)

[140] P. Nason, "A New method for combining NLO QCD with shower Monte Carlo algorithms," *JHEP* **11** (2004), p. 040. (Cited on page 75)

[141] S. Frixione, P. Nason, and G. Ridolfi, "A Positive-weight next-to-leading-order Monte Carlo for heavy flavour hadroproduction," *JHEP* **09** (2007), p. 126. (Cited on page 75)

[142] S. Frixione, P. Nason, and C. Oleari, "Matching NLO QCD computations with Parton Shower simulations: the POWHEG method," *JHEP* **11** (2007), p. 070. (Cited on page 75)

[143] P. M. Nadolsky, H.-L. Lai, Q.-H. Cao, J. Huston, J. Pumplin, D. Stump, W.-K. Tung, and C.-P. Yuan, "Implications of CTEQ global analysis for collider observables," *Phys. Rev. D* **78** (2008), p. 013004, arXiv:0802.0007 [hep-ph]. (Cited on page 75)

[144] **ALICE** Collaboration, D. Adamová *et al.*, "J/ψ production as a function of charged-particle pseudorapidity density in p–Pb collisions at $\sqrt{s_{NN}} = 5.02$ TeV," *Phys. Lett.* **B776** (2018), pp. 91–104. (Cited on page 77)

[145] P. Golonka and Z. Was, "PHOTOS Monte Carlo: A Precision tool for QED corrections in Z and W decays," *Eur. Phys. J.* **C45** (2006), pp. 97–107, `arXiv:hep-ph/0506026 [hep-ph]`. (Cited on page 77)

[146] **ALICE** Collaboration, "Production of $\omega(782)$ in pp collisions at $\sqrt{s} = 7$ TeV,", 2018. `https://cds.cern.ch/record/2316785`. (Cited on page 78)

[147] **ALICE** Collaboration, B. Abelev *et al.*, "Technical Design Report for the Upgrade of the ALICE Inner Tracking System," *J. Phys. G* **41** (2014), p. 087002. (Cited on page 98)

[148] **ALICE** Collaboration, C. Lippmann, "Upgrade of the ALICE Time Projection Chamber," Tech. Rep. CERN-LHCC-2013-020, ALICE-TDR-016, 3, 2014. `https://cds.cern.ch/record/1622286`. (Cited on page 98)

[149] Z. Citron *et al.*, *Report from Working Group 5: Future physics opportunities for high-density QCD at the LHC with heavy-ion and proton beams*, vol. 7, pp. 1159–1410. 12, 2019. (Cited on page 98)

[150] L. Musa, "Letter of Intent for an ALICE ITS Upgrade in LS3," Tech. Rep. CERN-LHCC-2019-018. LHCC-I-034, CERN, Geneva, Dec, 2019. `https://cds.cern.ch/record/2703140`. (Cited on page 98)

[151] D. Adamová *et al.*, "A next-generation LHC heavy-ion experiment," `arXiv:1902.01211 [physics.ins-det]`. (Cited on page 98)

[152] A. Hoecker, P. Speckmayer, J. Stelzer, J. Therhaag, E. von Toerne, and H. Voss, "TMVA: Toolkit for Multivariate Data Analysis," *PoS* **ACAT** (2007), p. 040, `arXiv:physics/0703039v5 [physics.data-an]`. (Cited on page 103)

[153] Rene Brun and Fons Rademakers, "ROOT - An Object Orientated Data Analysis Framework," `arXiv:1902.01211v2 [physics.ins-det]`. (Cited on page 103)

[154] Alpaydin, Ethem, *Introduction to Machine Learning (Adaptive Computation and Machine Learning)*. The MIT Press, 2004. (Cited on page 103)

Abbreviations

ALICE	A Large Ion Collider Experiment
BDT	Boosted Decision Tree
CERN	Conseil Européen pour la Recherche Nucléaire
CNM	Cold Nuclear Matter
DCA	Distance-of-Closest Approach
DIS	Deep Inelastic Scattering
DY	Drell-Yan
EM	ElectroMagnetic
EoS	Equation of State
FONLL	Fixed Order + Next-to-Leading Logarithms
HF	Heavy-Flavour
HG	Hadron Gas
HIC	Heavy-Ion Collision
IMR	Intermediate-Mass Region
ITS	Inner Tracking System
LF	Light-Flavour
LHC	Large Hadron Collider
LMR	Low-Mass Region

LO	Leading-Order
LQCD	Lattice Quantum ChromoDynamics
LS	Long-Term Shutdown
MAPS	Monolithic Active Pixel Sensor
MB	Minimum-Bias
MC	Monte Carlo
ML	Machine Learning
NLO	Next-to-Leading-Order
nPDF	nuclear Parton Distribution Function
PDF	Parton Distribution Function
PHSD	Parton-Hadron-String-Dynamics
PID	Particle IDentification
POWHEG	POsitive Weight Hardest Emission Generator
QA	Quality Assurance
QCD	Quantum ChromoDynamics
QED	Quantum ElectroDynamics
QGP	Quark–Gluon Plamsa
SDD	Silicon Drift Detector
SM	Standard Model
SPD	Silicon Pixel Detector
SSD	Silicon Strip Detector
TMVA	Toolkit for MultiVariate Analysis

TOF	Time-Of-Flight
TPC	Time Projection Chamber
TRD	Transition Radiation Detector

Aaron Capon, MSc

Address:	Flotowgasse 22/11/10, 1190, Vienna, Austria
Phone:	+43 677 619 869 61
Date of birth:	25/01/1988
Nationality:	Australian
Email:	aaroncapon@protonmail.com

EDUCATION

Doctoral Program in Technical Physics
Doctoral Programme Particles & Interactions, FWF　　　　Vienna, Austria
Technical University of Vienna　　　　05/2016–ongoing

- Thesis: Dielectron production in proton–lead collisions at $\sqrt{s_{\mathrm{NN}}} = 5.02$ with ALICE at the LHC, Supervisors: Prof. Dr. Eberhard Widmann and Dr. Michael Weber

Master of Science, Physics　　　　Vienna, Austria
University of Vienna　　　　01/2013–04/2016

- Thesis: Construction of a Scintillating Hodoscope Detector for Measurements on the Hyperfine Structure of Antihydrogen, Supervisor: Prof. Dr. Eberhard Widmann

Bachelor of Science, Physics　　　　Melbourne, Australia
University of Melbourne　　　　03/2009–07/2012

EXPERIENCE

Scientific Assistant　　　　Vienna, Austria
Stefan Meyer Institute for Subatomic Physics, Austrian Academy of Sciences　　　　05/2016 – 08/2020

- Data analysis of low-mass dielectron production recorded with the ALICE detector at CERN with a focus on applying machine learning techniques

Scientific Assistant　　　　Vienna, Austria
Stefan Meyer Institute for Subatomic Physics, Austrian Academy of Sciences　　　　06/2014 - 09/2015

- Construction, characterisation and installation of hodoscope detector for the detection of antihydrogen

TALKS AND PRESENTATIONS

- Poster at Quark Matter, Wuhan, China　　　　November 2019
  A multivariate approach to measuring low-mass dielectrons in p-Pb collisions at $\sqrt{s_{\mathrm{NN}}} = 5.02$ TeV with ALICE
- Talk at Strangeness in Quark Matter, Bari, Italy　　　　June 2019
  Low-mass dielectron measurements in pp, p-Pb and Pb-Pb collisions with ALICE at the LHC
- Poster at Quark Matter, Venice, Italy　　　　May 2018
  Low-mass dielectrons in p-Pb collisions at $\sqrt{s_{\mathrm{NN}}} = 5.02$ TeV with ALICE
- Poster at Quark Matter, Chicago, USA　　　　February 2017
  Machine learning methods in the analysis of low-mass dielectrons in ALICE

Publications

[1] S. Acharya *et al.*, "Dielectron production in proton-proton and proton-lead collisions at $\sqrt{s_{NN}} = 5.02$ TeV", 2020. arXiv: 2005.11995 `[nucl-ex]`.

[2] B. Kolbinger *et al.*, "Measurement of the principal quantum number distribution in a beam of antihydrogen atoms", 2020. arXiv: 2008.04246 `[physics.atom-ph]`.

[3] S. Acharya *et al.*, "Dielectron and heavy-quark production in inelastic and high-multiplicity protoncollisions at $\sqrt{s_{NN}} = 13$TeV", *Phys. Lett. B*, vol. 788, pp. 505–518, 2019. arXiv: 1805.04407 `[hep-ex]`.

[4] S. Acharya *et al.*, "Measurement of dielectron production in central Pb-Pb collisions at $\sqrt{s_{NN}} = 2.76$ TeV", *Phys. Rev. C*, vol. 99, no. 2, p. 024 002, 2019. arXiv: 1807.00923 `[nucl-ex]`.

[5] S. Acharya *et al.*, "Dielectron production in proton-proton collisions at $\sqrt{s} = 7$ TeV", *JHEP*, vol. 09, p. 064, 2018. arXiv: 1805.04391 `[hep-ex]`.

[6] C. Sauerzopf *et al.*, "Annihilation detector for an in-beam spectroscopy apparatus to measure the ground state hyperfine splitting of antihydrogen", *Nucl. Instrum. Meth. A*, vol. 845, pp. 579–582, 2017.

Professional Skills and Interests

- **Programming languages:** C++, Python, Bash
- **Proficient with:** Linux, iOS, Windows, Git, LaTeX
- **Interests:** Physics, Data analysis, machine learning

Languages

- **English:** Native
- **German:** B1

Extracurricular Interests

Rock climbing, reading, surfing, snowboarding, cycling